Dissertation
zur Erlangung der Doktorwürde
an der

Gesamtfakultät für Mathematik,
Ingenieur- und Naturwissenschaften
der
Ruprecht-Karls-Universität Heidelberg

Thema:

Field-alignment and measurement of the director in liquid crystals and new forms of 3D printing.

vorgelegt von:
Lovish Gulati

Max Planck Institute for Medical Research, Heidelberg, Germany
Ruprecht-Karls-Universität Heidelberg, Heidelberg, Germany

June 30, 2025

Gutachter:
Professor Dr. Peer Fischer
Professor Dr. Christine Selhuber-Unkel

Contents

Abstract

3D liquid crystalline (LC) structures are complex soft materials that can exhibit stimuli-responsive mechanical deformations based on their geometry and programmed director profile. Mechanical deformations occur when the programmed molecular orientations are disrupted, leading to collective chain-conformational changes in the polymer network. Various fabrication and alignment techniques are available to design their 3D shape. The director profile within LC polymers determines their actuation profile. More complex actuation demands complete control over the 3D structural design as well as 3D director alignment, independent of the structure's axis. Achieving this 3D capability with traditional techniques remains challenging. Generally, elevated temperatures and high external fields are needed or coupling of the director to the structural design, which restricts the 3D control. It is also challenging to determine and characterize the 3D director orientation. For printing complex 3D shapes, these methods rely on sequential layer-by-layer or scanning systems which creates interfaces where the director alignment is distorted.

This thesis aims to overcome these challenges by providing effective ways to:

1. Align the director in 3D within a structure,

2. Characterize and visually determine the 3D director orientation in real time, and

3. Enable single-shot, parallel fabrication of entire 3D complex structures with an independent 3D global director.

Moreover, all these techniques for alignment, characterization, and fabrication can be utilized at room temperature.

The first project focuses on spatially patterning complex 3D director orientations voxel by voxel using weak magnetic fields. We prepare an LC gel ink formulation containing the non-reactive mesogens E7 and 5CB, which facilitate magnetic alignment control at room temperature. The director can be oriented in any desired direction by rotating the external magnetic fields. A Wollaston prism with a spatially varying 3D optic axis is fabricated to demonstrate the arbitrary 3D director alignment control and fabrication of advanced 3D LC optical elements at room

temperature.

The second project introduces an optical method for characterizing 3D director orientation using a wedge cell technique, which enables the real-time visual determination of the 3D director orientation. It is based on the birefringence influenced by the out-of-plane director alignment. The in-plane and out-of-plane director orientations are measured and calculated based on polarization states and the angular separation of the beam splitting. This method provides a fast and reliable protocol for precisely determining the 3D director orientation.

The third project aims to fabricate entire 3D structures in a single exposure at room temperature while maintaining the 3D director alignment independent of the structure's geometry. To achieve this, optical holographic lithography is shown to generate 3D light intensity patterns for the direct polymerization of 3D shapes in a single exposure. The single shot holographic fabrication of 4D liquid crystals actuators is demonstrated.

Zusammenfassung

3D-flüssigkristalline (LC) Strukturen sind komplexe weiche Materialien, die aufgrund ihrer Geometrie und des programmierten Direktorprofils Stimulus-responsive mechanische Deformationen zeigen können. Mechanische Deformationen treten auf, wenn die molekularen Orientierungen gestört werden, was zu kollektiven Ketten- sowie Konformationsänderungen führt. Verschiedene Fertigungs- und Ausrichtungstechniken stehen zur Verfügung, um ihre 3D-Form zu beeinflussen. Das Direktorprofil innerhalb von LC-Polymeren bestimmt ihr Aktuierungsprofil. Komplexere Aktuierungen erfordern vollständige Kontrolle über das 3D-strukturelle Design sowie die 3D-Ausrichtung des Direktors, unabhängig von der Achse der Struktur. Die Realisierung dieser 3D-Fähigkeit mit traditionellen Techniken bleibt eine Herausforderung. Im Allgemeinen sind hohe Temperaturen und starke externe Felder erforderlich oder eine Kopplung des Direktors an das strukturelle Design, was die 3D-Kontrolle einschränkt. Es ist auch eine Herausforderung, die 3D-Ausrichtung des Direktors zu bestimmen und zu charakterisieren. Zum Drucken komplexer 3D-Formen werden sequenzielle Schicht- für Schicht- oder Scansysteme genutzt, die aber Grenzflächen erzeugen, an denen die Ausrichtung des Direktors verzerrt wird.

Diese Dissertation zielt darauf ab, diese Herausforderungen zu überwinden, indem sie effektive Methoden bietet, um:

1. den Direktor in 3D innerhalb einer Struktur auszurichten,

2. die 3D-Ausrichtung des Direktors in Echtzeit zu charakterisieren und visuell zu bestimmen und

3. Einzelaufnahme und parallele Fertigung ganzer 3D-komplexer Strukturen mit einem unabhängigen 3D-globalen Direktor ermöglichen.

Darüber hinaus können alle diese Techniken zur Ausrichtung, Charakterisierung und Fertigung bei Raumtemperatur genutzt werden.

Das erste Projekt konzentriert sich auf das räumliche Orientieren komplexer Direktorrichtungen Voxel für Voxel unter Verwendung schwacher Magnetfelder. Es wird eine LC-Gel Tinte untersucht,

die nicht-reaktiven Mesogene E7 und 5CB enthält, die die magnetische Ausrichtungssteuerung bei Raumtemperatur erleichtern. Der Direktor kann in jede gewünschte Richtung ausgerichtet werden, indem die externen Magnetfelder gedreht werden. Ein Wollastonprisma mit räumlich variierender 3D-optischer Achse wird hergestellt, um die beliebige 3D-Direktorausrichtung und die Fertigung fortschrittlicher 3D-LC-optischer Elemente bei Raumtemperatur zu demonstrieren.

Das zweite Projekt führt eine optische Methode zur Charakterisierung der 3D-Direktorausrichtung mit einer prismatischen Zelle (wedge cell) ein, die die Echtzeitbestimmung der 3D-Direktorausrichtung visuell ermöglicht. Sie basiert auf der Doppelbrechung, die durch die Ausrichtung des Direktors aus der Ebene beeinflusst wird. Die In-Plane- und Out-of-Plane-Direktororientierungen werden basierend auf Polarisationszuständen und der Winkeltrennung der Strahlspaltung gemessen und berechnet. Diese Methode bietet ein schnelles und zuverlässiges Protokoll zur präzisen Bestimmung der 3D-Direktorausrichtung.

Das dritte Projekt zielt darauf ab, ganze 3D-Strukturen mittels einer einzigen Belichtung bei Raumtemperatur zu fertigen, wobei die 3D-Ausrichtung des Direktors unabhängig von der Geometrie der Struktur beibehalten wird. Um dies zu ermöglichen, wird die optische holografische Lithografie verwendet, die die direkte Photopolymerisation von 3D-Formen in einer einzigen Belichtung ermöglicht. Die Einzelaufnahme-Holografische Fertigung von 4D-Flüssigkristall-Aktoren wird demonstriert.

STORM-BOTS ITN project

The PhD research has been conducted as part of Marie Sklodowska Curie European Training Network- STORM-BOTS (Soft and Tangible Organic Responsive Materials progressing roBOTic functionS) *https://storm-bots.eu*.

The work has been conducted under the supervision of and collaboration with

- **Prof. Dr. Peer Fischer**, Supervisor
- **Prof. Dr. Frank Gießelmann**, Co-supervisor
- **Dr. Carlos Sánchez-Somolinos**, Collaborator and STORM-BOTS coordinator

Research contributions

The research is done in the MNMS Group of **Prof. Dr. Peer Fischer**. I would also like to thank our collaborators for their contributions.

- **Prof. Dr. Frank Gießelmann** (University of Stuttgart) and his group members for hosting my visit and secondment in his labs, providing microscopy facilities, chemical samples, and engaging in helpful discussions.
- **Dr. Kai Melde** (IMSEAM, Heidelberg) and his group members for project collaboration on Optical Holographic Lithography and engaging in helpful discussions.
- **Dr. Alexander Song** (IMSEAM, Heidelberg) for project collaboration on Optical Holographic Lithography, his assistance in developing the optics setup, and engaging in helpful discussions.
- **Dr. Carlos Sánchez-Somolinos** (CSIC, Zaragoza) and his group members for hosting my visit and secondment in his labs, providing fabrication facilities, chemical samples, and engaging in helpful discussions.
- **Prof. Dr. Eva Blasco** (IMSEAM, Heidelberg) and her group members for providing microscopy facilities, chemical samples, and engaging in helpful discussions.
- **Prof. Dr. Christine Selhuber-Unkel** (IMSEAM, Heidelberg) and her group members for providing lab facilities and engaging in helpful discussions.
- **Prof. Antonio DeSimone** (SSSA, Pisa) and his group members for providing simulation results and engaging in helpful discussions.

Publications and conference contributions

Parts of the thesis have been published or have been presented at conferences

- **L. Gulati**, *C. Sánchez-Somolinos, F. Giesselmann, and P. Fischer.* "Aligning and Observing the Liquid Crystal Director in 3D Using Small Magnetic Fields and a Wedge-Cell." *Advanced Functional Materials* **35**, no. 3 (2025): 2413513.

- **L Gulati**, *F. Giesselmann, and P. Fischer.* "3D Director Alignment of Liquid Crystalline Structures with Magnetic Fields". Oral presentation at ILCEC - International Liquid Crystal Elastomer Conference, Boulder, Colorado, USA, October 2023

Manuscript to be submitted:

- **L. Gulati**[†], *J. Lee*[†], *R. Norouzikudian, C. Sánchez-Somolinos, A. DeSimone, K. Melde, A. Song, and P. Fischer.* "Holographic printing of 3D liquid crystal actuators"

[†] These authors contributed equally to the work.

1 Introduction

Liquid crystalline materials have shown explosive progress in modern science and engineering due to their anisotropic optical properties and stimuli-responsiveness. LC actuators are also exciting smart materials that utilize the anisotropy (molecular orientational ordering) of liquid crystals combined with the elasticity of cross-linked polymers. They have the ability to deform significantly under various external stimuli that disrupt their molecular orientation and trigger collective chain-conformational changes in the entire network. Their elastic and reordering properties cause the material to relax back to its initial network configuration when stimuli are removed. This inherent property of LC actuators makes them highly promising for various soft robotic applications, such as artificial muscles,[1] reconfigurable surfaces,[2, 3] soft robots,[4, 5] biomedical adhesives,[6] and smart textiles.[7]

In general, there are many different types of soft actuators, such as dielectric elastomer actuators,[8] hydrogel-based actuators,[9] pneumatic actuators,[10] and magnetically and light-driven actuators,[11, 12] that have shown real-world applications due to their flexibility, adaptability, and safer interaction with the environment—areas where traditional hard robots fail. However, polymeric materials exhibiting liquid crystallinity demonstrate programmable, reversible, and precise shape changes without requiring complex external hardware. LC actuators possess flexibility, durability, and miniaturization potential, making them ideal for applications in soft robotics.

The actuation mechanism of LC actuators depends on their director profile (the average orientation direction of the molecules). To achieve a particular mechanical deformation, the director must be programmed accordingly during the fabrication of LC actuators. More complex responses can be achieved with 3D structural design and 3D programmed director profiles. This 3D control is necessary to unlock all three degrees of freedom for actuation.

However, achieving this 3D control is highly challenging, as traditional alignment and printing techniques either impose geometrical constraints, require very high external field strengths, couple director alignment with the shape of the structure, have slow alignment speeds, or require temperature control during alignment. Furthermore, even for structures with 3D director align-

ment, characterizing the 3D director is highly complex and challenging. Traditional polarization microscopy techniques only provide visualization for the 2D projection and indirectly calculate the 3D director's information; hence, they cannot provide real-time visualization of the 3D director.

Another significant challenge in the field of LC actuators is printing complex 3D structures. Traditional techniques rely on layer-by-layer or voxel-by-voxel printing, require temperature control while printing, or couple director alignment with the structure's shape. This makes fabrication either slow, imposes geometrical constraints on the shape, or creates interfaces with distorted director orientations, limiting the quality of the printed structures.

In this thesis, I demonstrate how to overcome challenges by providing a method to align the director in any arbitrary 3D orientation using low external fields, allowing spatial patterning in 3D, independent of the structure shape, all at room temperature. The study demonstrates how to characterize and visualize the 3D director orientation in real time to achieve a precise orientation in 3D. Furthermore, it illustrates how complex 3D LC structures can be fabricated in a single-shot process with full control over the global director alignment within the structure.

This thesis comprises five chapters. Chapter 2 introduces background material. It introduces the basic properties of liquid crystalline materials and polymers. A brief overview of general alignment techniques is provided, with a focus on magnetic field alignment of LCs and related optimization parameters. The chapter also summarizes various 3D printing techniques used to fabricate 4D LC actuators. The limitations of these techniques are discussed, motivating the adoption of the optical holographic lithography technique demonstrated in this thesis. Additionally, light propagation in anisotropic LCs is discussed in detail, deriving and analyzing how 3D director alignment affects the propagation of transmitted light.

In Chapter 3, I present a method to control the director in 3D using low magnetic fields. I describe how to program spatially varying 3D directors at room temperature and fabricate LC actuators. The chapter begins by explaining the ink formulations and the printing setup. Then, I discuss the parameters required to optimize director alignment at room temperature and program spatially varying 2D director profiles. Finally, I demonstrate the fabrication of an optical prism with spatially varying birefringence.

Chapter 4 introduces an optical characterization technique to observe the local 3D orientation of the director. The study provides a protocol to analyze the in-plane and out-of-plane orientations of the director based on polarization as well as the angular separation of the observed beam splitting (into ordinary and extraordinary ray components). I demonstrate the visual determination of 3D orientation and verify the 3D alignment of fabricated 2D LC films.

Chapter 5 presents a technique to print complex 3D LC structures in a single short light

exposure at room temperature. The method utilizes 3D light intensity patterns to print entire 3D structures directly within the printing cell. It allows the global director to be programmed in any 3D orientation, irrespective of the structure's geometry and orientation. The thermal actuation of the fabricated structures is also studied. In particular, I demonstrate the use of this technique to fabricate 4D actuators that would be difficult to realize with other printing methods.

Finally, Chapter 6 summarizes the work of this thesis and provides an outlook on future directions.

2 General and theoretical background

In this chapter, I describe the fundamental concepts that underlie the work presented in this thesis. It begins with an introduction to liquid crystals, alignment techniques, and the printing of 4D LC actuators. Finally, the focus shifts to discussing the relationship between 3D director alignment and birefringence to understand the propagation of light beams inside birefringent LC, motivating the use of wedge cells for the optical characterization of the 3D director alignment.

2.1 Liquid crystals

The following closely follows the discussions found in the references[13–17], especially chapter 2 and 3 in ref [13], chapter 3 and 8 in ref [14], chapter 2 in ref [15], chapter 1 in ref [16] and chapter 3 in ref [17].

Liquid crystals are materials that exhibit properties of both solids and liquids. They possess intrinsic long-range ordering, similar to crystalline solids, while also being able to flow and show short-range positional order like liquids. These properties arise due to the chemical structure and shape of the LC molecules. The mesogens have a stiff rigid core with multiple aromatic rings that provide shape and intermolecular interactions, along with flexible groups at the ends, which contribute to fluidity in the nematic phase. (page 9-11 in [15], section 1.1 in [16] and section 3.1.1 in [17])

In this thesis, I will focus only on nematic LCs, the most common type exhibited by rod-shaped mesogens, where the molecules have long-range orientational order but no translational order. The orientation of LC molecules is defined by the director, denoted by $\vec{n'}$. This orientation is temperature-dependent and can be disrupted at high temperatures. (section 3.2 in [14] and section 2.2 in [15]) One example of nematic LC is 4-Cyano-4'-pentylbiphenyl (5CB) and its molecular structure is shown in Figure 2.1.

In nematic phase, the molecules do not have perfect orientation. The individual orientations $\vec{n'}$ of the molecules are different from each other. They tend to be parallel to a common axis,

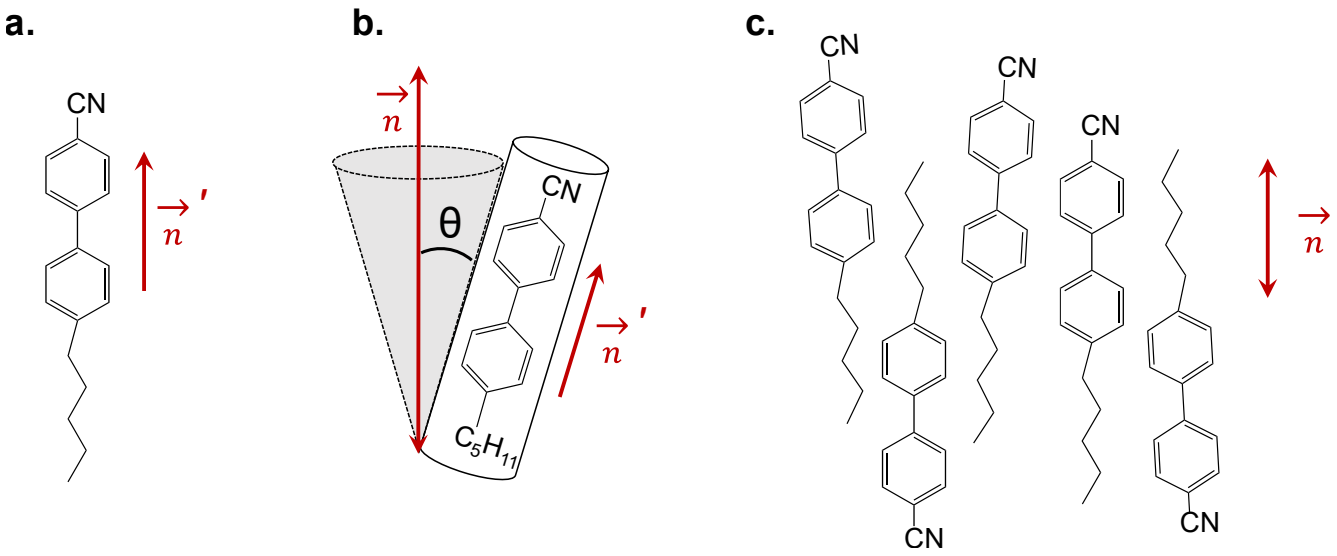

Figure 2.1: 5CB, a rod shape nematic liquid crystal. a) Molecular structure of 5CB having two aromatic rings with CN cyano group on one side and an alkyl chain (pentyl) on the other side. The molecular orientation is denoted by $\vec{n'}$. b) The polar angle θ is the angle of the molecular orientation $\vec{n'}$ with the average director alignment of the sample $\vec{n}$. c) The molecules are equally probable to have orientation $\vec{n'}$ and $-\vec{n'}$. Hence, the average LC director is denoted by the double headed arrow $\vec{n}$, implying that $\vec{n}$ and $-\vec{n}$ are equivalent. The figure and caption are adapted from Fig. 3 of [18] and Fig. 2.3 and 2.4 of [15].

labelled by director $\vec{n}$ as shown in Figure 2.1. In nematic phase, the molecular alignment $\vec{n'}$ is rotationally symmetric around $\vec{n}$ and molecules are equally probable to have $\vec{n'}$ and $-\vec{n'}$. Hence, the director states $\vec{n}$ and $-\vec{n}$ are not distinguishable. Therefore, the director $\vec{n}$ is represented by a double-headed arrow. (section 1.3.1 in [13], section 2.2 in [15])

A first-order phase transition can occur on heating, where the sample in the nematic phase undergoes transition to the isotropic phase within a narrow temperature range (a few Kelvin). The optical properties of the sample differ between phases, making it easy to observe the phase and alignment (due to birefringence in the nematic phase) using a polarization optical microscope (POM).

One important parameter to describe the quality of alignment is the order parameter. The average orientation of the molecules is given by the expression:

$$\langle \vec{n'} \rangle = \int \vec{n'} f(\theta)\, d\Omega = 0 \tag{2.1}$$

The distribution function $f(\theta, \phi)\, d\Omega$ represents the probability that a molecule is aligned in a direction within the solid angle $d\Omega = \sin(\theta)\, d\theta\, d\phi$, about the orientation direction specified by the Euler angles θ and ϕ in spherical coordinates. (section 3.3 in [17])

The zenithal angle θ is described with respect to the director $\vec{n}$, and it is assumed that all azimuthal angles ϕ are equally probable for each angle θ. section 3.3 in [17]

Since the molecules have an equal probability of $\vec{n'}$ or $-\vec{n'}$, the average value $\langle\vec{n'}\rangle = 0$. Hence, to solve this problem, a second-order tensor is defined that can be treated as the order parameter. The definition is: (section 1.1 in [16])

$$Q_{ab} = \frac{1}{2}\left(3\langle n'_a n'_b\rangle - \delta_{ab}\right) \tag{2.2}$$

with

$$\langle n'_a n'_b\rangle = \int n'_a n'_b f(\theta)\, d\Omega. \tag{2.3}$$

To simplify, the coordinate system is chosen where the director $\vec{n}$ coincides with the z-axis, $\vec{e}_z$ and the tensor $\mathbf{Q}$ can then be written as (Eq. 2.5 and 2.6 in [15])

$$\mathbf{Q} = S_2 \begin{pmatrix} -\frac{1}{2} & 0 & 0 \\ 0 & -\frac{1}{2} & 0 \\ 0 & 0 & 1 \end{pmatrix}, \tag{2.4}$$

here

$$S_2 = \frac{1}{2}\langle\left(3\cos^2\theta - 1\right)\rangle = \frac{3}{2}\frac{\int f(\theta)\cos^2(\theta)\, d\Omega}{\int f(\theta)\, d\Omega} - \frac{1}{2}, \tag{2.5}$$

The scalar order parameter is given by the coefficient S_2, strength of the order parameter and its value is defined as 1 when there is perfect order and 0 when there is no order (as in the isotropic state). Typically, for nematic liquid crystals, S_2 lies in the range between 0.4 and 0.7.

In a uniaxial phase where the tensorial properties are the same along x and y with $\chi_{11} = \chi_{22} \neq \chi_{33}$. The corresponding tensor can be expressed as: (section 3.5.2 in [17])

$$\chi_{\alpha\beta} = \begin{pmatrix} \chi_\perp & 0 & 0 \\ 0 & \chi_\perp & 0 \\ 0 & 0 & \chi_\parallel \end{pmatrix} \tag{2.6}$$

For instance, the magnetic susceptibility tensor in uniaxial systems has only two components. It can also be described in terms of the mean value $\langle\chi\rangle = \frac{1}{3}(\chi_\parallel + 2\chi_\perp)$ and the anisotropic value $\Delta\chi = \chi_a = \chi_\parallel - \chi_\perp$.

The traceless anisotropic tensor can be written as

$$\chi^a_{\alpha\beta} = \chi_{\alpha\beta} - \langle\chi\rangle\delta_{\alpha\beta} \tag{2.7}$$

$$\chi^a_{\alpha\beta} = \begin{pmatrix} \chi_\perp & 0 & 0 \\ 0 & \chi_\perp & 0 \\ 0 & 0 & \chi_\parallel \end{pmatrix} - \begin{pmatrix} \langle\chi\rangle & 0 & 0 \\ 0 & \langle\chi\rangle & 0 \\ 0 & 0 & \langle\chi\rangle \end{pmatrix} \tag{2.8}$$

$$= \begin{pmatrix} -\frac{1}{3}\chi_a & 0 & 0 \\ 0 & -\frac{1}{3}\chi_a & 0 \\ 0 & 0 & \frac{2}{3}\chi_a \end{pmatrix} \tag{2.9}$$

To obtain the dimensionless order parameter tensor, the anisotropy χ_a is normalized by dividing with the maximum anisotropy related to the orientation in a perfect crystal at absolute zero temperature. The expression becomes: (section 3.5.2 in [17])

$$Q_{\alpha\beta} = \frac{\chi^a_{\alpha\beta}}{\chi^{\max}_{\alpha\beta}} = \frac{\chi_a}{\chi^{\max}_a} \begin{pmatrix} -\frac{1}{3} & 0 & 0 \\ 0 & -\frac{1}{3} & 0 \\ 0 & 0 & \frac{2}{3} \end{pmatrix} = S_2 \left(n_\alpha n_\beta - \frac{1}{3}\delta_{\alpha\beta} \right). \tag{2.10}$$

This ratio of $\chi^a_{\alpha\beta}/\chi^{\max}_{\alpha\beta}$ is the scalar order parameter representing the degree of molecular statistical alignment order, as S_2 in equation 2.4 and its orientational component is represented by the tensor $Q_{\alpha\beta}$.

In general, the order parameter represents the director alignment and scalar order parameter, and it can also be expressed in terms of the director field rather than the mean orientations of the mesogens: (Eq. 1.2 in [16])

$$Q_{ij} = \frac{1}{2} S_2 \left(3 n_i n_j - \delta_{ij} \right) \tag{2.11}$$

Due to their relatively high order nematic liquid crystals also exhibit significant anisotropic properties. These anisotropic properties and the order parameter decrease with an increase in temperature, and at a certain temperature (called the critical temperature), the order vanishes, resulting in a phase transition from the nematic to the isotropic state. (Fig 1.3 in [16])

2.2 Crosslinked liquid crystalline polymers

The properties of liquid crystals give rise to certain "smart materials" such as crosslinked liquid crystal elastomers. This section provides a short introduction which summarizes the discussions found in [15, 19, 20], especially 3rd chapter of [15], 2nd section of ref [19], and 2nd section on page 3 of ref [20].

For soft robotic applications, crosslinked liquid crystalline polymers (CLCPs) are very promis-

ing. This class of materials is prepared by polymerizing mesogens that have functional groups. Depending on the position of these groups in the chemical structure of the mesogens, they can be covalently integrated to form a polymer network and can be classified into three categories. (page 3-15 in [19])

Main-chain LCEs, mesogens are part of the polymer backbone, and their flexible tails connect (acting as spacers) the adjacent mesogens, preventing crystallization. In *end-on side-chain* LCEs, the polymer backbone does not contain mesogens, but flexible chain extenders connect the ends of the mesogens to the polymer backbone. When these spacers connect orthogonally to the mesogens in the middle, the material is referred to as *side-on side-chain* LCEs. These polymeric chains are connected through mesogenic or non-mesogenic crosslinkers. (page 3-15 in [19] and 2nd section on page 3 in ref [20])

As the frequency of crosslinking increases, the stiffness of the material increases, and hence the flexibility of the LCEs decreases. If the polymer network also contains non-reactive mesogens, it is called liquid crystalline gels (LCGs), which are comparatively softer than other CLCPs. (page 7 in ref [20])

After crosslinking, the order in the polymer structures remains due to the intermolecular interactions, which enables their application in various mechanical actuations and optical elements. The domains in the sample, typically on the micrometer scale, have directors locally aligned due to these interactions. Techniques are used to induce uniform alignment across the entire sample, making it a monodomain where the sample has a single common director oriented in a desired direction. This alignment can amplify the material's response to stimuli and allows macroscopic bodies to exhibit mechanical properties in the volume possessing a uniform director alignment. [15, 20] The mechanical deformation results shown in Chapter 5 verify the programmed director alignment.

2.2.1 Vat polymerization

Vat polymerization is a process involving a light source and a "vat" containing the photopolymerizable ink, which is primarily composed of mono- or bifunctional chemical compounds and a photoinitiator (PI).[21] The reaction mechanism largely depends on the type of PI and the photocurable ink used to achieve the desired functional properties in the printed structures. In most cases, a radical system involving reactive mesogens with acrylate/methacrylate or vinyl-functional groups is employed.[22] Fast and high polymerization conversion is often observed in acrylate-functionalized chemical compounds, which are frequently preferred for 3D printing. In

our study, we use inks of this category for all the printed structures.

Figure 2.2: General process of free radical polymerization summarizing steps of initiation, propagation and termination. The schematic and caption are adapted from Fig.3 of [23].

The reaction mechanism is illustrated in Figure 2.2. The radical system utilizes a free radical polymerization mechanism to crosslink the ink composition of various monomers.[21, 22, 24–26]Upon light irradiation, the PI generates radicals R^*, which combine with the photopolymerizable groups of the monomers to form microradicals. This initiates the chain propagation step, where carbon-carbon bonds are formed with additional monomer units, leading to the growth of microradicals. This process continues until termination occurs in the final stage through radical recombination or disproportionation.

During recombination (also referred to as monomolecular termination), two chain-end species couple radicals by forming a carbon-carbon single bond. In disproportionation, one polymer radical chain transfers an atom (usually a hydrogen atom) to another chain-end radical, forming two polymeric chains—one with a quenched carbon-carbon single bond and the other with a double bond.

The kinetics of the mechanism involve three steps[23]: (1) After the photoinitiator (PI) is excited, the reactive units react with inhibitors, preventing effective polymerization. (2) In the second step, microradicals are formed once all the inhibitors are consumed. (3) Finally, the conversion slows down when the ink solidifies.

The radical photoinitiator (PI) converts photolytic energy into the generation of reactive species. These PIs can be classified into two categories: Norrish Type 1 and Norrish Type 2.[22, 27, 28] In the first category, the mechanism involves the splitting of a single photoreactive molecule into radical fragments upon light irradiation. Typical examples of Type 1 photoinitiators are acyl phosphine oxides, such as Irgacure 819 and TPO (diphenyl(2,4,6-trimethylbenzoyl)phosphine oxide). The presence of a phosphorus atom adjacent to the carbonyl group lowers the transition energy for the $n \rightarrow \pi^*$ process. As a result, the absorption maximum shifts toward longer wavelengths (around 400 nm),[29] enabling the photochemical generation of radicals without requiring

strong UV light irradiation. In the case of Norrish Type 2, a two-component system is utilized involving a sensitizer (as a light-absorbing molecule) and a synergist (as a co-initiator). After the suitable wavelength light is irradiated, the radical is generated through the transfer of a hydrogen atom from the synergist to the excited sensitizer. The free radical polymerization is then initiated by the synergist radical. Common examples of Type II sensitizers are Benzophenone and isopropylthioxanthone, while tertiary amines are commonly used as Type II co-initiators. [22, 27, 28]

We used TPO photoinitiator for all our fabrication results.

2.3 Alignment techniques

As discussed in the previous section, the order in the polymeric LC structures can be retained after polymerization. This section introduces how molecular alignment is controlled in the LC samples to either achieve uniform or spatially varying director orientation.

The director in LC materials is set through various alignment techniques before polymerization. To achieve a specific mechanical deformation, a particular director profile and shape geometry is required.[13, 30] However, fabricating 3D LC structures with arbitrary 3D director orientations for complex director profiles is challenging, as it is necessary to realize all three degrees of freedom for both shape geometry and anisotropic response. Researchers are exploring various methods to achieve this ideal fabrication approach. The conventional alignment techniques are discussed below.

Surface alignment is the most common method of alignment, where special surfaces are prepared by treating, patterning, or coating with specific polymers (which are also rubbed in the alignment direction for in-plane homogeneous alignment). These substrates are then used to create parallel plate LC cells, and the alignment from the surface anchoring is imparted into the bulk LC samples. Depending on the substrate treatment and the close positioning of two surfaces, one can generate planar, splay, twisted, or homeotropic alignment. Typical polymers used for rubbing alignments are polyimide (PI) and polyvinyl alcohol (PVA). Another type of surface-enforced alignment includes methods such as nano-/microgroove-based alignment[31, 32] and photo-alignment.[2, 33–36] These are all 2D or 2.5D methods.

Mechanical alignment utilizes highly viscous inks, where the director can be aligned along the mechanical stretching direction. This is a two-step alignment process: the inks are partially polymerized, then mechanically aligned, and finally fully crosslinked while under load. This technique is mostly used for obtaining unidirectionally aligned films and does not allow for arbitrary

orientations.[15]

Extrusion-based printing is another well-established technique used to print structures with an extrusion nozzle printer. The alignment can be controlled by the printing direction, as it is always coupled with the shear forces generated by the printhead motion.[37–40] The inks used are highly viscous and require precise control of parameters such as temperature, velocity, and nozzle geometry. To vary the director in 2D, one needs to draw the nozzle along specific trajectories, while for 3D structures, printing is achieved layer by layer.

The limitations of this technique include the inability to vary the alignment independently of the structure geometry. Additionally, only certain shapes of 3D structures can be printed, and the process is restricted to layer-by-layer fabrication

Field alignment is an exciting technique that has proven to address many challenges posed by other alignment methods. The director can be potentially varied arbitrarily in 3D orientation, independent of the structure geometry.[41–43] Since the molecules have polar functional groups, certain inks exhibit dielectric anisotropy and respond by realigning in the direction of an applied electric field. However, electric field alignment is challenging, as high field strengths are required, which can lead to dielectric breakdown of the inks. Magnetic alignment is an alternative that is discussed in detail in the next section. In general, field alignment requires low molar mass mesogens with low viscosity.

In our recent work, we have shown 3D arbitrary director alignment control using low magnetic field strengths[44], and the details of the experiment will be discussed in chapter 3.

2.3.1 Magnetic field alignment

Magnetic field alignment will be discussed in chapter 3. The discussion in this section introduces the topic and closely follows references [13, 45], especially section 3.2 in ref [13].

Aromatic mesogens exhibit positive diamagnetic susceptibility due to their zero-net spin and the dispersed electron distribution associated with delocalized charges.([45] and section 3.2.1 in [13]) The presence of benzene rings in the molecular structure causes these molecules to respond to a magnetic field according to Lenz's law. For instance, when an external magnetic field is applied perpendicular to the plane of these molecules, currents are induced in the benzene rings. These currents oppose the external field, reducing the magnetic flux passing through the rings. This interaction distorts the magnetic lines of force, leading to an increase in the system's energy. In contrast, when the magnetic field is parallel to the plane of the benzene rings, no flux passes through the rings, and consequently, no current is induced. As a result, the system's energy

remains unchanged. Therefore, it is energetically favorable for the molecules to orient themselves such that the applied field aligns with the plane of the rings.

Section 3.2.1 in [13] compares that this coupling energy of the single molecule is much smaller than the thermal energy. Hence, it is very difficult to orient a single isolated molecule in the vapor phase, even under the strongest practically achievable magnetic fields. On the other hand, if we consider a nematic sample containing about 10^{22} molecules, the collective response of the molecules leads to a higher coupling energy which can become much greater than $k_B T$. As will be shown, this makes it easier to align the nematic sample confined in liquid crystal (LC) cells of about 100–250 μm thickness. The magnetic alignment response is harder to realize in thinner samples due to surface anchoring effects.

To understand the effects of the field $\mathbf{H}$ on a nematic liquid crystal (LC) with director alignment $\mathbf{n}$, we can express the induced magnetization $\mathbf{M}$ as: (Eq. 3.44 in [13])

$$\mathbf{M} = \chi_{\parallel}\mathbf{H}, \quad \text{if } \mathbf{H} \text{ is parallel to } \mathbf{n},$$

$$\mathbf{M} = \chi_{\perp}\mathbf{H}, \quad \text{if } \mathbf{H} \text{ is perpendicular to } \mathbf{n}.$$

For an arbitrary angle, the general expression is given by: (Eq. 3.45 in [13])

$$\mathbf{M} = \chi_{\perp}\mathbf{H} + \chi_a(\mathbf{H}\cdot\mathbf{n})\mathbf{n},$$

where $\chi_a = \chi_{\parallel} - \chi_{\perp}$, is the anisotropy in the diamagnetic susceptibility.

The magnetic torque on the sample with magnetization $\mathbf{M}$ is given by: (Eq. 3.48 in [13])

$$\boldsymbol{\tau}_M = \mathbf{M}\times\mathbf{H} = \chi_a(\mathbf{n}\cdot\mathbf{H})\mathbf{n}\times\mathbf{H}. \tag{2.12}$$

In the nematic LC, this torque on the volume element is balanced by the torque due to surface anchoring, as discussed below.

2.3.2 Magnetic coherence Length

The discussion in this section is followed from references [13, 16, 45], especially page 660-666 of ref [45].

According to the Maier-Saupe theory, the director in the nematic phase tends to prefer uniform alignment throughout the sample volume, leading to the formation of a homogeneous director field. In the presence of external magnetic fields, the director alignment generally deforms continuously

from the surface alignment direction to the field alignment direction. This deformation typically occurs on a macroscopic scale (a few μm). However, this macroscopic deformation does not significantly alter the local degree of order. Instead, energy is required to induce elastic deformations in the director field of the nematic phase. In theory, three distinct types of director deformations are defined: splay, twist, and bend, as illustrated in Figure 2.3.

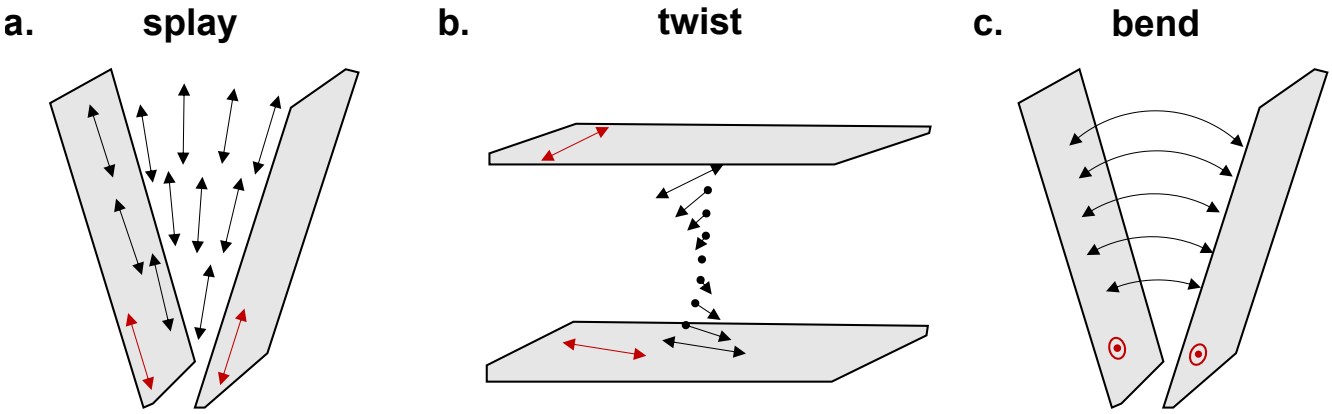

Figure 2.3: Graphical representation of three basic nematic LC-director distortions. a) splay, b) twist, c) bend. The LC director is shown in black and the surface orientation is shown in red arrow/marker. The figure and caption are adapted from [16].

For instance, consider the director in a nematic phase exhibiting a uniform twist. This can be achieved by preparing LC cells using rubbed surfaces such that the director is unidirectionally aligned parallel to the rubbing direction. If the orientation directions of the two substrates are rotated with respect to each other by an angle, a director field $\mathbf{n}(z) = (\cos\phi, \sin\phi, 0)$ with uniform twist $\frac{d\phi}{dz} = \frac{\phi}{d}$ about the z-axis is achieved.

According to the continuum theory, this deformation contributes to the free energy density, which is proportional to the square of the director twist: (Eq. 7.9 in [45])

$$F_D^{(V)} = K_2 \left(\frac{d\phi}{dz}\right)^2 \tag{2.13}$$

Here, K_2 is the elastic coefficient (with dimensions of energy per length) in the nematic phase, typically having values around 10^{-11} N. Using this value and considering $d = 10\,\mu$m and $\phi = 1$ rad (57°), the elastic twist deformation increases the free energy density by $0.1\,\mathrm{J/m^3}$. Due to the very small value of this energy increase, the twist deformation can be easily observed upon the application of an external field which is useful in display technologies. [45]

To generally summarize the energy density contributions due to the basic director deformations—bend, twist, and splay—according to the continuum theory: (Eq. 7.10 in [45])

$$F_D^{(V)} = \frac{1}{2}\left[K_1(\nabla \cdot \mathbf{n})^2 + K_2(\mathbf{n} \cdot \nabla \times \mathbf{n})^2 + K_3(\mathbf{n} \times \nabla \times \mathbf{n})^2\right] \tag{2.14}$$

Here, the three elastic constants can often be considered of the same magnitude ($K_1 = K_2 = K_3 = K$) using a one-constant approximation for simpler calculations.

The elastic constant depends on the anisotropic interactions, which both decrease with increasing temperature because they depend on the order parameter as $K \sim S^2$. To understand the distortion in the director field due to the external magnetic field $\mathbf{B}$, one can write its component of free energy density as: (Eq. 7.12 in [45])

$$F_{\text{B-field}}^{(V)} = -\frac{1}{2}\frac{\Delta\chi}{\mu_0}(\mathbf{n}\cdot\mathbf{B})^2 \tag{2.15}$$

This field energy changes with $\cos^2\phi$, where ϕ is the angle between the director and the field. Hence, the sample, having positive magnetic anisotropy ($\Delta\chi > 0$), experiences a torque to align the director parallel to the field direction.

This reorientation competes with the effects of surface anchoring, which often imposes an orientation different from the field direction. Therefore, the system prefers the minimum total energy state, accounting for both effects: (Eq. 7.13 in [45])

$$F_g = \int_V \left(F_{\text{Def}}^{(V)} + F_{\text{Field}}^{(V)}\right) dV \tag{2.16}$$

By integrating from $x = 0$ to $x = \infty$ and considering A as the area of the walls, the expression to be minimized can be written as: (Eq. 7.14 in [45])

$$F_g = \frac{A}{2}\int_0^\infty \left[K\left(\frac{d\phi}{dx}\right)^2 + \frac{\Delta\chi}{\mu_0}B^2\cos^2\phi\right] dx \tag{2.17}$$

Using the Euler-Lagrange equation, we can write: (Eq. 7.16 in [45])

$$K\frac{d^2\phi}{dx^2} - \frac{\Delta\chi}{\mu_0}B^2\sin\phi\cos\phi = 0 \tag{2.18}$$

Considering the characteristic length ξ as: [45]

$$\xi = \frac{1}{B}\sqrt{\frac{K\mu_0}{\Delta\chi}} \tag{2.19}$$

The expression can be rewritten as: (Eq. 7.17 in [45])

$$2\frac{d\phi}{dx}\frac{d^2\phi}{dx^2} - \frac{1}{\xi^2}\cdot 2\frac{d\phi}{dx}\sin\phi\cos\phi = 0 \tag{2.20}$$

Integrating this equation yields: (Eq. 7.18 in [45])

$$\left(\frac{d\phi}{dx}\right)^2 = \frac{\sin\phi}{\xi^2} + C \tag{2.21}$$

Using the boundary conditions $\phi = 0$ and $\frac{d\phi}{dx} = 0$ as $x \to \infty$, the constant C is determined to be 0. [45]

This leads to two energetically equivalent mirror images of director profiles: (Eq. 7.19 in [45])

$$\frac{d\phi}{dx} = \pm\frac{\sin\phi}{\xi}.$$

For the case of the negative sign and the boundary condition $\phi(x = 0) = \pi/2$, it can be integrated to obtain: (Eq. 7.20 in [45])

$$\phi(x) = 2\arctan\exp\left(-\frac{x}{\xi}\right), \quad \text{for } x \geq 0. \tag{2.22}$$

This is the expression for the deformed director field over the characteristic length thickness, referred to as the coherence length. For instance, if $B = 1\,\mathrm{T}$, $K = 10^{-11}\,\mathrm{N}$, and $\Delta\chi = 4\pi \times 10^{-7}$, the coherence length is calculated as $\xi = 3\,\mu\mathrm{m}$. [45]

The coherence length is an important factor in accounting for magnetic field alignment, as it represents the minimum dimension of the sample in which the director can reorient in response to external fields. Hence, to observe the realignment of the director with magnetic fields, the sample dimensions should be thicker than the coherence length.[13, 45] This will be a consideration in the experiments presented in chapter 3.

Similarly, to align a sample of a certain dimension d, a threshold magnetic field is required to achieve a characteristic length shorter than this thickness d. The exact calculation of the Freedericksz transition (the reorientation of the liquid crystal director in response to the external magnetic field exceeding a critical threshold field as this minimum field is required to overcome the competing elastic forces of the LC system) results in the relation $\pi\xi = d$, and the threshold field can be determined using: (Eq. 7.21 in [45])

$$B = \frac{\pi}{d}\sqrt{\frac{K\mu_0}{\Delta\chi}}. \tag{2.23}$$

This relation has been used to optimize the director alignment in response to low magnetic fields. The results are shown in Chapter 3.

2.4 3D printing of complex LC actuators

The next important step in the fabrication of crosslinked LC polymers includes printing. This section introduces the printing methods, properties, and challenges involved. It also motivates the goals of the fabrication methods presented in this thesis.

Researchers have utilized various techniques to fabricate 4D LC actuators at the micro and macroscale for applications in soft robotics and optical elements.[30, 37, 44, 46–51] It has been very challenging so far to print 3D geometries and independently control the director alignment with respect to the structure's axis. Programming complex 3D director profiles to achieve advanced actuation responses is difficult with the currently known methods. The most commonly used techniques are DIW (direct ink writing) and DLP (digital light projection) for macroscale objects, and 2PLP (two-photon laser printing) for microscale objects.

DIW involves the layer-by-layer printing of 3D geometries, where at each layer, the director is aligned by extruding viscous LCE ink.[37–40, 52] The shear forces then align the director along the printing direction, and one can design the pathways to program a 2D director profile for each layer. However, it is always challenging to select the right viscosity inks, set the appropriate printing velocity, and choose the correct printing pathways for complex 2D director profiles. Despite these challenges, this technique has been utilized to fabricate various 4D actuators, such as swimmers, grippers, folding structures, and adaptive optical elements, where light or temperature is used as an external stimulus for actuation.[37–40, 52]

The shape complexity of the printed structures in this research area has been addressed by printing freeform 3D LCE structures embedded in a gel matrix.[53] This method allows printing of free-standing complex 3D structures away from flat substrates without requiring any support structures. However, the director is still coupled to the printing direction, which limits the design of 3D LCE structures with varying actuation responses depending on the director profile.

The use of the DLP technique to print 4D LCE structures has been explored, where the director is aligned in 3D using magnetic fields or shear-flow induced alignment. One example of this work involves voxel-by-voxel printing, where the director in each voxel is oriented using magnetic fields.[41] It required high field strengths while keeping the ink at high temperatures (near nematic-isotropic transition temperatures of 100°).[41] Another example of using DLP is with shear flow alignment, where each shear-aligned layer has orientation order for the fabrication of soft actuators as self-sensing muscles.[54] The advancement of DLP has been demonstrated in printing 4D multi-responsive structures[55] and 4D LC emulsions.[56] However, all these methods are still layer-by-layer or voxel-by-voxel, which makes the printing very slow and places limitations

on the scalability of the fabrication. DLP printing has been demonstrated in fabricating structures at room temperature with magnetically programmed 3D director control, using non-reactive mesogens in the ink formulations.[57, 58]. These studies were published approximately around the same time and independently of our study (see Chapter 3).[44]

In microscale robotics, 2PLP (Two-Photon Lithography Printing) or DLW (Direct Laser Writing) has proven to be successful, utilizing the two-photon absorption process with a femtosecond pulsed laser to print complex 3D geometries.[42, 43, 59, 60] Two-photon absorption is a nonlinear process that depends on the square of the light intensities; polymerization only occurs in the high-intensity regions near the focus of the beam. Hence, this technique can achieve submicrometer resolution, which is very challenging in other one-photon absorption techniques.[28] However, this technique requires advanced and expensive equipment, as well as control over various experimental parameters such as laser intensity, printing speed, ink formulations, and focusing the laser light using an objective lens. Moreover, the voxel size depends on the printing speed and laser power, and one must surpass the threshold limit of laser power needed for photopolymerization. 2PLP has been utilized with in situ electric field alignment of the LC director, where the director is aligned using a quasi-static electric field with variable orientation control.[42, 43] The electric field orientation can be set arbitrarily in 3D using optically transparent electrodes. However, the voxel size is limited, as it requires high field strengths that can lead to dielectric breakdown. Examples are shown for the printing of the microwalker responsive to light stimulus[61], a photonic microhand[62], and multi-photoresponsive actuators[60]. Furthermore, for applications in tunable optical devices, whispering gallery mode (WGM) resonators are demonstrated, and the frequency of the resonators can be controlled optically.[63] Another example of using 2PLP is the fabrication of temperature- and light-responsive optical gratings.[64–66] A recent advancement in the use of 2PLP technique is demonstrated in the 3D spatial director alignment of LC mesogens using 3D-printed polydimethylsiloxane-based confinement barriers.[59] One drawback is that 2PLP is based on scanning and therefore is very slow, putting limitations on the number of 3D LC actuators that can be printed.

The following sections describe traditional 3D printing techniques used in general, not specific to LCs. These techniques will help motivate the method used in this thesis to parallel print 4D LC actuators.

2.4.1 Volumetric additive manufacturing

Another advanced 3D printing technique is Volumetric Additive Manufacturing (VAM), which can print object parts volumetrically to integrate different components, as opposed to the layer-by-layer method.[67, 68] While other 3D printing techniques rely on scanning, VAM utilizes light to selectively solidify a photosensitive resin within a constrained volume. The method is very similar to computed tomography (CT) principles (often used in medical imaging) and employs multiple 2D light patterns to construct a 3D volume by projecting 2D images from different angles. It cures the ink at the superposition of the beams, leading to the polymerization of a high-resolution, desired 3D geometry of up to 55 mm lateral size in about 30 to 300 seconds.[68] The advantage is that there is no need for support structures to create 3D objects. However, there are many challenges, including the relatively slow printing speed due to multiple exposures, the need for special inks, and precise calibration of the 2D images.

Advances have been made to achieve multi-material printing using a suspension bath in VAM of non-viscous inks. Here, a sacrificial matrix is used as a shear-yielding bath to support complex 3D shapes, preventing the structure from collapsing in air. [69] With this approach, it has been shown that one can fabricate multiple materials.[69]

2.4.2 Flow lithography

Flow lithography is a microfabrication technique that can print structures using UV photopolymerization in a continuously flowing ink within microfluidic channels. The technique has two categories: continuous flow lithography and stop flow lithography, depending on the flow speed during curing. [70] The method can be integrated with one-photon or two-photon polymerization and has been shown to print 2D, 2.5D, and 3D particles, with decreasing throughput as the complexity and dimensions of the structure increase.[70] For instance, printing rates for sophisticated 3D particles are only a few particles per minute. Hence, one must deal with the complexity vs. throughput trade-off when using this technique. However, it poses challenges such as precise control over flow dynamics, synchronization of scanning printing speed with flow speed, and mass production of complex 3D geometries.[71, 72]

2.4.3 Multi-photon, multi-focus 3D printing

Further advancements in the field of multi-photon 3D printing have been achieved by incorporating a 3D-printed diffractive optical element (DOE) and a multi-lens array to enable a multi-photon, multi-focus 3D laser printer.[73] Using 49 simultaneous laser foci generated in a 7 $\times$ 7 grid,

the fabrication process necessarily is faster than conventional single-focus systems. The benefits of using this method include increased printing speed and the ability to produce complex 3D geometries. However, the method has limitations: a greater number of laser foci at a fixed field of view (FOV) can only be achieved by decreasing the spacing between adjacent foci, which results in reduced focus quality and uneven laser intensity distribution, thereby limiting the complexity of the printed structures.[73]

2.4.4 Holographic patterning of light for 3D printing

The limitations of other techniques can to some extent be addressed in the technique of printing 3D geometries using holographic patterning of light fields. It is an advanced method that utilizes the principles of holography to print complex volumetric structures with high precision. The complex light field can be projected using a hologram of a three-dimensional interference pattern of light waves. The photocurable material is selectively polymerized at desired points to achieve volumetric shapes by modulating the light's intensity and phase, resulting in the simultaneous fabrication of entire 3D geometries. One example demonstrates that complex 3D shapes can be printed by the superposition of optical light patterns from multiple beams projected simultaneously.[74] Although it has higher printing rates, the use of multiple beams poses limitations and increases complexity in the setup. In this study, the prismatic nature of the superimposed beams puts geometric constraints on the fabricated structures.[74].

Another promising direction for fast printing is using a digital holography-based TPL (two-photon lithography) platform for ultrafast 3D nanoprinting.[75]. The setup uses a 1kHz femtosecond laser amplifier to enable printing with up to 2000 holography-based foci, providing control of intensity, phase, and location for each individually. The parallel printing is excellent for rapid fabrication, but a larger number of foci compromises the quality, intensity distribution, and also increases the risk of overpolymerization due to the close spacing of laser focal points.[73, 75]

The underlying physics of 3D printing has already been extensively discussed in the context of various optics-based 3D printing techniques.[76] In this domain, the development of 3D holographic multi-photon nanoprinting using a single, spatiotemporally shaped, short laser pulse is particularly exciting.[77] This would enable printing all the voxels in a single short laser pulse. However, while this approach shows great potential for rapid 3D fabrication, its implementation could be not only very expensive, as it requires a complex and costly printing setup, but also very challenging, as all the voxels simultaneously need a high light intensity to polymerize in a two-photon absorption process, which would require more sensitive inks. Moreover the hologram is static.

Hence, to utilize the power of holographic patterning—allowing faster production times and the creation of complex geometries without requiring support structures—and to avoid the challenges in digital holography-based TPL, we believe that one-photon holographic printing would be highly beneficial if advanced to the next level for single-exposure and large-scale fabrication. This is described in chapter 5.

2.5 Optics and director alignment

This section introduces the fundamentals, mathematical derivations, and plots necessary to understand the optics related to 3D director alignment. This discussion is referenced from the literature [78–81], especially 2.5.1 is referred from chapter 23 of ref [80] and chapter 22 of [78]; 2.5.2 is referred from [82] and furthermore, detailed derivations are provided to correct a mistake in the expression presented in Eq. (13) of [82] and to understand the relationship between the extraordinary-wave direction and the incidence angle in a birefringent material; 2.5.5 is referred from [82]; 2.5.6 is referred form chapter 22 of [80]. Some parts of this section have also been published and are included in the supplementary material of our published article [44].

2.5.1 Derivation of effective refractive index

Consider a monochromatic wave propagating in a medium that is nonmagnetic having zero volume charge ($\rho = 0$) and zero conduction current ($\vec{J} = 0$) then the Maxwell's relations can be written as (Eq. 22.1 in [78])

$$\nabla \times \vec{E} = -\mu_0 \frac{\partial \vec{H}}{\partial t} \tag{2.24}$$

$$\nabla \times \vec{H} = \frac{\partial \vec{D}}{\partial t} \tag{2.25}$$

$$\nabla \cdot \vec{H} = 0 \tag{2.26}$$

$$\nabla \cdot \vec{D} = 0 \tag{2.27}$$

Now considering the wave propagation along the direction $\vec{k}$, the field oscillations in the harmonic representation can be represented by (Eq. 22.2 in [78] and Eq. 15-16 of chapter 22 in [80])

$$\vec{E} = \vec{E}_0 e^{i(\vec{k}\cdot\vec{r}-\omega t)} \tag{2.28}$$

$$\vec{H} = \vec{H}_0 e^{i(\vec{k}\cdot\vec{r}-\omega t)} \tag{2.29}$$

$$\vec{D} = \vec{D}_0 e^{i(\vec{k}\cdot\vec{r}-\omega t)} \tag{2.30}$$

On combining these relations with Maxwell's equation, one can get

$$\vec{k} \times \vec{E} = \mu_0 \omega \vec{H} \tag{2.31}$$

$$\vec{k} \times \vec{H} = -\omega \vec{D} \tag{2.32}$$

$$\vec{k} \cdot \vec{H} = 0 \tag{2.33}$$

$$\vec{k} \cdot \vec{D} = 0 \tag{2.34}$$

Combining the equations 2.31 and 2.32 (Eq. 22.4 in [78])

$$\vec{k} \times (\vec{k} \times \vec{E}) = \mu_0 \omega (\vec{k} \times \vec{H}) = -\mu_0 \omega^2 \vec{D} \tag{2.35}$$

Consider that the medium is linear where the $\vec{D}$ and $\vec{E}$ are related in terms of the dielectric tensor as [78, 80]

$$D_i = \epsilon_0 \sum_{j=1}^{3} \epsilon_{ij} E_j \tag{2.36}$$

where ϵ_{ij} denote the nine dielectric tensor ($\hat{\epsilon}_r$) coefficients. The relation from the Eq. 2.36 can be written as (Eq. 22.8 in [78])

$$\begin{pmatrix} D_x \\ D_y \\ D_z \end{pmatrix} = \begin{pmatrix} \epsilon_{xx} & \epsilon_{xy} & \epsilon_{xz} \\ \epsilon_{yx} & \epsilon_{yy} & \epsilon_{yz} \\ \epsilon_{zx} & \epsilon_{zy} & \epsilon_{zz} \end{pmatrix} \begin{pmatrix} E_x \\ E_y \\ E_z \end{pmatrix} \tag{2.37}$$

For electromagnetic waves in anisotropic media, the dielectric matrix can be considered as Hermitian, with real diagonal entries ϵ_{xx}, ϵ_{yy}, ϵ_{zz}, and its off-diagonal entries being complex-conjugated.[78, 81] If all the elements of ϵ_{ij} are real, then the matrix is symmetric along the diagonal, indicating a non-optically active medium. On the other hand, in optically active media, certain elements must be treated as complex. [78, 81]

For the case of real symmetric matrices, the dielectric matrix can be represented in diagonal form, along the principal Cartesian axes as (Eq. 22.10 in [78])

$$\hat{\epsilon}_r = \begin{pmatrix} \epsilon_x & 0 & 0 \\ 0 & \epsilon_y & 0 \\ 0 & 0 & \epsilon_z \end{pmatrix} = \begin{pmatrix} n_x^2 & 0 & 0 \\ 0 & n_y^2 & 0 \\ 0 & 0 & n_z^2 \end{pmatrix} \tag{2.38}$$

In this context, ϵ_x, ϵ_y, and ϵ_z are considered as the principal dielectric constants, which are

associated with the squares of the principal refractive indices n_x^2, n_y^2, and n_z^2, respectively. As derived from Eq. 2.35, it follows that

$$\vec{k} \times (\vec{k} \times \vec{E}) = -\mu_0 \omega^2 \vec{D} \tag{2.39}$$

This relation can be written in principal axis representation as (Eq. 22.11 in [78])

$$\vec{k} \times (\vec{k} \times \vec{E}) = -\mu_0 \omega^2 \epsilon_0 \hat{\epsilon}_r \vec{E} \tag{2.40}$$

$$\vec{k} \times (\vec{k} \times \vec{E}) = -\frac{\omega^2}{c^2} \hat{\epsilon}_r \vec{E} \tag{2.41}$$

$$\vec{k} \times (\vec{k} \times \vec{E}) + k_0^2 \hat{\epsilon}_r \vec{E} = 0 \tag{2.42}$$

here, $c = \frac{\omega}{k_0}$ and k_o is the free space wavenumber.

Consider that the anisotropic birefringent medium has its optic axis along the z-direction in the principal axis system. Let us assume that the x- and y-dielectric components are the same, which leads to $n_x = n_y = n_o$ and $n_z = n_e$. (Eq. 3 in [81] and Eq. 22.26 in [78])

$$\hat{\epsilon}_r = \begin{pmatrix} \epsilon_x & 0 & 0 \\ 0 & \epsilon_x & 0 \\ 0 & 0 & \epsilon_z \end{pmatrix} = \begin{pmatrix} n_o^2 & 0 & 0 \\ 0 & n_o^2 & 0 \\ 0 & 0 & n_e^2 \end{pmatrix} \tag{2.43}$$

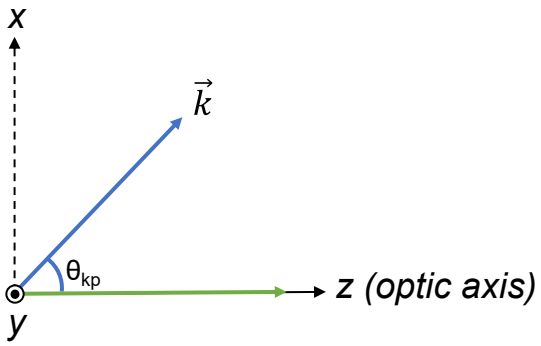

Figure 2.4: Schematic showing the coordinate frame of a wave propagating in the x-z plane with the optic axis along the z direction. The angle θ_{kp} is the angle between the propagation vector and the optic axis. The figure and caption are adapted from [80].

Consider the wave vector in the x-z plane: $\vec{k} = (k_x, 0, k_z)$ and the electric field vector $\vec{E} = (E_x, E_y, E_z)$. The relation 2.42 for each component can be written as (Eq. 4-6 in [81] and Eq.

22.15 in [78])

$$-k_z^2 E_x + k_z k_x E_z + k_o^2 n_o^2 E_x = 0 \tag{2.44}$$

$$-k_z^2 E_y - k_x^2 E_y + k_o^2 n_o^2 E_y = 0 \tag{2.45}$$

$$-k_x^2 E_z + k_x k_z E_x + k_o^2 n_e^2 E_z = 0 \tag{2.46}$$

As indicated in Figure 2.4, $\vec{k} = k(\sin\theta_{kp}, 0, \cos\theta_{kp})$, where $|\vec{k}| = k = \frac{\omega}{c} n_w = k_o n_w$. Here, the wave refractive index in the medium is n_w, and for the wave traveling along the optic axis, it is subject to the n_o refractive index. These relations can be expressed as (Eq. 92-94 in section 22.12.1 in [80])

$$\left(n_o^2 - n_w^2 \cos^2\theta_{kp}\right) E_x + n_w^2 \sin\theta_{kp} \cos\theta_{kp} E_z = 0 \tag{2.47}$$

$$\left(n_o^2 - n_w^2\right) E_y = 0 \tag{2.48}$$

$$n_w^2 \sin\theta_{kp} \cos\theta_{kp} E_x + \left(n_e^2 - n_w^2 \sin^2\theta_{kp}\right) E_z = 0 \tag{2.49}$$

The solutions can be found by setting the determinant equal to zero. The relation 2.48 is only dependent on the E_y component, and relations 2.47, 2.49 only on the E_x and E_z components.

Solution:1

With a y-polarized wave, one can consider $E_y \neq 0$ and $E_x = E_z = 0$. The relation 2.48 can be written as (Eq. 95 of section 22.12.1 in [80])

$$n_o^2 - n_w^2 = 0 \tag{2.50}$$

$$\text{Refractive index: } n_w = n_o \tag{2.51}$$

$$\text{Wave velocity: } v_w = v_{wo} = \frac{c}{n_o} \tag{2.52}$$

So, this wave is the ordinary wave (O-wave) with y-polarized $\vec{E}$ with its wave velocity independent of direction of propagation. (Eq. 96 of section 22.12.1 in [80])

Solution:2

Here, the wave is polarized in the plane x-z perpendicular to the y-axis with $E_y = 0$ and $E_x \& E_y \neq 0$. This results in $D_y = \epsilon_y E_y = 0$ that both $\vec{D}$ and $\vec{E}$ are in the x-z plane. (Eq. 97 of section 22.12.1 in [80])

Writing $\frac{E_z}{E_x}$ from relations 2.47 and 2.49 can be expressed as (Eq. 97 of section 22.12.1 in [80])

$$\frac{E_z}{E_x} = \frac{n_o^2 - n_w^2 \cos^2\theta_{kp}}{-n_w^2 \sin\theta_{kp}\cos\theta_{kp}} = \frac{n_w^2 \sin\theta_{kp}\cos\theta_{kp}}{-(n_e^2 - n_w^2 \sin^2\theta_{kp})} \tag{2.53}$$

$$(n_e^2 - n_w^2 \sin^2\theta_{kp})(n_o^2 - n_w^2 \cos^2\theta_{kp}) = (n_w^2 \sin\theta_{kp}\cos\theta_{kp})(n_w^2 \sin\theta_{kp}\cos\theta_{kp}) \tag{2.54}$$

$$n_e^2 n_o^2 - n_e^2 n_w^2 \cos^2\theta_{kp} - n_o^2 n_w^2 \sin^2\theta_{kp} + n_w^4 \cos^2\theta_{kp}\sin^2\theta_{kp} = n_w^4 \sin^2\theta_{kp}\cos^2\theta_{kp} \tag{2.55}$$

$$n_e^2 n_o^2 - n_e^2 n_w^2 \cos^2\theta_{kp} - n_o^2 n_w^2 \sin^2\theta_{kp} = 0 \tag{2.56}$$

$$n_e^2 n_o^2 = n_e^2 n_w^2 \cos^2\theta_{kp} + n_o^2 n_w^2 \sin^2\theta_{kp} \tag{2.57}$$

Dividing by $n_e^2 n_o^2 n_w^2$, we get: (Eq. 98 of section 22.12.1 in [80])

$$\frac{1}{n_w^2} = \frac{\cos^2\theta_{kp}}{n_o^2} + \frac{\sin^2\theta_{kp}}{n_e^2} \tag{2.58}$$

The refractive index n_w is given by: (Eq. 98 of section 22.12.1 in [80])

$$n_w = n_{we} = \frac{n_o n_e}{\sqrt{n_e^2 \cos^2\theta_{kp} + n_o^2 \sin^2\theta_{kp}}} \tag{2.59}$$

The wave velocity v_{we} is:

$$v_{we} = \frac{c}{n_{we}} = \frac{c\sqrt{n_e^2 \cos^2\theta_{kp} + n_o^2 \sin^2\theta_{kp}}}{n_o n_e} \tag{2.60}$$

This wave is an extraordinary wave (E-wave), as its refractive index and wave velocity depend on the propagation direction. For Solution 2, it is assumed that the E-wave is polarized in the x-z plane, orthogonal to the O-wave in Solution 1.

Typically, an E-wave does not propagate uniformly in all directions through a birefringent crystal. As a result, the E-ray, which represents the direction of the energy vector, is generally considered not to follow Snell's law. (page 358, chapter 8 in [79])

2.5.2 Refraction at the interface of birefringent media

Consider a plane wave with a propagation vector $\vec{k_1}$ incident on the interface between an isotropic material and a birefringent medium. Upon entering the birefringent material, the wave splits into two components: the ordinary wave (O-wave) and the extraordinary wave (E-wave). The phase matching conditions at the interface of the two materials are as follows ([78, 80] and Eq. 1 in [82])

$$\vec{k_1} \cdot \vec{r} = \vec{k_o} \cdot \vec{r} \quad \text{for the O-wave} \tag{2.61}$$

$$\vec{k_1} \cdot \vec{r} = \vec{k_e} \cdot \vec{r} \quad \text{for the E-wave} \tag{2.62}$$

here $\vec{r}$ is a position vector of a point on the surface. According to the Snell's law for each component: (Eq. 46-47 in section 22.5.2 in [80] and Eq. 2-3 in [82])

$$n_i \sin\theta_i = n_o \sin\theta_o \quad \text{for the O-wave} \tag{2.63}$$

$$n_i \sin\theta_i = n_{\text{eff}} \sin\theta_e \quad \text{for the E-wave} \tag{2.64}$$

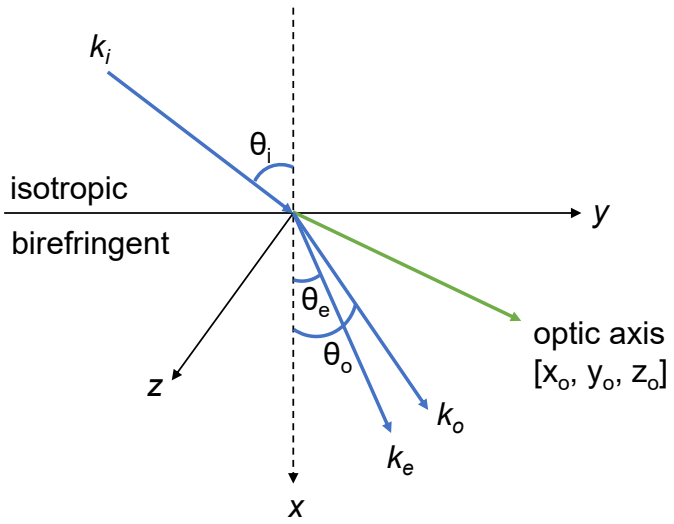

Figure 2.5: Schematic showing of the refraction at the interface of an isotropic and a birefringent material. The figure and caption are adapted from [44].

As derived earlier, the refractive index n_o is independent of the wave propagation vector $\vec{k_o}$, while the effective refractive index n_{eff} depends on the wave propagation vector $\vec{k_e}$, as given by relation 2.59.

$$n_{\text{eff}} = n_w = \frac{n_o n_e}{\sqrt{n_o^2 \sin^2\theta_{kp} + n_e^2 \cos^2\theta_{kp}}} \tag{2.65}$$

Here, the angle θ_{kp} is between the optic axis and wave vector k_e. Hence, the E-wave following the Snell's law can be written as

$$n_i \sin\theta_i = \frac{n_o n_e}{\sqrt{n_o^2 \sin^2\theta_{kp} + n_e^2 \cos^2\theta_{kp}}} \sin\theta_e \tag{2.66}$$

To derive the relation of angle θ_e with angle of incidence θ_i, we need to check the relation of angles θ_{kp} and θ_e.

Let the direction cosines of the optic axis be denoted as x_o, y_o, and z_o. We know that after refraction, the extraordinary wave (E-wave) propagates within the plane of incidence. Consequently, the direction cosines for the wave vector $\vec{k}_e$ can be expressed as $\cos\theta_e$, $\sin\theta_e$, and 0. Therefore, the projection of the E-wave onto the optic axis is given by the dot product of these two vectors. (Eq. 10 in [82])

$$\cos\theta_{kp} = x_o \cos\theta_e + y_o \sin\theta_e \tag{2.67}$$

Using this relation, we can find the value of n_{eff} in terms of θ_e, by substituting it into the equation 2.66: (Eq. 11 in [82])

$$n_{\text{eff}} = \frac{n_o n_e}{\sqrt{n_o^2\left[1 - (x_o \cos\theta_e + y_o \sin\theta_e)^2\right] + n_e^2 (x_o \cos\theta_e + y_o \sin\theta_e)^2}} \tag{2.68}$$

From Snell's law 2.64, we know that:

$$n_{\text{eff}} = \frac{n_i \sin\theta_i}{\sin\theta_e} \tag{2.69}$$

Substituting this relation into Eq. (2.68) and squaring both sides, we get:

$$n_o^2\left[1 - (x_o \cos\theta_e + y_o \sin\theta_e)^2\right] + n_e^2 (x_o \cos\theta_e + y_o \sin\theta_e)^2 = \frac{n_o^2 n_e^2 \sin^2\theta_e}{n_i^2 \sin^2\theta_i} \tag{2.70}$$

$$\begin{aligned} & n_o^2 - n_o^2\left(x_o^2 \cos^2\theta_e + y_o^2 \sin^2\theta_e + 2x_o y_o \cos\theta_e \sin\theta_e\right) \\ & + n_e^2\left(x_o^2 \cos^2\theta_e + y_o^2 \sin^2\theta_e + 2x_o y_o \cos\theta_e \sin\theta_e\right) \\ & = \frac{n_o^2 n_e^2 \sin^2\theta_e}{n_i^2 \sin^2\theta_i} \end{aligned} \tag{2.71}$$

Expanding and simplifying:

$$\begin{aligned} n_o^2 + \left(-n_o^2 x_o^2 + n_e^2 x_o^2\right)\cos^2\theta_e + \left(-n_o^2 y_o^2 + n_e^2 y_o^2\right)\sin^2\theta_e \\ + \left(2n_e^2 x_o y_o - 2n_o^2 x_o y_o\right)\cos\theta_e \sin\theta_e \\ = \frac{n_o^2 n_e^2 \sin^2\theta_e}{n_i^2 \sin^2\theta_i} \end{aligned} \tag{2.72}$$

Dividing by $\sin^2\theta_e$:

$$\begin{aligned} \frac{n_o^2}{\sin^2\theta_e} + \left(-n_o^2 x_o^2 + n_e^2 x_o^2\right)\cot^2\theta_e + \left(-n_o^2 y_o^2 + n_e^2 y_o^2\right) \\ + \left(2n_e^2 x_o y_o - 2n_o^2 x_o y_o\right)\cot\theta_e \\ = \frac{n_o^2 n_e^2}{n_i^2 \sin^2\theta_i} \end{aligned} \tag{2.73}$$

Using the following relation:

$$\frac{1}{\sin^2\theta_e} = 1 + \cot^2\theta_e \tag{2.74}$$

We can write Eq. 2.73 as: (Eq. 12 in [82])

$$\begin{aligned} n_o^2\left(1 + \cot^2\theta_e\right) + \left(-n_o^2 x_o^2 + n_e^2 x_o^2\right)\cot^2\theta_e \\ + \left(-n_o^2 y_o^2 + n_e^2 y_o^2\right) + \left(2n_e^2 x_o y_o - 2n_o^2 x_o y_o\right)\cot\theta_e \\ = \frac{n_o^2 n_e^2}{n_i^2 \sin^2\theta_i} \end{aligned} \tag{2.75}$$

$$\begin{aligned} \left[n_o^2 + x_o^2\left(n_e^2 - n_o^2\right)\right]\cot^2\theta_e + 2x_o y_o\left(n_e^2 - n_o^2\right)\cot\theta_e \\ + \left[n_o^2 + \left(n_e^2 - n_o^2\right)y_o^2 - \frac{n_o^2 n_e^2}{n_i^2 \sin^2\theta_i}\right] = 0 \end{aligned} \tag{2.76}$$

We obtain a quadratic equation in $\cot\theta_e$:

$$a\cot^2\theta_e + b\cot\theta_e + c = 0 \tag{2.77}$$

The roots of this equation are:

$$\cot\theta_e = \frac{-b \pm \sqrt{b^2 - 4ac}}{2a} \tag{2.78}$$

$$\begin{aligned} b^2 - 4ac = &\left[2x_o y_o \left(n_e^2 - n_o^2\right)\right]^2 \\ &- 4\left[n_o^2 + x_o^2\left(n_e^2 - n_o^2\right)\right]\left[n_o^2 + \left(n_e^2 - n_o^2\right)y_o^2 - \frac{n_o^2 n_e^2}{n_i^2 \sin^2\theta_i}\right] \end{aligned} \tag{2.79}$$

By comparing Eq. 2.76 and 2.78

$$\begin{aligned} b^2 - 4ac = &4x_o^2 y_o^2\left(n_e^2 - n_o^2\right)^2 \\ &- 4\left[n_o^4 + n_o^2 y_o^2\left(n_e^2 - n_o^2\right) - \frac{n_o^4 n_e^2}{n_i^2 \sin^2\theta_i}\right. \\ &+ n_o^2 x_o^2\left(n_e^2 - n_o^2\right) + x_o^2 y_o^2\left(n_e^2 - n_o^2\right)^2 \\ &\left.- x_o^2\left(n_e^2 - n_o^2\right)\frac{n_o^2 n_e^2}{n_i^2 \sin^2\theta_i}\right] \end{aligned} \tag{2.80}$$

$$b^2 - 4ac = 4n_o^2\left[\frac{n_o^2 n_e^2 + x_o^2 n_e^2\left(n_e^2 - n_o^2\right)}{n_i^2 \sin^2\theta_i} - \left(n_o^2 + \left(x_o^2 + y_o^2\right)\left(n_e^2 - n_o^2\right)\right)\right] \tag{2.81}$$

Now, using Eq. 2.78 and 2.81, the roots of Eq. 2.76 are:

$$\cot\theta_e = \frac{-2x_o y_o\left(n_e^2 - n_o^2\right) \pm 2n_o\sqrt{\frac{n_o^2 n_e^2 + x_o^2 n_e^2\left(n_e^2 - n_o^2\right)}{n_i^2 \sin^2\theta_i} - \left(n_o^2 + \left(x_o^2 + y_o^2\right)\left(n_e^2 - n_o^2\right)\right)}}{2\left[n_o^2 + x_o^2\left(n_e^2 - n_o^2\right)\right]} \tag{2.82}$$

This is the relation between the E-wave direction to the angle of incidence θ_i.

This section has closely followed the arguments and derivations of the ref [82] and the expression 2.82 has been derived previously in Eq. (13) of [82], but it contains an error. The error in [82] is found in the sign of the term under the square root in this equation, which is now corrected in expression 2.82.

2.5.3 Plots

To understand the consequence of relation 2.82, the following plots are presented for a birefringent medium with $n_o = 1.5$ and $n_e = 1.7$ and both the incidence plane and the optic axis are in the x-y plane.

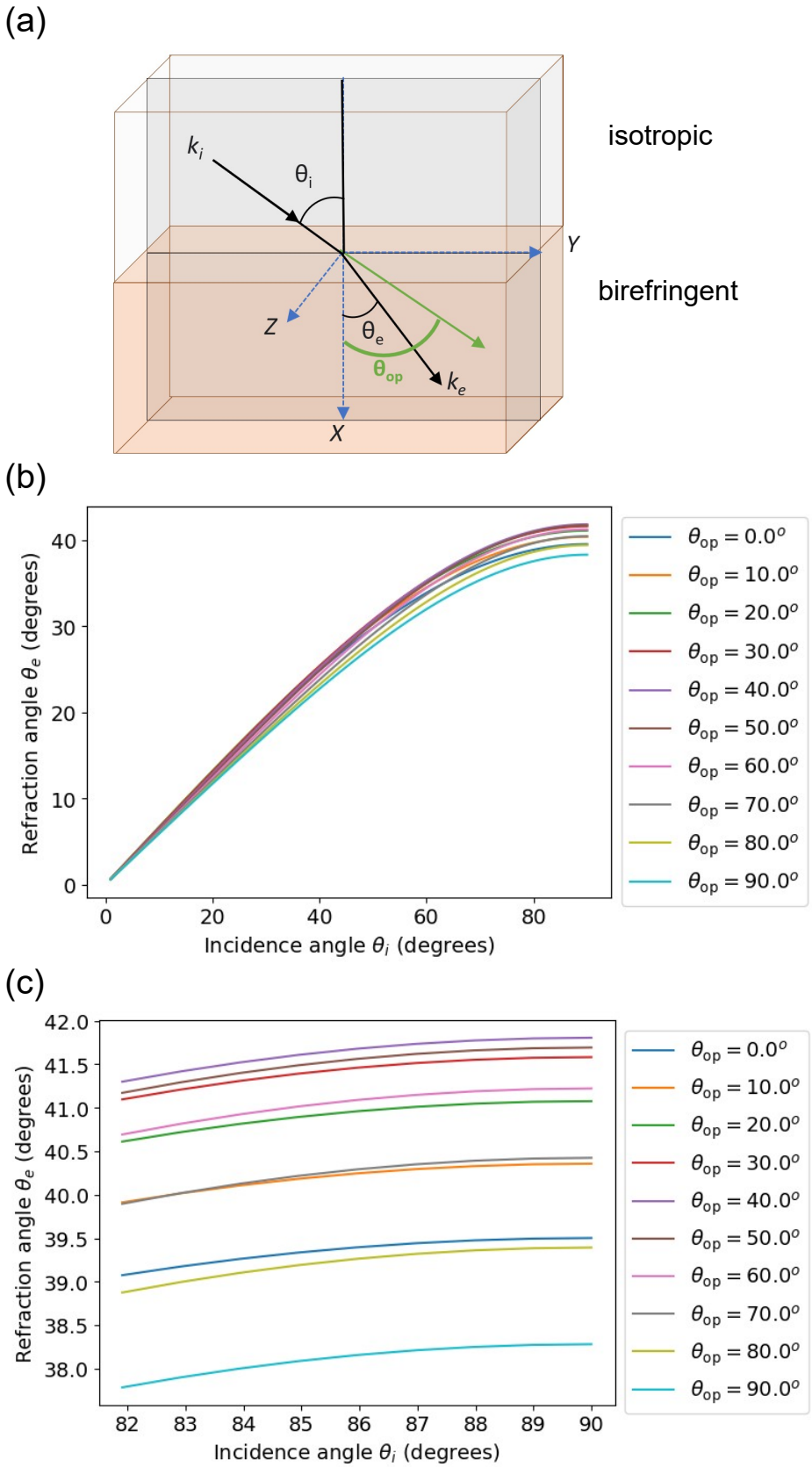

Figure 2.6: Varying the incidence angle for a fixed optic axis. (a) Schematic of the refraction angle of the extraordinary (E-) wave for any incidence angle at the interface between an isotropic and a birefringent medium. (b)-(c) Plots of the refraction angle θ_e, where different line plots correspond to a particular optic axis orientation in the crystal (θ_{op}). Plots (b) and (c) differ in the range of the incidence angles. The figure and caption are adapted from [44].

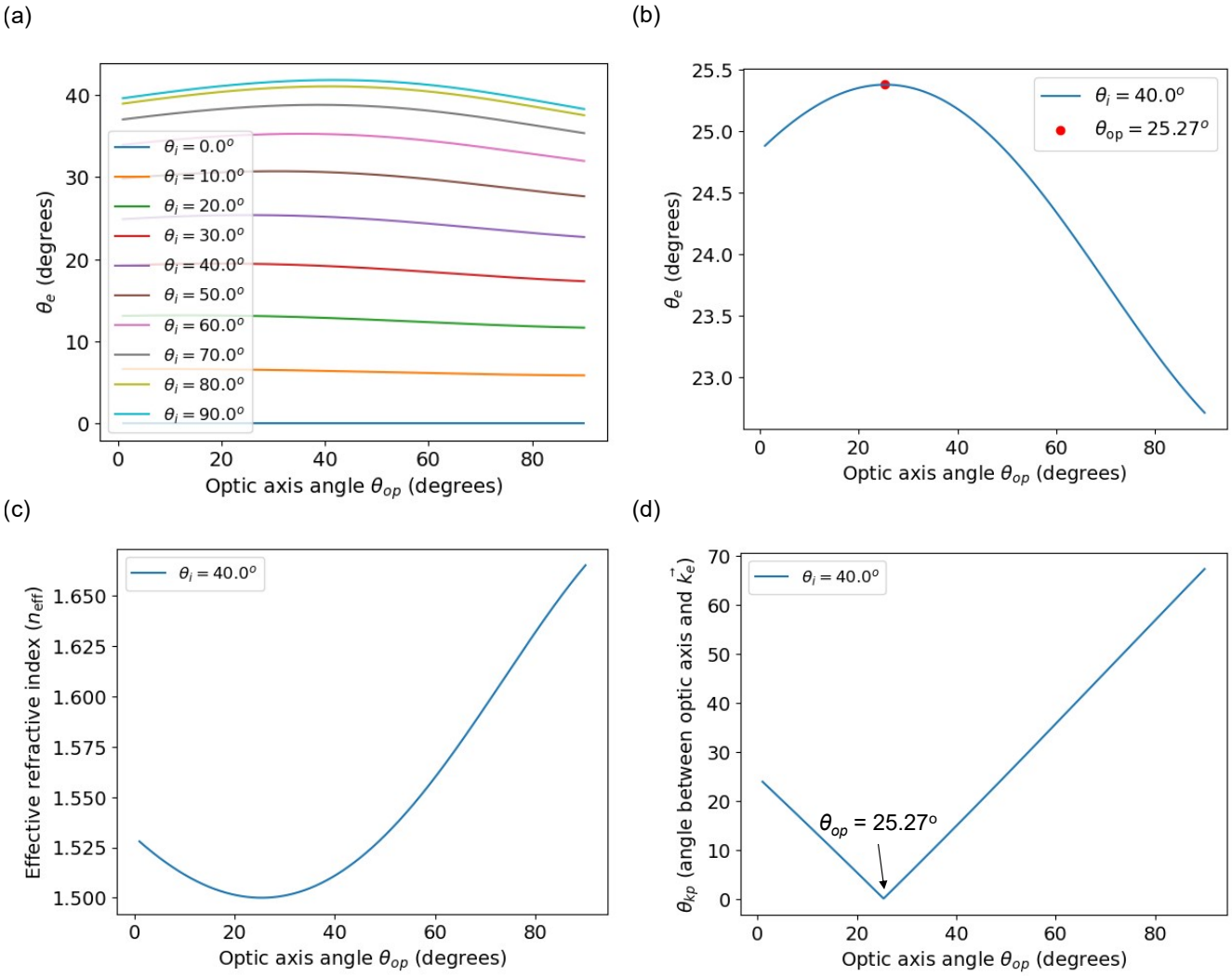

Figure 2.7: a) Plot of E-wave propagation versus optic axis orientation θ_{op} and fixed incidence angles (values of θ_i are shown in the label). b-d) Plots for the refraction angle θ_e, effective refractive index n_{eff}, and propagation direction of the E-wave relative to the optic axis θ_{kp}, respectively, at a fixed incidence angle of $\theta_i = 40°$. The red dot marker indicates the value of θ_{op} when the E-wave is propagating along the optic axis, with $\theta_e \sim \theta_{\text{op}}$, resulting in $\theta_{\text{kp}} = 0$ and $n_{\text{eff}} = 1.5$.

2.5.4 To find the divergence angle between E-wave and O-wave in a wedge cell

The subsequent procedure has been published in [44]. In the following a procedure is provided to determine the angle between the O- and E-wave which is needed to determine the director orientation in chapter 4.

Interface: 1 (isotropic to birefringent) Schematics of the wave propagation is shown in the Figure 2.8

- **Step-1:** Calculate the refraction angles θ_e, θ_o for a specific angle θ_i.
- **Step-2:** Calculate the value of θ_{kp}, the angle between the optic axis and $\vec{k}_e$, as

$$\cos\theta_{kp} = x_o \cos\theta_e + y_o \sin\theta_e \tag{2.83}$$

- **Step-3:** Calculate the value of the effective refractive index n_{eff}, using the value of θ_{kp} as

$$n_{\text{eff}} = \frac{n_o n_e}{\sqrt{n_o^2 \sin^2\theta_{kp} + n_e^2 \cos^2\theta_{kp}}} \tag{2.84}$$

Interface: 2 (birefringent to isotropic)

- **Step-4:** For a wedge angle δ, calculate the value of the angles for the e-wave and the o-wave as

$$\theta_{e_2} = \theta_e + \delta \quad \text{and} \quad \theta_{o_2} = \theta_o + \delta \tag{2.85}$$

- **Step-5:** Apply Snell's law for this interface to find the angles θ_{e_t} and θ_{o_t} as

$$n_{\text{eff}} \sin\theta_{e_2} = n_i \sin\theta_{e_t} \tag{2.86}$$

$$n_o \sin\theta_{o_2} = n_i \sin\theta_{o_t} \tag{2.87}$$

- **Step-6:** The divergence angle between the o- and e-waves is

$$\alpha = \theta_{e_t} - \theta_{o_t} \tag{2.88}$$

The divergence angle depends on both the incidence angle and the optic axis. This relationship is illustrated in Figure 2.9, where the incidence angle θ_i is varied while the optic axis θ_{op} is fixed, and in Figure 2.10, where the optic axis θ_{op} is varied while the incidence angle θ_i is fixed. As

seen, the relation of the splitting angle (divergence angle) is complex. The protocol can be further simplified to determine 3D director orientation is described in section 4.7, chapter 4 of this thesis.

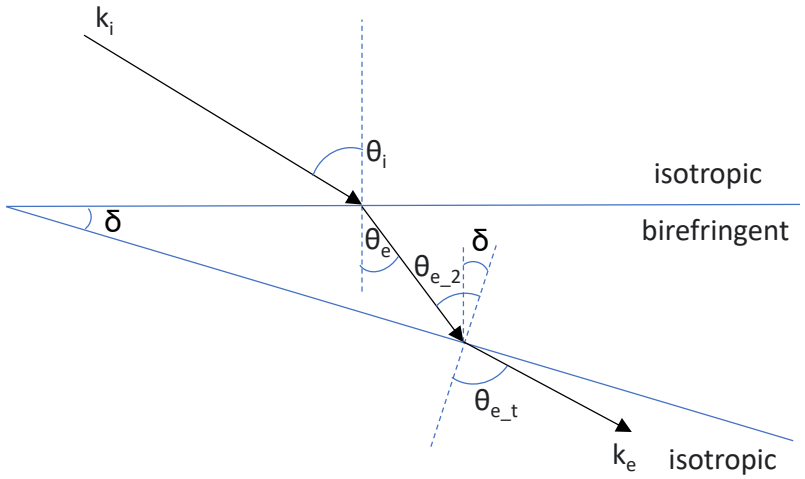

Figure 2.8: Schematic of the propagation direction of the E-wave at the two interfaces of the wedge cell with wedge angle δ. (The propagation vector for the ordinary wave is not shown in the schematic.)

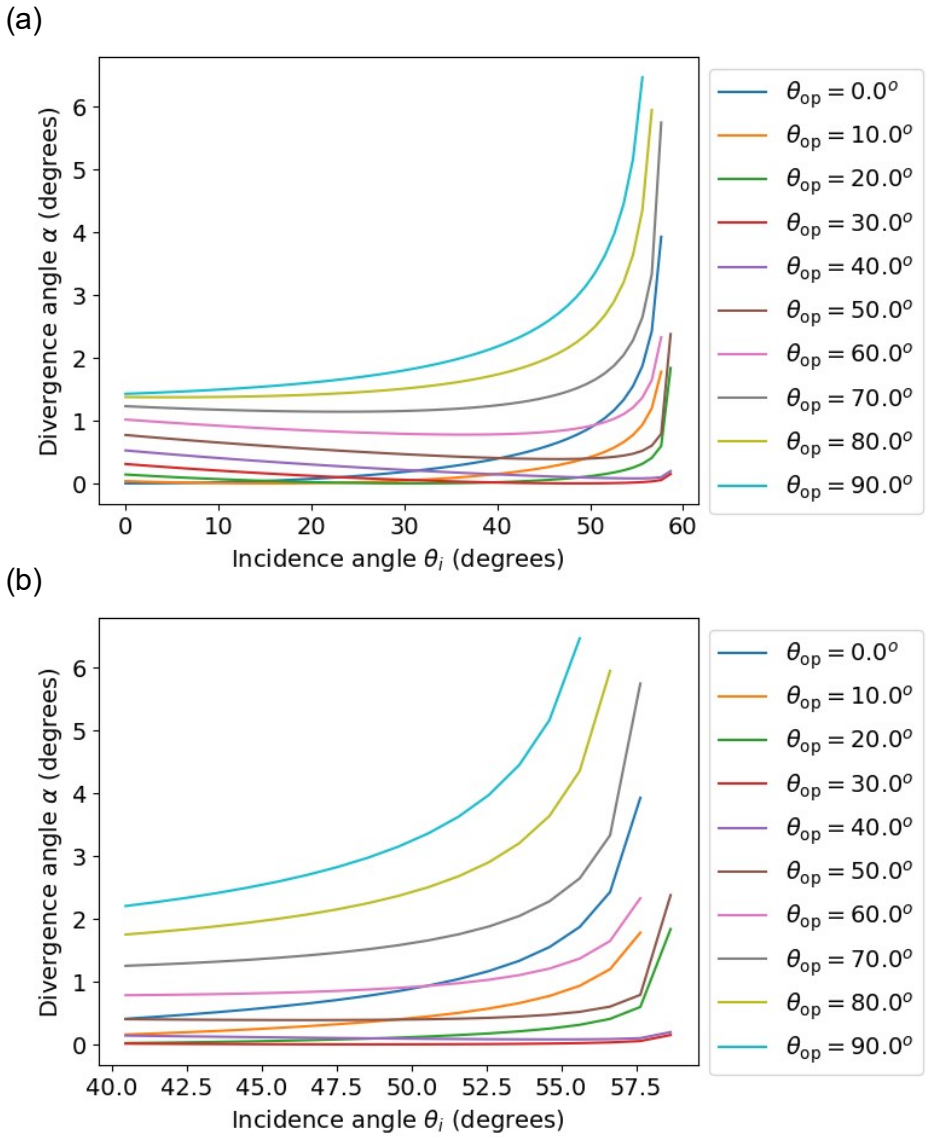

Figure 2.9: a-b) Divergence angle between E-wave and O-wave propagation after passing through the wedge cell at varying incidence angle and fixed optic axis at angles θ_{op} (values shown in the labels). The plots are for different ranges of incidence angle.

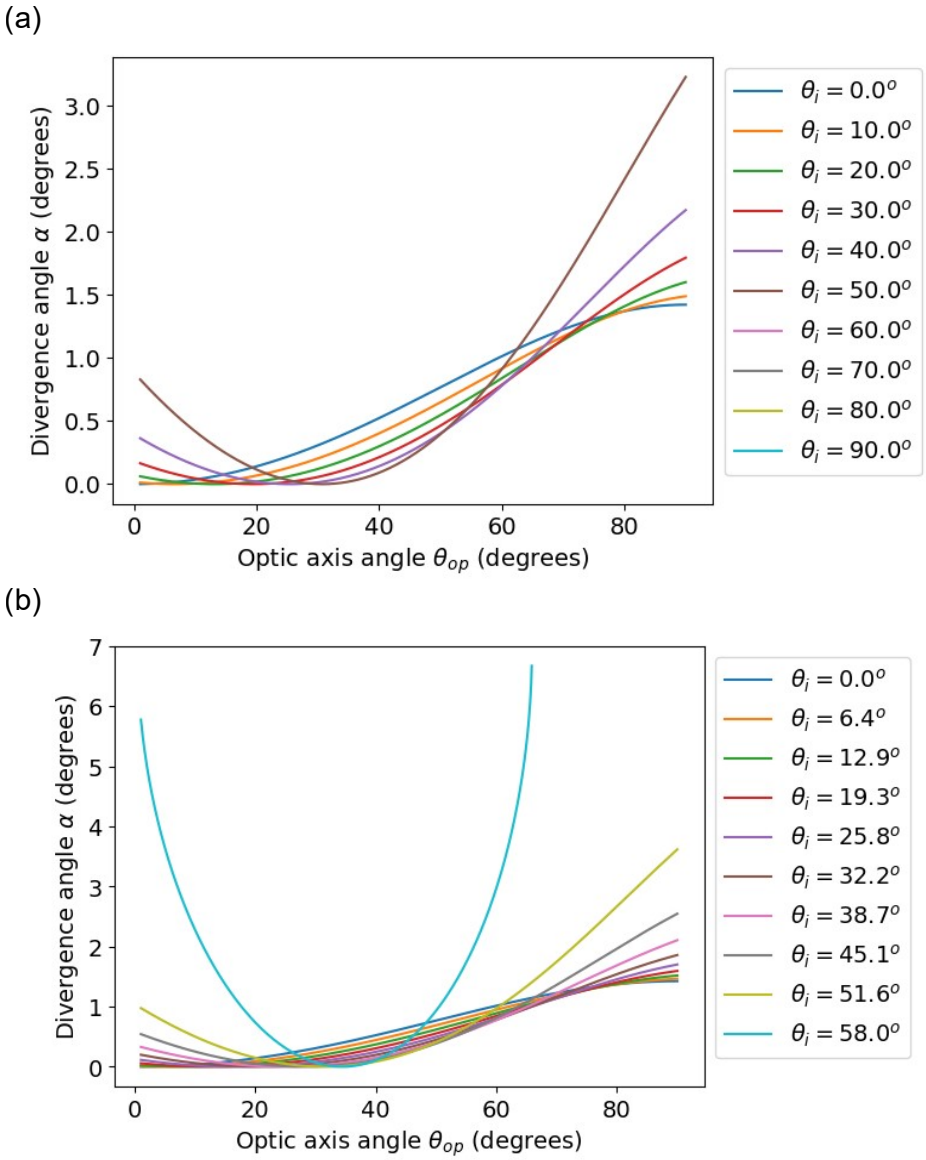

Figure 2.10: a-b) Divergence angle between E-wave and O-wave propagation after passing through the wedge cell at varying optic axis and fixed incidence angle at angles θ_i (values shown in the labels). The plots are for different ranges of incidence angle.

3 3D director alignment using low magnetic fields

3.1 Introduction

3D alignment in cross-linked liquid crystalline materials is particularly interesting for fabricating structures with complex director profiles and achieving intricate 3D actuation.[41–43, 53, 57–60, 83] Magnetic field alignment is promising for orienting the LC director in any arbitrary 3D orientation, independent of the structural geometry. The advantage of using magnetic field alignment is that larger samples, on the order of millimeters, can be easily aligned to fabricate large 3D structures which is particularly exciting for achieving complex 3D actuation in soft robotics.[41, 58] However, programming a 3D director using a magnetic field is challenging due to the weak effect of the field, requiring very high magnetic field strengths (0.5 T) to achieve alignment control.[83] The required field strength can be only reduced to 0.3 T if the LC ink is heated to temperatures near the isotropic transition temperature, T_{ni} (e.g., 100°C) during printing.[41] Therefore, it is desirable to reduce the magnetic field strength for easier and faster control of the director field in large-scale fabrication. Spatially controlling an arbitrary director is even more exciting as it allows for programming complex director profiles that vary with position and orientation, independent of the structural geometry, resulting in rich mechanical deformations. Here, we address these challenges and demonstrate 3D arbitrary alignment control using low magnetic fields (0.13 T), 3-4 times weaker than those reported in the literature.[41, 58, 83] We show that adding the mesogens 5CB and E7 to the ink can decrease the viscosity and enhance the alignment response, due to the large response of 5CB. Additionally, we successfully fabricated 2D and 3D liquid crystalline gels (LCGs) at room temperature with spatially varying 3D director profiles, demonstrating that this method has potential applications for the fabrication of soft liquid crystalline structures.

3.2 Motivation

The precise control of the 3D LC director using low magnetic fields at room temperature to pattern spatially varying arbitrary director profiles in 2D and 3D LC structures. The aim is to overcome the challenges of 3D alignment control and make the fabrication process easier and faster for complex LC soft robotic actuators.

3.3 Results

The work presented in this chapter has already been published in [44] and is in part reproduced in this chapter. I would like to thank Prof. Dr. Frank Gießelmann (University of Stuttgart) for the collaboration, for providing access to his microscopy lab facilities, and for valuable discussions; Dr. Carlos Sánchez-Somolinos (CSIC, Zaragoza) for his collaboration, for providing LC inks for this study, and insightful discussions; Prof. Dr. Eva Blasco (IMSEAM, Heidelberg) for providing samples and helpful discussions, Prof. Dr. Christine Selhuber-Unkel for providing lab facilities, and Dr. Dimitris Missirlis (MNMS group) for his help with rheological measurements.

3.4 Chemical inks and preparation

Figure 3.1 shows the molecular structures of the chemicals used. The reactive mesogens 4-bis[4-(3-acryloyloxypropyloxy)benzoyloxy]-2-methylbenzene (RM257), 4-Methoxybenzoicacid 4-(6-acryloyloxy-hexyloxy)phenyl ester (RM 105), and the E7 mixture, were ordered from Synthon Chemicals GmbH & Co. KG. The photo-initiator phenyl-bis(2,4,6-trimethylbenzoyl)phosphine oxide (TPO) was bought from Sigma–Aldrich. The radical inhibitor 2,6-di-tert-butyl-4-methylphenol (BHT) and LC 4-cyano-4-pentylbiphenyl (5CB) were bought from TCI Deutschland GmbH. All the chemicals were used as received.

Here I would like to mention that the chemicals RM257, RM105, E7 and TPO were inspired from [43, 60] and provided by Dr. Carlos Sánchez-Somolinos (CSIC, Zaragoza) and Dr. Eva Blasco (IMSEAM, Heidelberg); 5CB was provided by Prof. Dr. Frank Gießelmann (University of Stuttgart).

LCG-ink 1 has RM257 (16.4 wt%), RM105 (32.8 wt%), E7 (49.2 wt%), TPO (1.2 wt%) and BHT (0.4 wt%). The chemicals were dissolved in dichloromethane (DCM) and heated at 80°C with continuous magnetic stirring until all the DCM had evaporated. Upon slow cooling to room temperature, the ink transitioned to the nematic phase. LCG-ink 2 was prepared by further

adding 5CB (20 wt%) into LCG-ink 1. and hence contains RM257 (13.67 wt%), RM105 (27.33 wt%), E7 (41 wt%), TPO (1 wt%) and BHT(0.33 wt%). At the end, the inks were filtered to remove undissolved residues by using 0.45 um PTFE syringe filter (diameter 13 mm).

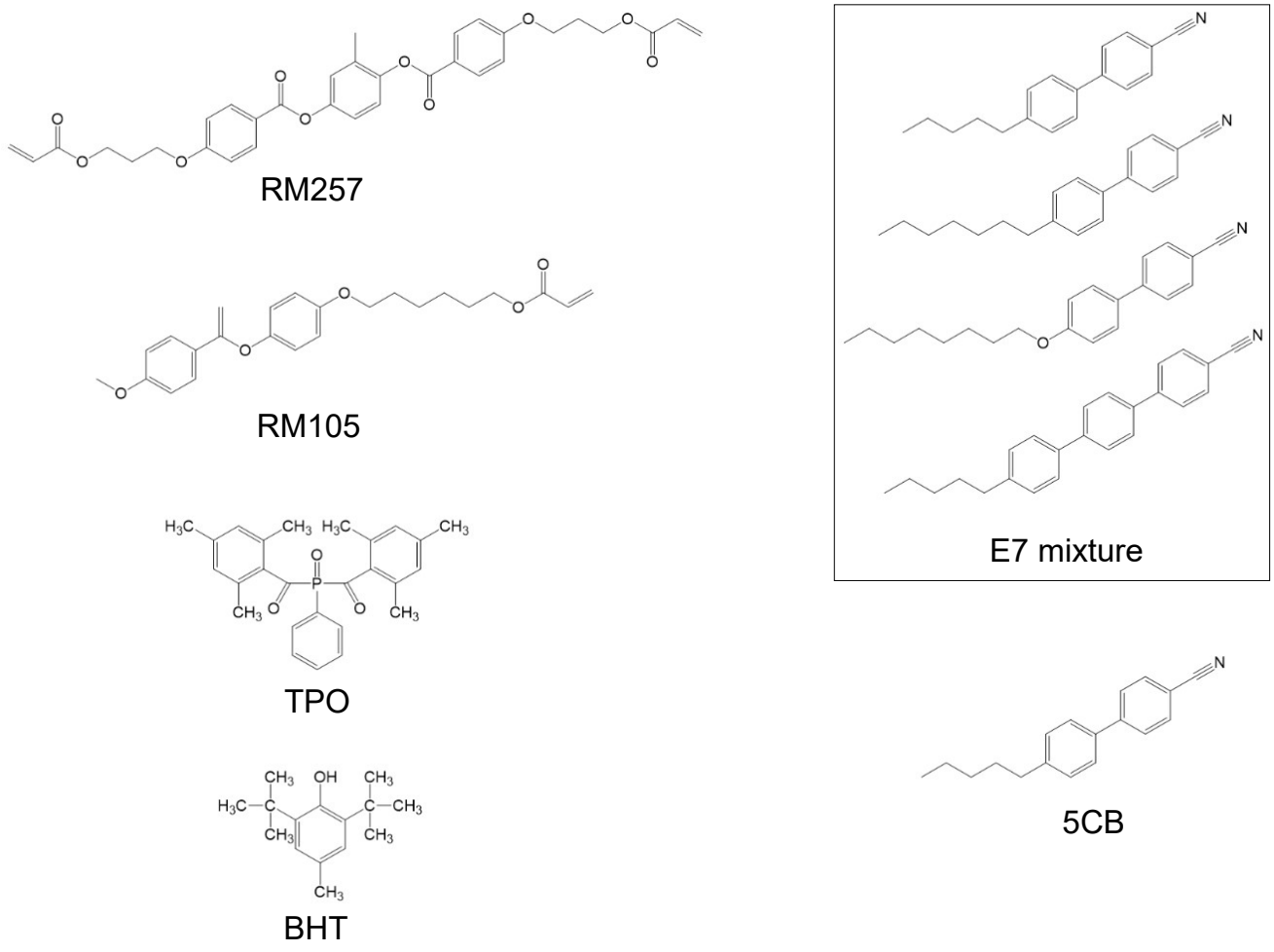

Figure 3.1: Chemical structures of the mesogens used to prepare the LC ink formulations. The figure and caption are adapted from [44].

3.5 Director alignment of LCG-inks using low magnetic fields

To apply a uniform magnetic field, two permanent magnets (surface field of 0.3 T) were placed opposite and parallel to each other in a 3D-printed holder with a spacing of 3.5 cm to obtain a 0.13 T field at the center, as shown in Figure 3.2a. The liquid crystal cell, made of two sandwiched 1 mm-thick glass substrates containing the LCG-ink, was placed at the center, and the director orientation was set by the applied magnetic field direction. This holder was rotated in-plane or out-of-plane to align the magnetic field orientation in the desired direction to achieve the 3D director alignment.

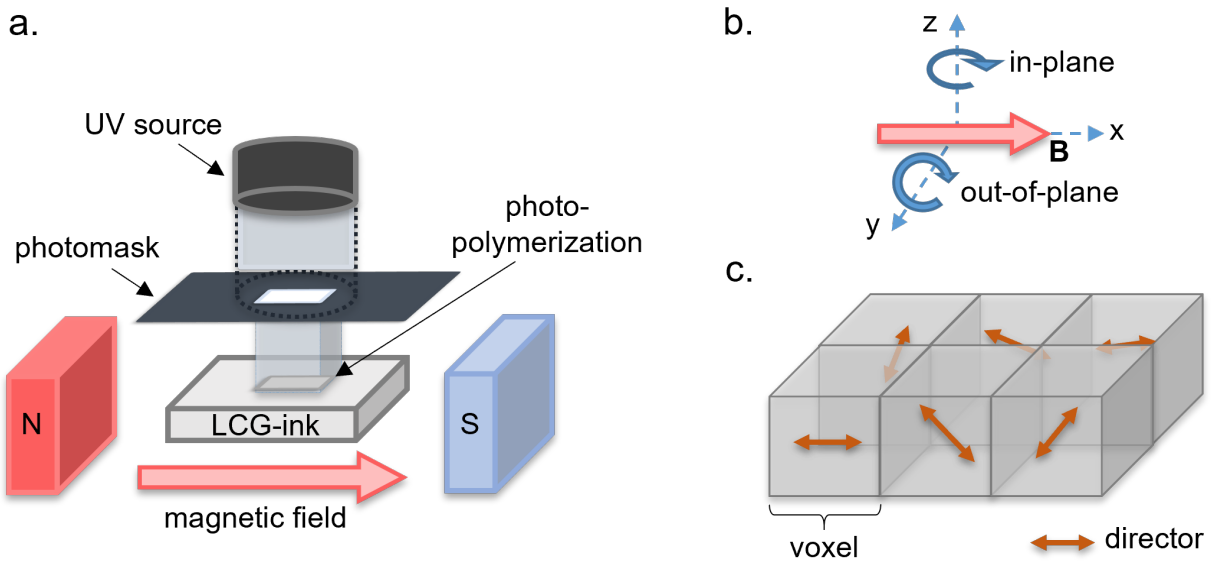

Figure 3.2: The schematics of the setup for magnetic field alignment of liquid crystalline gels (LCGs) are shown. a) A magnetic field of 0.1 to 0.15 T is applied using two magnets placed parallel and opposite to each other. The liquid crystal cell containing the LCG-ink is positioned at the center, where the director orientation is determined by the magnetic field direction. The size and shape of the desired voxel to be printed are controlled using a photomask placed on top of the cell. After 1-2 minutes, the director aligns, and the LCG-ink is photopolymerized using a UV light source to print a voxel, while the remaining ink stays unaffected in the liquid state. b) The magnetic field direction, and consequently the director orientation, can be controlled in any 3D orientation by rotating the magnet holder in-plane and out-of-plane within a range of 0° to 90°, as indicated by the rotation arrows. c) This process can be repeated to print voxels sequentially, as illustrated in the schematics, where the arrows represent the director orientation in each voxel. The figure and caption are adapted from [44].

We selected ink formulations with low viscosity to ensure that the molecules can easily rotate and align with the magnetic field. Among these, 5CB, due to its low viscosity, aligns effectively in response to magnetic fields due to its anisotropic magnetic susceptibility ($\Delta\chi = 2 \times 10^{-6}$).[84] Consequently, we first prepared the formulation LCG-ink 1, which has low viscosity and serves as a base into which 5CB can be mixed. The low viscosity of LCG-ink 1 is due to its high content (49.2

wt%) of the non-reactive mesogen E7, which dissolves all other chemicals in the formulation to achieve a nematic phase at room temperature. Subsequently, LCG-ink 2 was prepared by adding 20 wt% 5CB to LCG-ink 1. The viscosity of LCG-ink 2 was measured and compared with that of pure 5CB, as shown in Figure 3.3.

Viscosity measurements were performed using an HR20 rheometer (TA Instruments) in a parallel plate geometry with an 8 mm diameter upper plate. A 100 μL sample was carefully loaded between the parallel plates, with the gap manually set to 1.2 mm. The viscosity was measured at 25°C over a shear rate range of 10 to 100 s^{-1}.

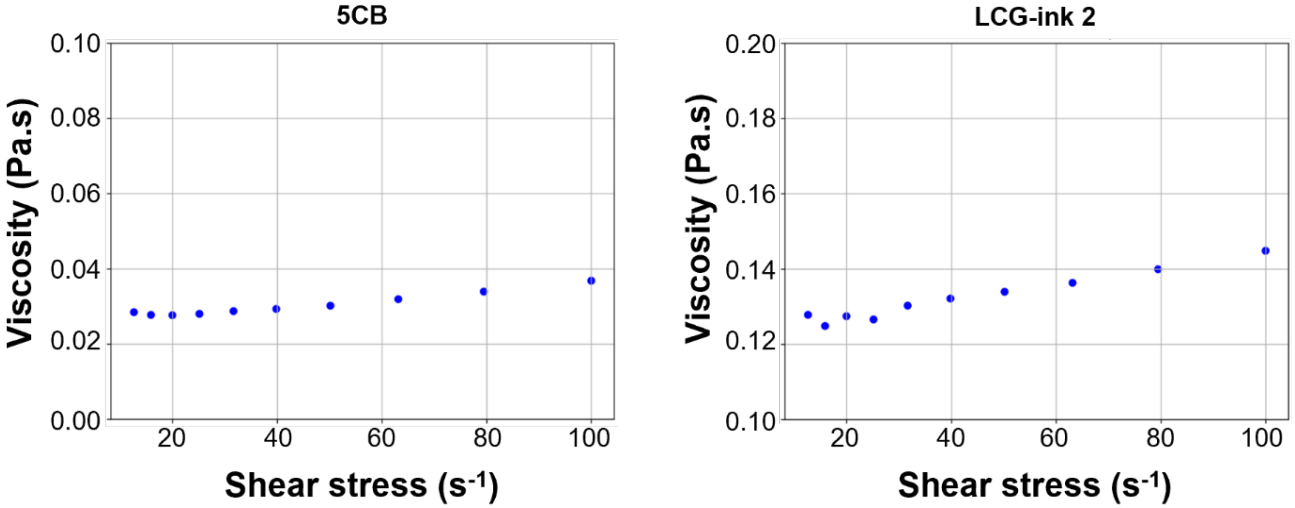

Figure 3.3: Viscosity measurements with varying shear stress. a) Plot of 5CB and b) LCG-ink 2. The figure is taken from and the caption is adapted from [44].

The aromatic LC molecules in the inks respond to magnetic field alignment due to their positive diamagnetic susceptibility and as a function of their viscosity, which affects their ability to reorient.[85, 86] The torque on the diamagnetic aromatic mesogens arises because of the presence of $\pi-$electrons.[13, 87] For example, the magnetic susceptibility of RM257 (1.87×10^{-6})[88] is 10 times that of 5CB (0.17×10^{-6})[89] because RM257 has three benzene rings compared to the two benzene rings in 5CB. However, RM257 has significantly higher viscosity (viscosity data for pure RM257 is not published, but it is known to be very viscous) and therefore needs to be heated near its isotropic transition temperature to align with magnetic fields, and even then, the alignment is relatively slow. Additionally, we measured that our LCG-ink 2 containing RM257 is more viscous compared to pure 5CB (see Table 3.1).

Although 5CB has lower magnetic susceptibility, its lower viscosity enables faster alignment at lower magnetic field strengths, as shown in Figure 3.3 and Table 3.1. Since 5CB molecules are uniformly dissolved in our ink, the application of an external magnetic field causes them to reorient and guide all other molecules in the ink to align in the magnetic field direction.

We compared the alignment response of the LCG-inks and 5CB at different magnetic field strengths. The table summarizes the response, where 'Y' and 'N' indicate whether the alignment response was observed or not, respectively.

Table 3.1: Summary of the magnetic field alignment response observed for LCG-ink 1, LCG-ink 2, and 5CB. Here, 'Y' indicates a birefringence change, and 'N' denotes no change under different magnetic field strengths. As observed, LCG-ink 2 aligns at lower field values compared to LCG-ink 1. The table and caption are adapted from [44].

S.No.	**Magnetic Field (Gauss)**	**LCG-ink 1**	**5CB**	**LCG-ink 2**
1	15	N	N	N
2	200	N	N	N
3	300	N	Y	Y
4	450	N	Y	Y
5	650	Y	Y	Y
6	900	Y	Y	Y
7	1300	Y	Y	Y

Initially, we studied the director alignment as a function of the applied magnetic field strength, determining the smallest magnetic field required to realign the director. The birefringence change was observed as a contrast change in the LC cell containing the ink under crossed polarizers. For these experiments, a sandwiched LC cell with a gap thickness of 250 μm was used to minimize the effect of surface anchoring on the director alignment, to observe the alignment effect caused by the magnetic field.

The glass substrates of the cell impart homeotropic alignment in the absence of a magnetic field, causing the sample to appear dark under crossed polarizers, as shown in Figure 3.4. An external magnetic field was applied in-plane at an angle of 45° to the polarizer axes. As seen in Figure 3.4, at $T = 0$ s, the sample appears dark due to the homeotropic alignment. Upon applying the magnetic field, the sample becomes brighter, indicating the alignment response to the field.

The visual contrast observations were used to determine the threshold field, defined as the lowest field required to align the director and produce a noticeable birefringence change. The data for different ink formulations is summarized in Table 3.1.

We observed that the LCG-ink 2 formulation containing 20% 5CB lowers the field threshold to match that of 5CB in the same LC cell configuration, without compromising the overall structural integrity. As shown in Table 3.1, the threshold field for LCG-ink 1 (without 5CB) is 650 Gauss, whereas LCG-ink 2 with 20% 5CB aligns at approximately 300 Gauss, similar to pure 5CB. Increasing the 5CB concentration beyond 20% does not reduce the threshold field below that of pure 5CB and, instead, negatively impacts the structural integrity of the ink. Therefore, 20% 5CB is considered the optimal balance between maintaining structural integrity and reducing the

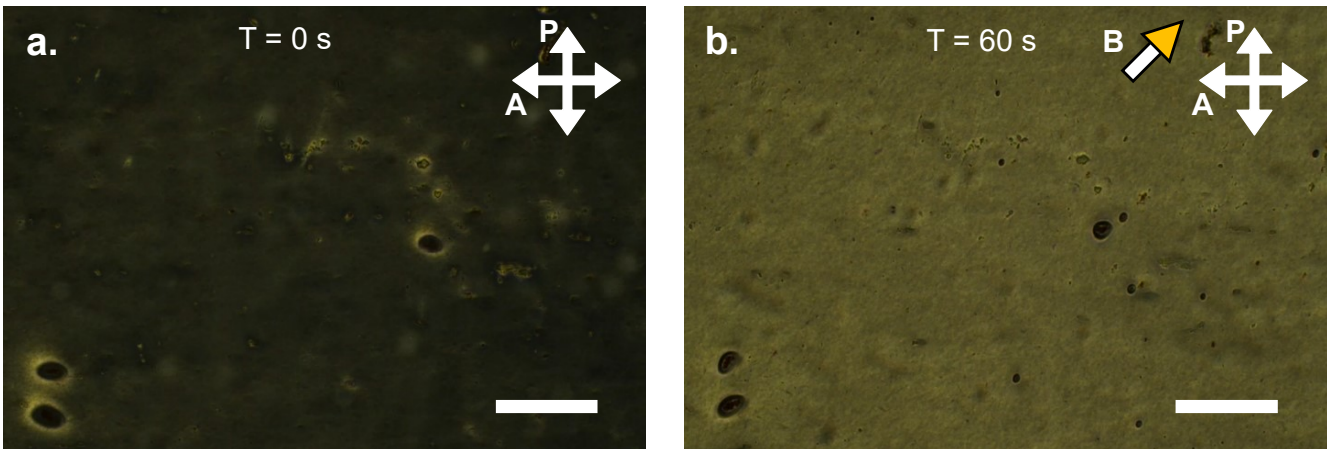

Figure 3.4: Polarization optically microscope images of the alignment observation in response to external magnetic field. a) Initally at t = 0s, the LC cell is homeotropically aligned and hence appears dark under crossed polarizers.b) Upon application of a magnetic field in the direction indicated by the arrow, the director realigns in-plane by 45° relative to the polarizer axes, and the sample appears brighter compared to its initial state. The alignment was observed to be stable after approximately 1 minute. The figure and caption are adapted from [44].

required threshold field. This demonstrates that lower magnetic field strengths are sufficient to reorient the director in the presence of non-reactive mesogens like 5CB and E7, compared to inks containing only reactive mesogens.

The director alignment is influenced by both the surface anchoring of the glass substrates and the magnetic fields. The surface anchoring effect decays exponentially with distance, and to reorient the director, the magnetic field must overcome this anchoring effect from the surface boundaries. Consequently, the threshold magnetic field depends on the cell thickness d, the elastic constant K, and the magnetic susceptibility $\Delta\chi$ of the LC: [13, 45, 85, 86, 88, 89] (see chapter 7, page 666 of [45], chapter 3, page 128 of [13])

$$B_0 = \frac{\pi}{d}\sqrt{\frac{K\mu_0}{\Delta\chi}} \tag{3.1}$$

Here, we use the material parameters of 5CB typically reported in the literature: $K = 10^{-11}$ N, $\Delta\chi = 4\pi \times 10^{-7}$, and $d = 250$ μm, as used in our experiments. Using Eq. 3.1, we estimate the threshold field B_0 to be 40 mT (400 Gauss), which agrees well with our observed threshold fields summarized in Table 3.1.

Similarly, the magnetic coherence length ξ indicates the distance over which the magnetic field influences the director alignment. The size of the coherence length corresponds to the minimum bulk sample volume within which the director alignment can still be affected by the magnetic field. The relationship for the transition layer thickness is given by:(see chapter 7, page 665 of [45], chapter 3, page 123 of [13])

$$\xi = \frac{1}{B}\sqrt{\frac{K\mu_0}{\Delta\chi}} \tag{3.2}$$

Using the values for 5CB, the magnetic coherence length ξ is estimated to be 32 μm for a magnetic field $B = 1000$ Gauss. Therefore, we designed LC cells with a gap thickness (250 μm) much greater than the coherence length (ξ).

Magnetic field alignment can also be influenced by other factors, such as the viscosity and elastic energy of the LC, both of which decrease with increasing temperature. In previous studies, reactive mesogens have been aligned in response to magnetic fields by heating the inks to high temperatures (about 100°C), close to their isotropic transition temperature T_{NI}.[41, 83]The elastic constant K depends on the order parameter S, which also decreases as the temperature increases.

In our setup, as shown in Figure 3.2, the director alignment of LCG-ink 2 can be achieved within approximately one minute at external field strengths of about 1300 Gauss at room temperature. After achieving the desired alignment, the sample is photo-polymerized to fabricate soft liquid crystalline gels (LCGs).[90] Structures were fabricated by sequential alignment and polymerization, where the magnetic field direction, and thus the director, can be independently set before each polymerization step to program 2D and 3D director profiles.

Since the LCG structures are transparent, polarization optics can be used to visualize the director alignment. Unlike polarization optical microscopy (POM), which allows for qualitative observation of the director orientation, we describe an optical characterization technique in Chapter 4 and its background in chapter 2. This method enables precise determination of the 3D director alignment. It uses a wedge cell and is based on observing the polarization and divergence of the ordinary and extraordinary light beams, which are directly related to the director alignment as it defines the optic axis of the sample.

3.6 Spatial patterning of a 2D director profile

Liquid crystalline gels with patterned director profiles were fabricated using LCG-ink 2, which has lower viscosity and requires a lower magnetic field to reorient the director in an LC cell with a gap thickness of 250 μm. Furthermore, due to the thicker cell gaps, the fabricated LCGs were self-supporting. After achieving the desired director alignment, the orientation of the molecules was fixed by UV exposure through a photomask cut from aluminum foil, which is used to set the shape of the voxel. The sample is photopolymerized at the desired position, and the voxel is printed using a 365 nm light from a UV source (UV Consulting) passing through the lens onto

the sample with an intensity of 1 W/cm^2.

Sequentially, the new director for each voxel can be set by reorienting the magnets. The unexposed regions respond to the new alignment, while the polymerized voxel director does not reorient and remains fixed. The alignment and polymerization steps are repeated, and the next voxel is printed at a new position set by physically moving the photomask. By iteratively repeating this procedure, a ribbon with alternate 45° director rotations with respect to the ribbon's long axis is printed. The POM images of the ribbon with alternating 0° and 45° director rotations can be seen in Figure 3.5.

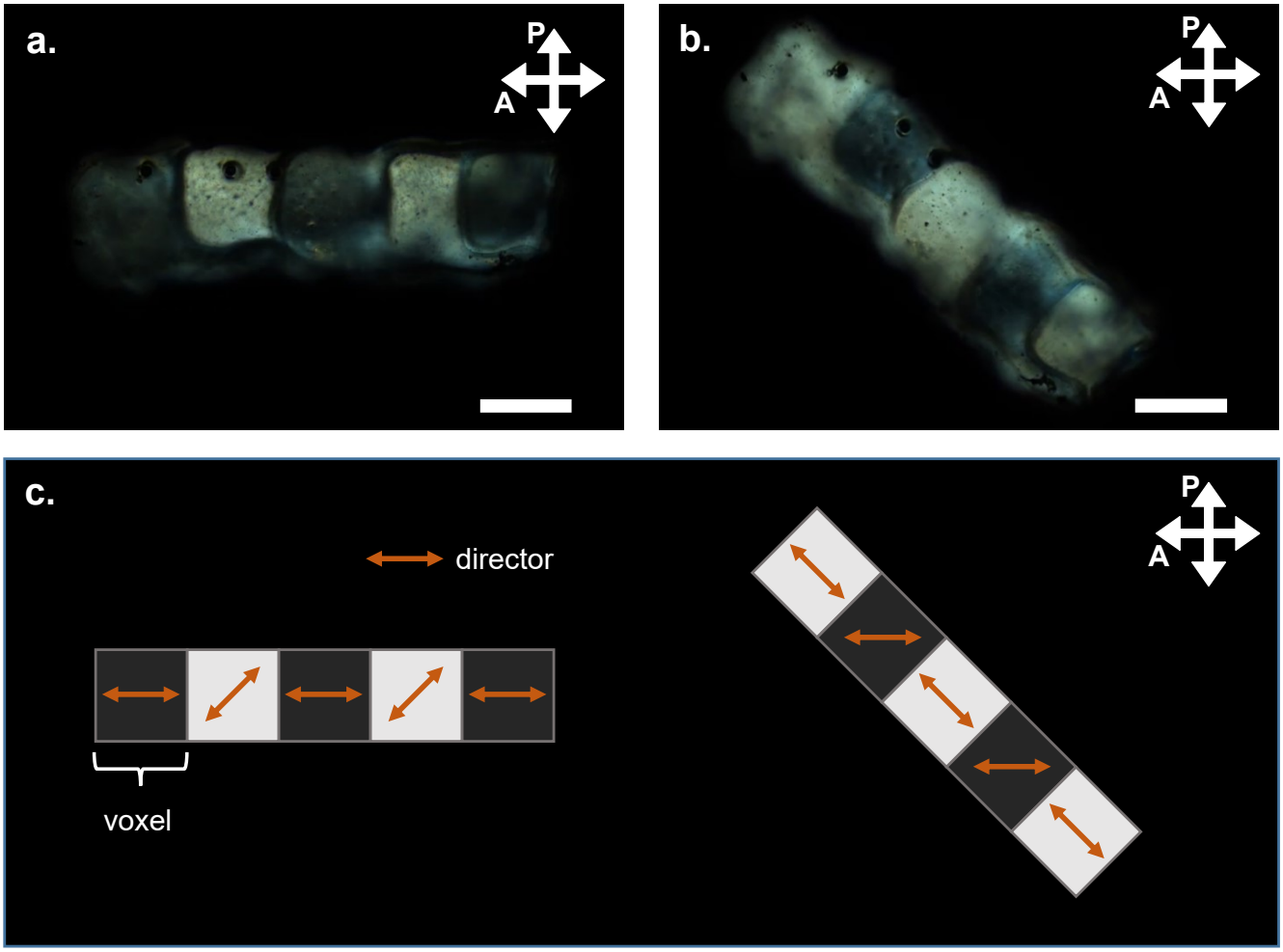

Figure 3.5: A 1D ribbon with an alternate in-plane 2D director pattern is fabricated using low magnetic field alignment and voxel polymerization iteratively. a) The long axis of the ribbon is aligned along the polarizer axes and is observed to have alternate bright and dark voxels. b) The ribbon is rotated in-plane by 45°, which reverses the brightness pattern of the voxels. c) The schematics of the fabricated 1D ribbon with alternate director alignment and its corresponding appearance under crossed polarizers. The scale bar is 200 μm. The figure and caption are adapted from [44].

It is demonstrated that the director can be patterned by aligning with smaller magnetic fields. This effect on the director alignment can be easily observed under crossed polarizers. To investigate the anisotropic deformation, the thermal actuation of a uniaxially aligned liquid crystalline

network (LCN) is tested.

3.7 Thermal actuation of uniaxially aligned liquid crystal networks (LCNs)

The LCN can be obtained by developing the LCG samples to remove the unpolymerized part of the ink. This washing step is performed by immersing the samples in isopropanol at 60°C for 2-3 minutes. After the unpolymerized part is dissolved, the samples are left at ambient temperature to dry in air. For example, after the washing and drying steps, a 0.43 mg LCG sample resulted in 0.22 mg of LCN. A negligible amount of residue remained inside the LCN samples. The LCN samples were observed under POM to analyze their mechanical deformation at high temperatures.

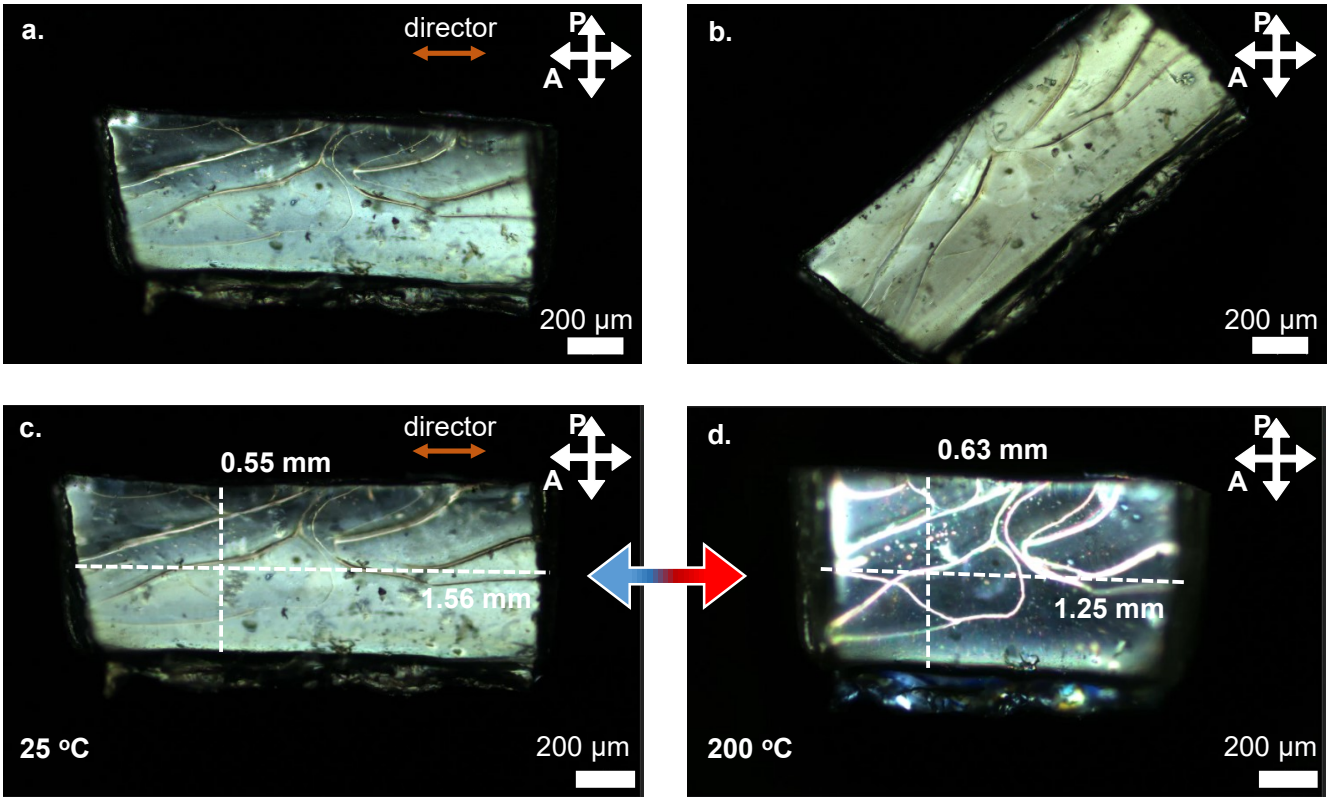

Figure 3.6: Alignment and thermal actuation of liquid crystalline network (LCN) observed under polarization optical microscope. The developed LCN is rotated and heated. a) The LCN director is parallel to the polarizers and it appears comparitively darker than b) as seen upon inplane rotation by 45° as referred to the polarizers axes. The defects and cracks are visible that appears after washing and drying steps. c,d) Thermal actuation. On heating the sample to 200°C, the film deforms by contracting approx. 20% along its long axis (director) and expanding by approx. 15% perpendicular to the director along the short axis as seen in the 2nd cycle of actuation. The figure is taken from and the caption is adapted from [44].

The actuation of LCN at high temperatures leads to anisotropic shape deformation. For this experiment, we repeated the observation, and the second cycle of actuation is shown in Figure

3.1. We measured a contraction of 20% along the director and an expansion of 15% perpendicular to the director in the plane. This deformation reached its maximum at 200°C, and the structure relaxed back to its initial shape upon cooling. The observed response can be explained by changes in the alignment of the molecules, validating the effective actuation performance of structures fabricated using low magnetic field alignment of LCG-ink 2.

3.8 LC Wollaston prism as an optical element

This method of fabrication has made the process much easier to tune the director in arbitrary orientations, facilitating the fabrication of elements for applications in optics. Here, we demonstrate an LC Wollaston prism as a small optical element made using LCG-ink 2. In this case, we used a parallel plate LC cell with a 500 μm gap thickness. A prism was then fabricated in two separate voxels, each magnetically aligned and polymerized. After fabrication, the LCG sample was carefully opened, and the substrates were removed. The block containing the two halves was cut with a shape knife, resulting in a cubic structure, with the voxel interface clearly visible along the face diagonal, as seen in Figure 3.7. The two sections have optic axes (directors) that are perpendicular to each other, and their alignment can be verified under crossed polarizers. Figure 3.8 shows the homeotropic alignment of section 1, where its contrast does not change significantly upon rotation between crossed polarizers. The director is not perfectly homeotropic, as the section does not appear completely dark. On the other hand, section 2 is in-plane aligned and shows a significant change in contrast upon rotating the prism.

Consider a y-polarized incident laser beam entering the prism, as shown in Figure 3.7c. At the first interface, the light encounters the ordinary refractive index n_o, as the E-vector is orthogonal to the optic axis. According to Snell's law, the light bends towards the normal because it experiences a higher refractive index n_e in the second half of the prism.[80] On the other hand, a z-polarized beam encounters the higher refractive index n_e in the first section and refracts away from the normal in the second section, where it experiences a lower refractive index n_o. This LCG Wollaston prism was used to observe the beam divergence, as shown in Figure 3.7c, demonstrating its use for optical applications without removing or washing the non-reactive part of the ink. This method is highly useful for fabricating new, unusual, or small components in polarization optics or any element with a shaped structure that cannot be easily fabricated using other techniques.

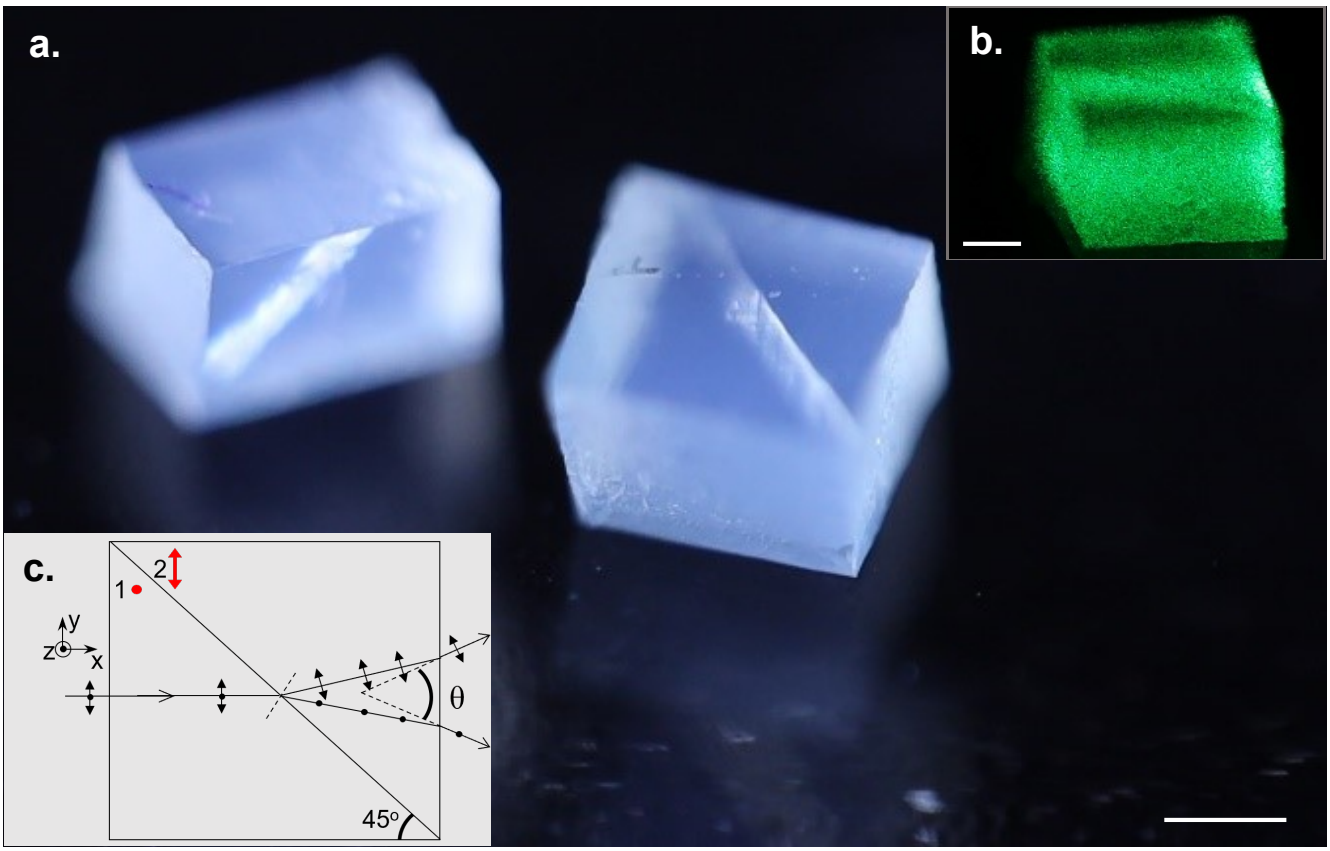

Figure 3.7: The LCG Wollaston prism fabricated using magnetic field alignment: a) 3D image of the prisms, with their interfaces clearly visible. b) Demonstration of the LCG Wollaston prism as an optical component for beam splitting. c) Schematics (not to scale) depicting the optic axes of the sections and the beam refractions for the two orthogonal polarization states. Section 1 has the optical axis (director) along the z-axis, and Section 2 has the optical axis along the y-axis. The y-polarized beam experiences the ordinary refractive index in Section 1 and the extraordinary refractive index in Section 2, resulting in refraction towards the normal at the interface. The z-polarized beam encounters the ordinary refractive index in Section 1 and the extraordinary refractive index in Section 2, refracting away from the normal at the interface. The figure and caption are adapted from [44].

3.9 Limitations

As in any LC alignment process, the magnetic field alignment process presented here also has some general limitations. The alignment is always influenced by the surface anchoring effects at the boundaries of each voxel. A drastic or sudden change in the alignment from one voxel to another involves an energy cost; hence, the minimum size of the voxel in 3D alignment is limited by the magnetic coherence length (here $\xi = 32$ μm). With the dimensions of the printed voxels much larger than the coherence length, the surface anchoring effects from neighboring voxels decay exponentially, and the resulting director reorientation is primarily influenced by the external magnetic fields rather than interactions from adjacent voxels.[13]

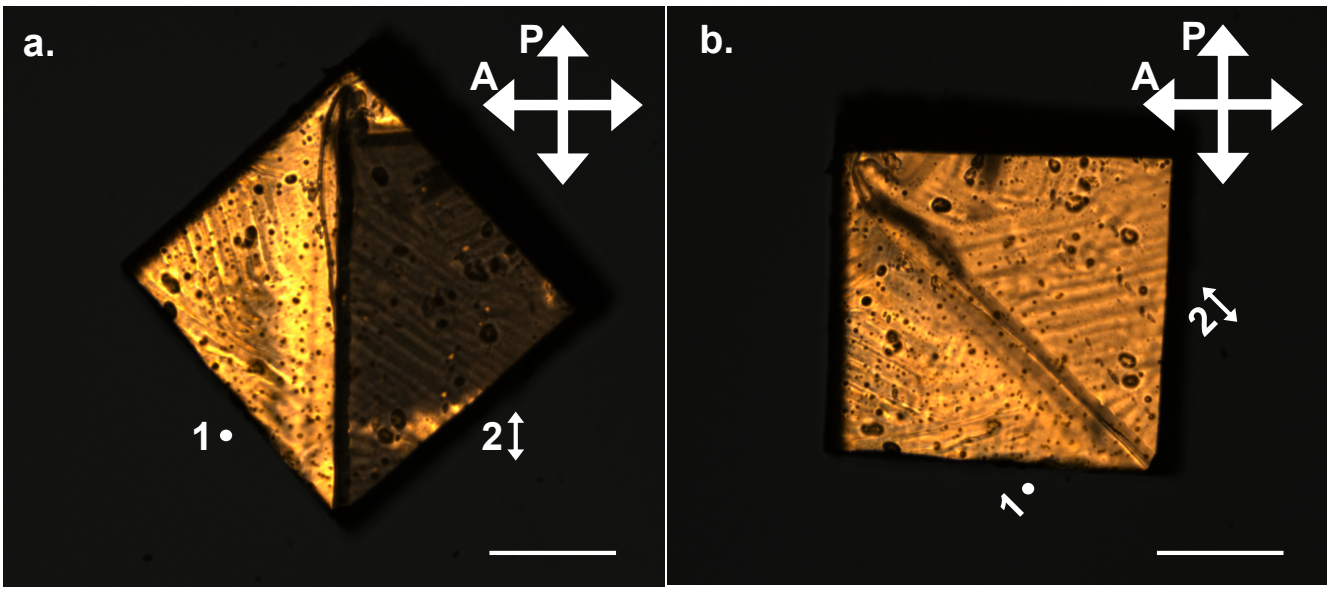

Figure 3.8: POM images of the LCG Wollaston prism fabricated with orthogonal directors in two sections and their corresponding contrast, as seen in (a) and (b), upon rotation at 0° and 45° relative to the polarizers. The director is homeotropic in section 1 and in-plane aligned in section 2. Scale bars are 3 mm. The figure and caption are adapted from [44].

3.10 Conclusions

We have demonstrated that adding 5CB to the LC ink formulation lowers the threshold of the magnetic field required for 3D magnetic field alignment of LC molecules at room temperature, enabling the fabrication of cross-linked LC polymers (CLCPs). LCG-ink 2, containing the non-reactive mesogens 5CB and E7, aligns with a 0.13 T field at room temperature, and liquid crystalline gels (LCGs) are successfully fabricated. Thicker LC cells (250 μm) are used to minimize surface anchoring effects and maximize alignment due to external fields. The actuation of a 2D uniaxially aligned LC network film is measured to verify the alignment. An LC ribbon with a spatially patterned 2D director profile is fabricated and observed under crossed polarizers. The director can also be aligned in arbitrary 3D orientations to create optical elements such as an LC Wollaston prism for beam splitting applications.

We believe this method will facilitate the fabrication of LC actuators at room temperature with complex 3D spatially varying director profiles. Future work can be done to develop inks without non-reactive mesogens that can be aligned using low magnetic fields at room temperature, which would allow for more complete polymerization and enhanced structural integrity. Additionally, incorporating magnetic particles as inclusions in the LC ink, which can locally interact with mesogens to induce global director alignment, should also be explored. This could further reduce the magnetic field threshold below that of 5CB. However, a challenge remains in preventing the

aggregation of magnetic particles, which could introduce defects in the bulk LC. Cross-linked LC polymers (CLCPs) with 3D spatially varying director profiles promise complex mechanical actuation, as full 3D director programming can be patterned into structures in ways that are not easily achieved with other alignment techniques.

4 3D director characterization using a wedge cell

4.1 Introduction

3D director alignment in LC structures has become increasingly popular due to the higher degree of control it offers in patterning spatially varying profiles, enabling complex mechanical actuation and optical elements that push the limits of LC applications.[41, 57, 87, 91] Field alignment techniques have proven useful in achieving this goal, and it is crucial to develop a method for observing and verifying the 3D director alignment to facilitate the fabrication of complex actuators.[41, 42, 58, 91] Characterizing 3D alignment is very challenging with traditional techniques such as WAXS/SAXS measurements.[92, 93] The Polarization Optical Microscope (POM) permits the visualization of the director projected onto the imaging plane, meaning only the 2D projection of the 3D director orientation is observed. Consequently, it becomes difficult to analyze the out-of-plane component of the director in a birefringent sample, and therefore, POM cannot be directly useful. Although the LC-PolScope can be used with POM to measure 3D molecular orientation, it requires a setup to sequentially illuminate circular- and elliptically-polarized light in various directions to observe the director and its 2D projected effective optical path difference simultaneously, which is then used to calculate the out-of-plane angle of the optic axis (director).[94] Hence, a simpler and faster method is required to visualize 3D director orientation in real-time to effectively use 3D alignment techniques and realize the complex functionalities of LC polymers.

Here, we demonstrate a fast and simple optical characterization technique that enables the real-time observation of 3D director alignment in LC structures. This method is based on the splitting of a light beam into two orthogonal components: the ordinary ray (O-ray) and the extraordinary ray (E-ray).[95–97] Their splitting depends on the orientation of the optic axis (and hence the director alignment) as the light passes through the LC cell. The O-ray has its electric field polarized orthogonal to the plane of the director and the propagation direction, while the

E-ray has its electric field polarized in the plane of the director and propagation direction. The polarization and splitting of these rays serve as a measure for both in-plane and out-of-plane alignment, facilitating the real-time visualization of any dynamic changes in the LC director orientation.

4.2 Motivation

To characterize the 3D director alignment in thick LC samples and help precisely align the global director in arbitrary 3D orientations, the aim is to visualize in real-time the dynamic changes in 3D director alignment. This will facilitate the fabrication of complex actuators and optical elements, which are very challenging to achieve with other techniques. The goal is to monitor the 3D director alignment to support the development of LC structures with spatially varying director profiles.

4.3 Results

The work presented in this chapter has already been published in [44] and is in part reproduced in this chapter. I would like to thank Prof. Dr. Frank Gießelmann (University of Stuttgart) for the collaboration, for providing access to his microscopy lab facilities, and for valuable discussions; Dr. Carlos Sánchez-Somolinos (CSIC, Zaragoza) for his collaboration, for providing LC inks for this study, and insightful discussions; Prof. Dr. Eva Blasco (IMSEAM, Heidelberg) for providing samples and helpful discussions, Prof. Dr. Christine Selhuber-Unkel for providing lab facilities, and Dr. Alexander Song for his assistance in developing the optics setup.

4.4 Wedge cell technique

The aligned director in a nematic LC sample can be considered as its optic axis direction. When a laser beam enters the birefringent LC sample, it splits into two orthogonal polarization component beams: the ordinary ray (O-ray) and the extraordinary ray (E-ray). When the incident beam is normal to the director (optic axis), the O-ray has its electric polarization perpendicular to the director, while the E-ray has its electric field aligned with the director direction.[95–97]

The O-ray and E-ray encounter different refractive indices, denoted as n_o and n_e, respectively. For the case where the beam propagates at an angle θ with respect to the director (optic axis), the E-ray experiences an effective extraordinary refractive index (n_{eff}) that depends on θ, n_o, and

n_e, given by the relation 2.59 as described in chapter 2: [81, 95, 96]

$$n_{\text{eff}}^2(\theta) = \frac{n_e^2 n_o^2}{n_o^2 \sin^2\theta + n_e^2 \cos^2\theta} \tag{4.1}$$

Hence, the propagation of the E-ray is dependent on n_{eff} and can be determined using the wedge angle and Snell's law. The E-ray encounters n_{eff} as an effective refractive index, and its value is bounded as $n_e \geq n_{\text{eff}} \geq n_o$. According to Snell's law, when light enters an LC medium at an angle θ relative to the director (optic axis), the O-ray and E-ray, due to their different refractive indices, propagate in different directions. This effective birefringence leads to the splitting of the O-ray and E-ray, and one can use this splitting to measure the out-of-plane angle of the optic axis (hence the director) from the sample plane.

For the case where the light beam is incident on a parallel-plate sandwiched LC cell, the O-ray and E-ray components travel in different directions within the medium. In this configuration, the O-ray propagates in the same direction as the incident beam, normal to the LC medium, but the E-ray bends by about 0° to 6° relative to the O-ray depending on the optic axis direction.[96] As both beams traverse the entire cell and exit from the opposite face, they propagate with a slight displacement. Both components propagate parallel after exiting, and hence their displacement remains constant.

This displacement in thin LC cells is hard to observe because the beam separation depends on the thickness of cell and typically lies between 0 and 25 μm, which, compared to the beam's diameter of 500 μm, is very small and not easily visible on a camera. Hence, the parallel-plate cell configuration is not useful for this case. A wedge cell provides divergence of the orthogonal beams as they exit the cell. The use of a wedge cell has already been introduced in previous studies to determine the refractive indices of LCs.[45, 98] Here, we demonstrate that it can also be used to measure the 3D director alignment.

For a wedge cell containing nematic LC, when a polarized beam is incident normally on the optical face, it splits into two orthogonal components. Their polarization states and separation depend on the optic axis orientation.[95–97] Figure 4.1 shows the schematic (not to scale) of the wedge cell with the director parallel to its first face and perpendicular to the beam propagation. It is assumed that the sample is well-aligned, and the director is uniformly oriented throughout the bulk sample. At the interface, the beam follows Snell's law and the wedge angle causes the E-ray and O-ray to split into two components, due to their different refractive indices, n_e and n_o, respectively.[79]

In our experiments, we prepared a wedge cell using 0.7 mm thick glass substrates of approxi-

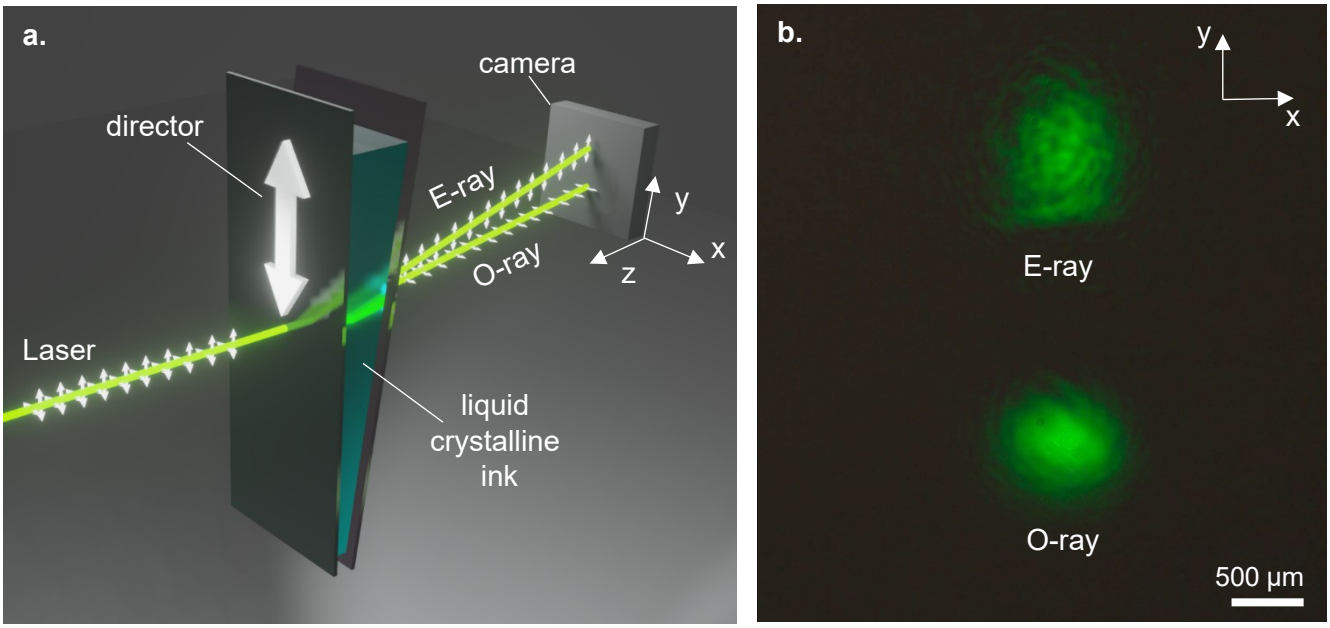

Figure 4.1: Wedge cell to observe the 3D alignment of the LC director. a) The laser is incident perpendicular to the surface of the wedge cell. The E-vectors are represented by the double-headed white arrows to depict the polarization state of the light beam and the plane of the electric field. At the exit face of the wedge cell, the beam splits into two orthogonal components: the extraordinary ray (E-ray) and the ordinary ray (O-ray). The E-ray has its E-vector polarized in the plane defined by the director and the propagation direction. The O-ray is polarized with its E-vector perpendicular to it. One possible example of director alignment is indicated by the white double-headed arrow. The beam divergence depends on the director alignment and the wedge angle. b) The split ray spots are observed by a camera placed 8.3 cm away from the exit window of the cell. The figure is taken from and caption is adapted from [44].

mately 1.5 cm × 1 cm in size. These glass surfaces were assembled into cells with the help of two different spacers (250 μm and 1 mm thickness) placed at opposite ends. The spacers were adhered to one glass substrate, and the other substrate was then attached to form a sandwiched wedge cell. The wedge angle δ was determined by measuring the separation of the spacers and the dimensions of the glass substrates. This angle δ showed slight variations and was measured to be between 7° and 9° across all cells. The LC sample was filled into the cells dropwise using capillary action.

The 532 nm laser (0.4 μW) is used in our optical characterization method. The split E-ray and O-ray were observed through a CCD camera mounted 8.3 cm away from the back window of the cell in the path of the beams. The schematic of the measurement setup is shown in Figure 4.2.

When the beam is incident normally on the first air-glass-LC interface, it continues along the same path, perpendicular to the face. Upon reaching the second LC-glass-air interface, the angle of incidence matches the wedge cell angle, resulting in the beam splitting into two components due to their different refractive indices, following Snell's law. The rays propagate with a divergence angle α, which depends on the optic axis orientation within the cell and the birefringence of the sample. This divergence angle leads to significant separation at the plane of the camera screen,

allowing the two components to be clearly distinguished.

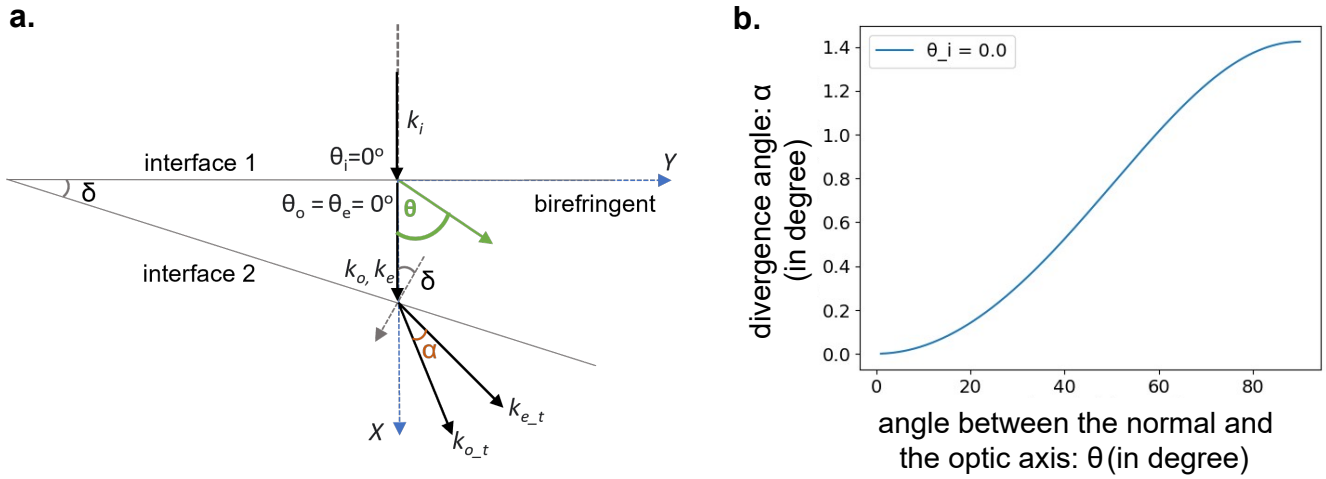

Figure 4.2: a) The schematic (not to scale) indicating the refraction of the normally incident light beam on one face and exiting with splitting into E-ray and O-ray, with divergence, from the other face of the wedge cell. Inside the birefringent medium, both orthogonal components travel in the same direction normal to interface 1. As shown, the angle θ is defined as the angle between the arbitrarily aligned 3D director (optic axis) and the normal to interface 1. b) Plot of the relationship between the divergence angle α and the out-of-plane angle of the optic axis θ for the case of a wedge cell with an angle $\delta = 7°$. The figure is taken from and the caption is adapted from [44].

To calculate the divergence angle of the beams, the angle of refraction θ_e at the first interface (Interface 1) needs to be estimated. Considering the fixed incident angle to be θ_i, the refraction angle varies with the direction cosines of the director (optic axis), as derived in the introduction section. For our experiments, we simplified this observation by directing the laser beam normal to Interface 1 ($\theta_i = 0°$), so that both the E-ray and O-ray have refraction angles $\theta_o = \theta_e = 0°$, as shown in the schematic diagram in Figure 4.2a.

Since both beams travel in the same direction inside the LC sample, the splitting appears only at Interface 2. Here, the incident angle is δ, and following Snell's law, both beams exit the cell and propagate with a divergence angle α. This divergence angle depends on the effective refractive index n_{eff} for the extraordinary component, which is further dependent on the director alignment θ. An example plot is shown in Figure 4.2b for the case of a wedge cell with $\delta = 7°$, using the typical refractive indices for 5CB: $n_o = 1.5$ and $n_e = 1.7$.

The divergence angle is calculated for the angle θ between the optic axis and the normal direction to Interface 1. Hence, the divergence angle can serve as a tool to measure the optic axis orientation and, consequently, the director alignment.

The schematic Figure 4.3 depicts how the in-plane and out-of-plane orientations were analyzed. We tilted the entrance face (Interface 1) to allow the laser beam to enter the LC cell normally. The camera screen was positioned at a distance D away from the back face of the wedge cell. The

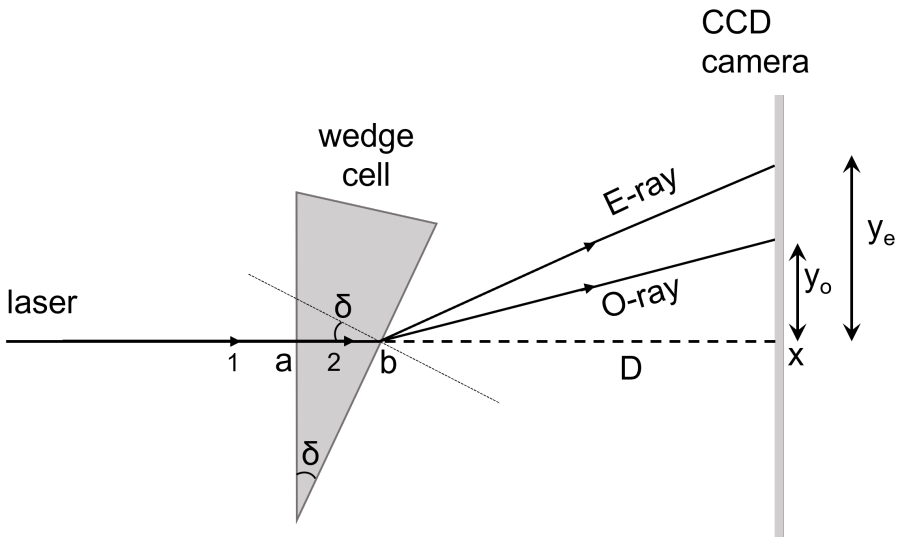

Figure 4.3: The schematic of the beam divergence measurements for a laser beam incident on the wedge cell at point a and traveling without refraction to point b on the other face is shown. At the exit window, the splitting appears as both beams refract at different angles, following Snell's law and the wedge angle δ. Their splitting is observed on the camera detector through the measurement of distances y_e and y_o from the reference point x. The figure is taken from and the caption is adapted from [44].

center spots of the E-ray and O-ray beams (y_o and y_e) relative to the incident beam spot were observed on the camera screen placed at the distance D. The distances were measured relative to the point where the incident laser beam would have been measured in the absence of the wedge cell in the beam path.

4.5 Analysis of in-plane director orientation

To analyze the 2D director orientation, polarization optics can be used. For the case of linearly polarized incident light, the in-plane director projection onto the image plane can be observed. By rotating the polarization of the incident light, the relative intensities of the E-ray and O-ray can be altered, as seen through the CCD camera. Figure 4.4 panels indicate the separation distance d between the rays.

It can be observed that when the polarization of the incident light lies in the same plane defined by the director and the propagation direction, only the E-ray is visible on the camera. As expected, if the polarization direction is further rotated by 90°, only the O-ray component is visible on the camera. Additionally, an analyzer can be introduced in the beam path between the cell and the screen. Upon rotating the analyzer's optic axis to align with the plane of the director and propagation direction, only the E-ray component is visible while the O-ray is blocked. This optic axis direction corresponds to the 2D projection of the 3D director alignment, and this

technique can be used to determine the in-plane director orientation.

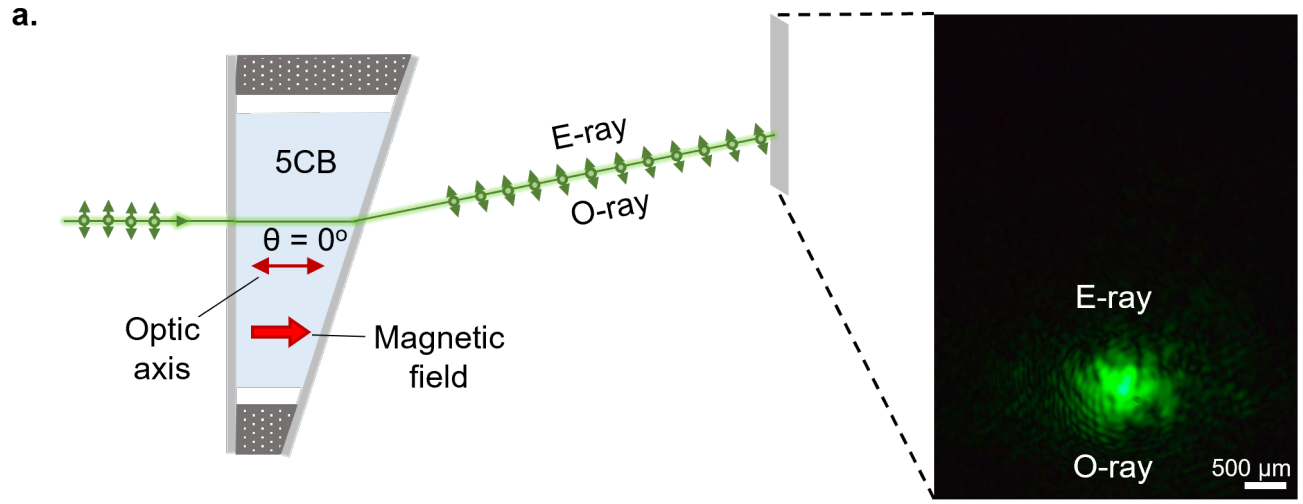
a.
5CB
θ = 0°
Optic axis
Magnetic field
E-ray
O-ray
E-ray
O-ray
500 μm

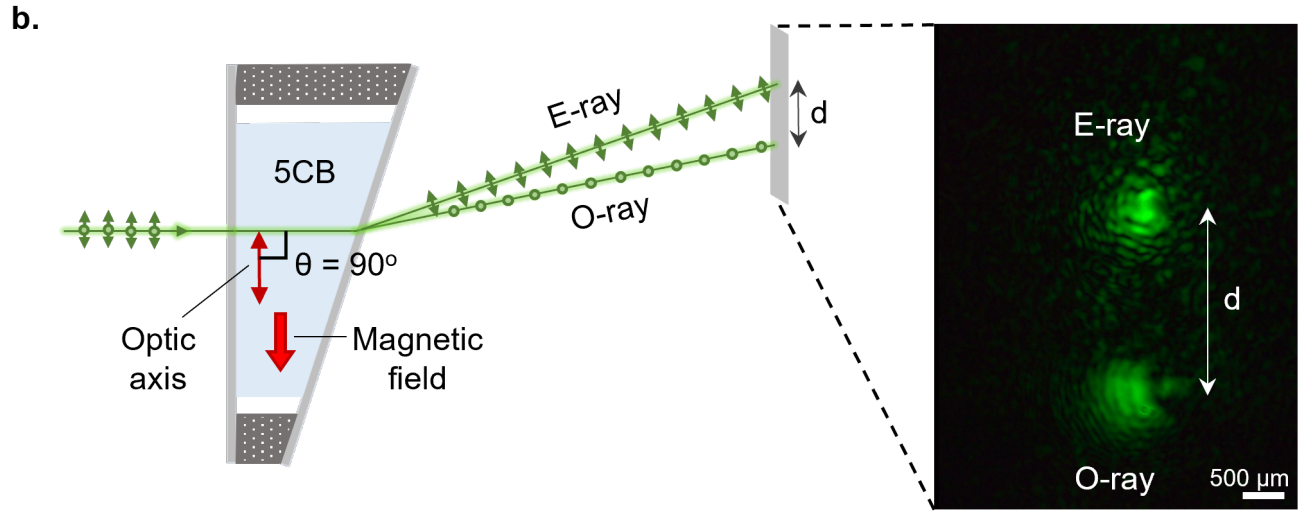
b.
5CB
θ = 90°
Optic axis
Magnetic field
E-ray
O-ray
d
E-ray
d
O-ray
500 μm

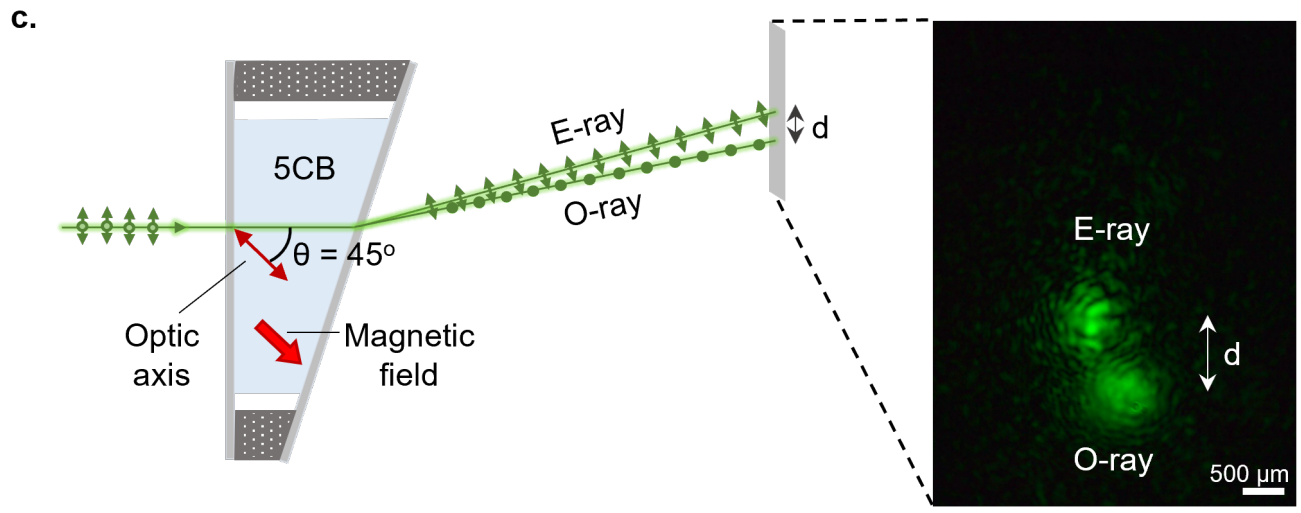
c.
5CB
θ = 45°
Optic axis
Magnetic field
E-ray
O-ray
d
E-ray
d
O-ray
500 μm

Figure 4.4: The splitting of E-ray and O-ray from the angle window of the wedge cell is observed in the camera as a function of the director's out-of-plane orientation. Three different cases of angle θ are demonstrated to study its effect on the splitting observed on the camera detector. The director is aligned using magnetic fields and can also be considered as the optic axis of the birefringent material 5CB. a) Case: $\theta = 0°$. There is no splitting observed as both the beams seem to overlap on the detector plane. This is due to the fact that the beams do not experience any effective birefringence and hence follow the same propagation path. b) Case: $\theta = 90°$. The director is aligned perpendicular to the incident light, and hence the beam experiences maximum effective birefringence. Therefore, the E-ray and O-ray follow different propagation paths after exiting the window, depending on the refractive indices n_e and n_o for the extraordinary and ordinary rays, respectively. Hence, we see maximum separation between the split beams. c) Case: $\theta = 45°$. The E-ray experiences an effective refractive index $n_{\text{eff}} < n_e$ and hence, due to decreased effective birefringence, the splitting of orthogonal beams as seen on the camera decreases. Hence, the observed splitting increases as the out-of-plane angle θ is increased from 0° to 45° to 90°. The figure is taken from and the caption is adapted from [44].

4.6 Analysis of out-of-plane director orientation

To analyze the 3D director orientation, the out-of-plane angle is determined. This angle affects the separation of the two rays, depending on other factors such as the angle of incidence, the wedge angle, and the orientation of the director. The first two are experimental parameters, and hence can be used to determine the out-of-plane alignment and, consequently, the 3D director orientation.

The experimental observations for different out-of-plane angles can be seen in Figure 4.4. When the director is aligned out of the plane with $\theta = 0°$, there is no separation between the E-ray and O-ray. For the case when the director is aligned in the plane of the cell ($\theta = 90°$), as guided by magnetic fields, the separation between the E-ray and O-ray is maximum. Upon rotating the field to 45° out-of-plane, the separation decreases, and the dynamics of the motion of the laser spot on the camera can be understood as real-time director visualization.

4.7 Protocol to determine the 3D director orientation

As seen in Sections 2.5.3 and 2.5.4, the relationship between the splitting (divergence) angle and the director (optic axis) orientation, as well as the incidence angle, is complex. However, the protocol can be simplified by choosing the incidence angle $\theta = 0°$, where the light is incident perpendicular to one face of the wedge cell, as indicated in Figures 4.2 and 4.3.

Following symbols are used to describe different parameters as shown in Figure 4.2

- φ (in-plane director orientation of LC)
- θ (out-of-plane director orientation of LC)
- δ (wedge angle of the LC wedge cell)
- θ_i (angle of incidence of laser beam at interface 1)
- θ_o and θ_e (angle of refraction of O-wave and E-wave at interface 1)
- θ_{o_2} and θ_{e_2} (angle of incidence of O-wave and E-wave at interface 2)
- θ_{o_t} and θ_{e_t} (angle of refraction of O-wave and E-wave at interface 2)
- α (angle of divergence)

In the following, I describe a procedure that will be used for the real-time visualization of the 3D LC director to optimize the magnetic field alignment for the results shown in chapter 3. One can use the following protocol to determine the angle of the optic axis (director in LC):

1. Prepare a wedge cell and fill it with LC. With the laser light incident normal to one surface of the wedge cell, the splitting should be visible as the light beam traverses the whole cell and exits from the opposite face, as shown in Figure 4.3.

2. The split component that has a larger deviation from the incident path is the extraordinary ray (E-ray). Insert the analyser on the path of the E-ray. Upon rotating the optic axis of the analyser, the intensity of the E-ray reaching the camera will change.

3. **In-plane angle φ:** Set the angle of the optic axis of the analyser such that its axis is perpendicular to the electric field of the E-ray and hence blocks the E-ray. Then the in-plane angle φ of the director is perpendicular to the angle of the analyser's optic axis.

4. Divergence angle: measure the angle of splitting between E-ray and O-ray by the known parameters: i) Camera and cell separation distance, ii) Distance of separation of the orthogonal beam spots on the camera detector.

5. **Out-of-plane angle θ:** Using the known parameters: i) Divergence angle α, ii) Wedge angle δ, iii) Principal refractive indices of the medium, n_o and n_e, make a graphical representation and plot of divergence angle as a function of optic axis orientation in Y-X plane as shown in Figure 4.2.

6. Estimate the angle θ for observed divergence α from the plot.

   Steps to plot the graph of divergence v/s out-of-plane angle θ

7. Apply Snell's law at both interfaces: **Interface 1:** Incident light is normal to the surface with $\theta_i = 0°$ leading to the propagation directions of both E-wave and O-wave in the same direction with $\theta_o = \theta_e = 0°$, valid for all values of director angle θ. **Interface 2:** The angle of incidence for both polarization state components are $\theta_{o_2} = \theta_{e_2} = \delta$ and applying Snell's law on these as:

$$n_{\text{eff}} \sin\delta = n_i \sin\theta_{e_t} \tag{4.2}$$

$$n_o \sin\delta = n_i \sin\theta_{o_t} \tag{4.3}$$

8. Using the known values of n_i, n_o, n_e, δ, our set condition in this procedure $\theta_o = \theta_e = 0°$. Hence the dirctor orientation with respect to E-wave can be considered as $\theta_{kp} = \theta - 0° = \theta$

9. The divergence angle can be calculated, as described by relation 2.66 in chapter 2:

$$\sin\theta_{e_t} = \frac{n_o n_e}{\sqrt{n_o^2 \sin^2\theta + n_e^2 \cos^2\theta}} sin\delta \tag{4.4}$$

$$\sin\theta_{o_t} = n_o \sin\delta \tag{4.5}$$

10. The divergence angle α can be calculated as:

$$\alpha = \theta_{e_t} - \theta_{o_t} \tag{4.6}$$

4.8 Splitting observations for various 3D director orientations

This work demonstrates the use of the wedge cell technique to determine the arbitrary 3D director orientation described by Euler angles. For this experiment, we polymerized samples in seven wedge cells, each having a different 3D alignment, using the LCG ink aligned with low magnetic fields as described in Chapter 2. The schematics of the director alignment in each cell can be seen in Figure 4.5. To achieve seven different orientations, the magnetic field was aligned to combinations of Euler angles with in-plane angles φ: 0°, 45°, and 90°, as well as out-of-plane angles θ: 0°, 45°, and 90°.

To characterize the alignment, the angle φ can be measured by rotating the linear polarization of the incident light, which corresponds to the polarization direction of the incident light when the ordinary component completely vanishes. To analyze the out-of-plane angles, the divergence or the splitting between the rays is measured. As expected, the divergence or separation depends only on the angle θ and is maximum when $\theta = 0°$, independent of the φ angles. For $\theta = 45°$ and any φ angles, the separation decreases, and our observations match well with theoretical expectations, as shown in Figure 4.5c.

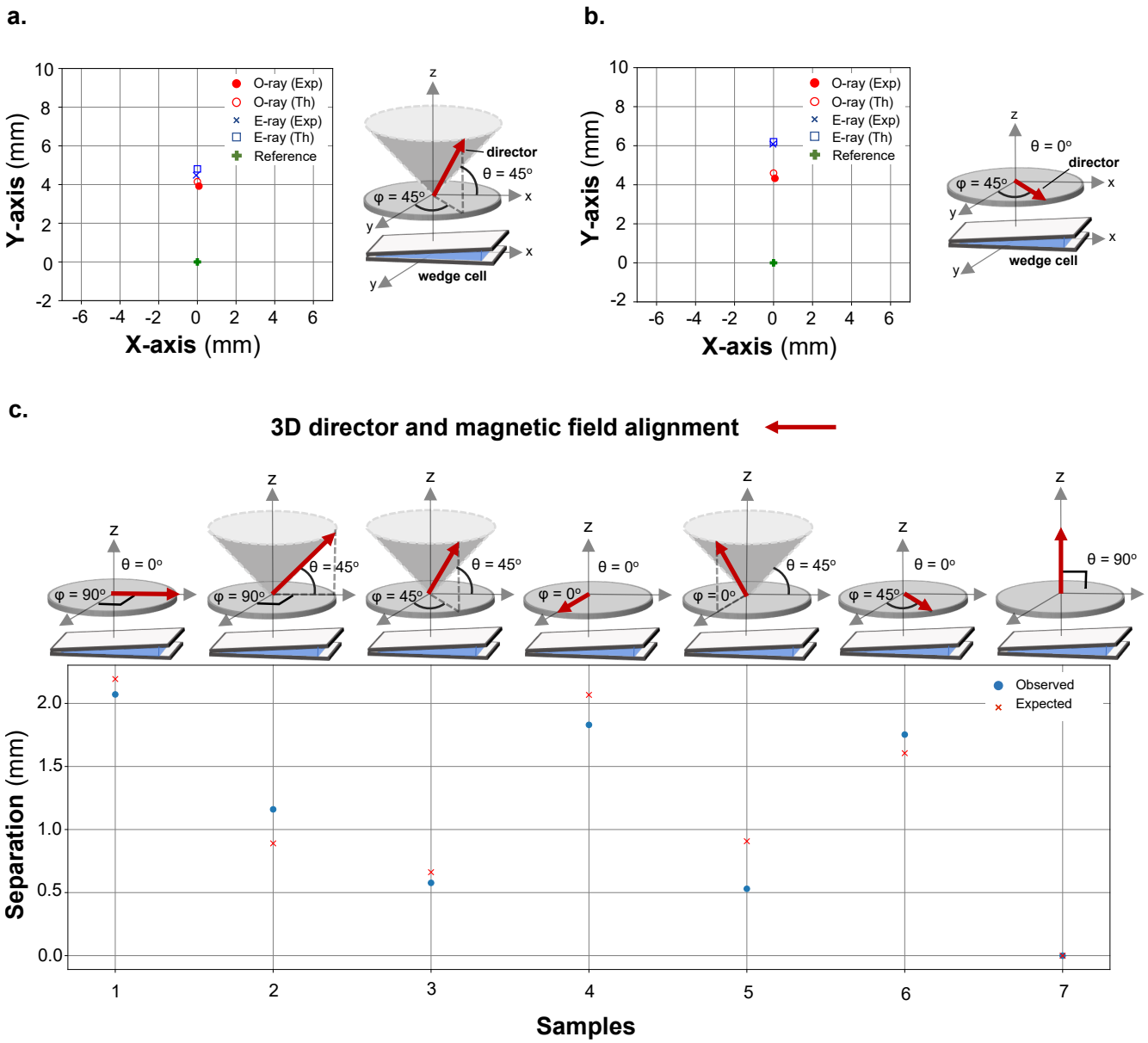

Figure 4.5: Observed E-ray and O-ray splittings for seven different 3D aligned configurations in different wedge cells and results are compared with theoretical estimates. The director Euler angles θ and φ are varied using magnetic field alignment. This experiment indicates the reliability of the characterization method. The red arrow depicts the direction of the magnetic field, the director, and the optic axis all in the same direction. The experimental observations and theoretical predictions match very well for different cases of θ and φ. a) For $\theta = 45°$ and $\varphi = 45°$, the beams have smaller separation due to lower effective birefringence seen in the sample, as compared to b) $\theta = 90°$ and $\varphi = 45°$, which show the dependence of the out-of-plane angle θ on the beam divergence and hence the observed splitting. c) The summarized splitting between E-ray and O-ray is primarily dependent on angle θ and independent of angle φ. The small difference between the samples with the same angle θ is due to the difference in their wedge angles δ of the corresponding cell. For samples 1, 4, and 6, the observed splitting is larger due to larger effective birefringence seen by light beams, as compared to samples 2, 3, and 5, resulting in their smaller splitting distance. The angle θ can be related to the 3D director (optic axis) orientation. The figure is taken from and the caption is adapted from [44].

Additionally, the dynamics of the reorientation in response to an external field can also be realized using this method. This real-time visualization provides information on how fast the alignment response saturates and whether the alignment is effective with the given field strengths. This experimental observation can be used to optimize the alignment response of any ink formulation with any alignment technique to obtain the desired response for a particular application. For instance, the LCG films prepared for the characterization experiment have 3D alignment and can exhibit complex actuation due to their 3D director profile. We have not studied the thermal actuation of these films because the films were too sticky and hence difficult to handle after polymerization. However, the literature suggests that these films would not only contract/expand in-plane but would also exhibit complex mechanical deformation, where the angle of deformation depends on the director orientation in 3D.[87]

Our characterization technique using a wedge cell involves the observation of the splitting angle between the E-ray and O-ray, which depends on the out-of-plane director angle θ that was varied between 0° and 90° in a cell with a wedge angle $\delta \approx 7°$. The splitting was recorded by a CCD camera placed 8.3 cm away from the cell. This method has the potential to provide details about the dynamics of the alignment that can be utilized for effective alignment optimization.

The limitations of our proposed characterization technique are that while this method enables the observation of surface effects on the alignment response to an external field and provides real-time visualization, it requires the use of wedge cells. This puts a constraint on the experiments, as a wedge cell might not be practical for many applications compared to a parallel sandwiched cell. Hence, the idea would be to first optimize the ink formulation and other parameters such as surface anchoring, field strengths, cell gaps, temperatures, and alignment response time using a wedge cell. Then, based on this optimization, these same parameters can be used for alignment and fabrication in any other desired cell configuration. This characterization technique is very general and can be used for other LC inks, surface coatings, alignment techniques, and would be useful to diagnose the quality, uniformity, and limitations of the alignment setup. Once these observations are taken, the same parameters and information can be used to fabricate complex 3D spatially varying director patterns in LC structures.

4.9 Conclusions

We have demonstrated an optical characterization technique to visualize the 3D director profile in real time and diagnose the quality of alignment in a wedge cell, which cannot be determined by using only Polarization Optical Microscopy (POM). The method is based on the observation

of the splitting of a light beam into E-ray and O-ray components after the light traverses through an LC wedge cell. The in-plane and out-of-plane angles were analyzed using polarization optics and beam splitting due to the wedge cell. We have verified the 3D alignment in seven different cells, each having the director in seven different 3D orientations, using our proposed method. This technique has the potential to facilitate the effective fabrication of complex 3D director profiles to achieve complex mechanical actuation.

Future work can focus on observing this effect for even weaker fields. A weak value amplification scheme might be very helpful in the case of weak effects and small divergence angles, as it can potentially amplify the splitting between orthogonal components. This amplification method carefully chooses a post-selection for the final light beam polarization and has already yielded successful results in optically active systems to detect nanorad divergence angles.[99, 100] This could further increase the sensitivity of our wedge cell characterization technique and enable the characterization of samples with smaller birefringence, lower than that of 5CB.

5 Holographic printing of 3D liquid crystal actuators

5.1 Introduction

The liquid crystalline polymers with 3D shape and 3D director alignment are promising material systems as they exhibit 3D complex mechanical actuation based on their geometry as well as their programmed director profile.[30, 44, 46–50] The 3D capability in both shape and molecular orientation is necessary to unlock the three spatial degrees of freedom for actuation.[37, 38, 40, 43, 51] The traditional fabrication techniques are being used to fabricate 3D structures but the limitations lie in the free design of the structures to avoid any geometrical and alignment constraints.[44, 48–50] This requires that the body geometry and molecular alignment are independently controlled. In literature, 3D/4D fabrication of LC actuators mainly involves very well-developed techniques such as direct laser writing (DIW), digital light processing (DLP) and two-photon laser writing (TPLP).[37–43, 52, 57–60, 101] as has been discussed in section 2.4. But, the challenge has not been completely addressed. For example, the DIW method has a nozzle printer that extrudes the ink and aligns the director along the printing direction. The shape and alignment are both set by printing paths as seen in the case of printed swimmers, adaptive optical elements, folding structures or grippers.[37–40, 52] This method limits the director to be defined only along the printing direction and in addition, also creates director distortions in between the interface of two paths. The advancement has been made to print 3D freeform structures in the gel matrix,[53] but the director is still coupled to the printing direction which is hard to avoid in the case of extrusion printing.

The independent director programming, irrespective of body structure, can be achieved with the DLP technique as described earlier in the section 2.4. The literature shows that high field strengths or special responsive inks incorporating non-reactive mesogens are required to align the director in 3D in layer by layer or voxel by voxel printing steps.[41, 57, 58] However, high director

distortion is seen at the interfaces. Many fabrication examples have been reported in the literature such as 4D emulsions and 4D multi-responsive structures.[55, 56] But this technique can only be used to fabricate complex structures in voxel by voxel and layer by layer steps which makes the process slow and also prone to distortions at the interfaces.

In microscale fabrication, 2PLP is the most promising technique to print 4D LC polymers.[42, 43, 59, 60, 101] This technique has been described earlier in the section 2.4. The 3D director can be independently aligned either using quasi-static electric fields or 3D-printed polydimethylsiloxane-based confinement barriers.[42, 43, 59] These examples show great potential in printing 4D complex structure but has a core limitation that the printing need to be done in the scanning mode.

Here, we show the next technical advancement that enables the parallel printing of whole 3D structure to overcome the challenges of layer by layer and scanning printing. The benefits of parallel printing is that it initiates the polymerization of the whole 3D object at the speed of light in a single short exposure time where the director alignment is kept independent to the 3D geometry of the structure, under room temperature and without the use of low molecular weight mesogens. The 3D objects can be printed without using any mechanical moving stages or lasers but directly through the 3D spatially modulated light in a single exposure time. The laser is spatially modulated using non-convex optimized 3D computer-generated holograms to shape the light in 3D space.[102] This optimization technique has already been used in the literature and in this study, we are using this light modulation to print 3D shapes directly inside the printing LC cells. The 3D printing then happens following the non-linear response of the photopolymerization to the light intensity.[103] This study demonstrates the fabrication of various complex 3D LC actuators using holographic projection of 3D light intensity patterns that enables the parallel printing of whole 3D structure with independently programmed 3D director profile, in a single short exposure time.

5.2 Motivation

The study shows the parallel fabrication of whole 3D LC structures with arbitrary 3D director alignment in a single short exposure time. The light is spatially modulated to shape into 3D complex intensity patterns that enable the direct printing of 3D geometries in the LC cell while avoiding interface effects observed in sequential printing. The goal is to fabricate complex 4D LC actuators and realize all three spatial degrees of freedom, allowing the printing of complex geometries that are otherwise difficult to realize for advanced actuation mechanisms.

5.3 Contributions

The study has been performed as a collaboration and the respective contributions are as follows:

Lovish Gulati: LC ink and cell preperation, fabrication and printing optimization of 3D LC structures, actuation observation, SEM and POM imaging, data analysis.

Junhee Lee, Dr. Alexander Song, Dr. Kai Melde (IMSEAM, Heidelberg): Optical Holographic setup, generation of 3D light intensities patterns, imaging and optimization

Reza Norouzikudiani (SSSA, Pisa), within the STORM-BOTS training network: COMSOL modelling for LC actuation. His results are also shown in the results just to compare the experimental observations with the simulation predictions.

Dr. Carlos Sánchez-Somolinos (CSIC, Zaragoza) for providing the chemical inks for this study.

5.4 Publication

The results of this study will be published. The manuscript is being prepared and includes the same results, material, and figures of this chapter.

5.5 LC ink

The ink formulation (provided by Dr. Carlos Sánchez-Somolino, CSIC) was prepared that can be used at room temperature for printing LC structures. For this study, ink formulation contains A6OCB(39.22 wt%), RM105i (39.22 wt%), 2R (19.6 wt%), and TPO (1.96 wt%), as inspired from literature.[36] The chemical structures of the ink components are shown in Figure 5.5a.

The purpose of choosing and preparing this specific ink formulation was to simplify the alignment and fabrication process at room temperature, eliminating the need for temperature control. This ink differs from the formulations used in results of Chapters 3 and 4, which contained non-reactive mesogens for field alignment control.

The ink components 6-(4-Cyanobiphenyl-4'-yloxy)hexyl acrylate (A6OCB), 4-Methoxybenzoic acid 4-(6-acryloyloxyhexyloxy)phenyl ester (RM105i), 4-(6-(Acryloyloxy)hexyloxy)phenyl 4-(6-(acryloyloxy)hexyloxy)benzoate (2R) were bought from Synthon Chemicals GmbH & Co. KG. The photo-initiator phenyl-bis(2,4,6-trimethylbenzoyl)phosphine oxide (TPO) was bought from Sigma–Aldrich. All the chemicals were used as received.

The ink was prepared by dissolving the mentioned amounts in dichloromethane. The glass vial containing the mixture is heated and kept at 80°C with magnetic stirring. The nematic phase

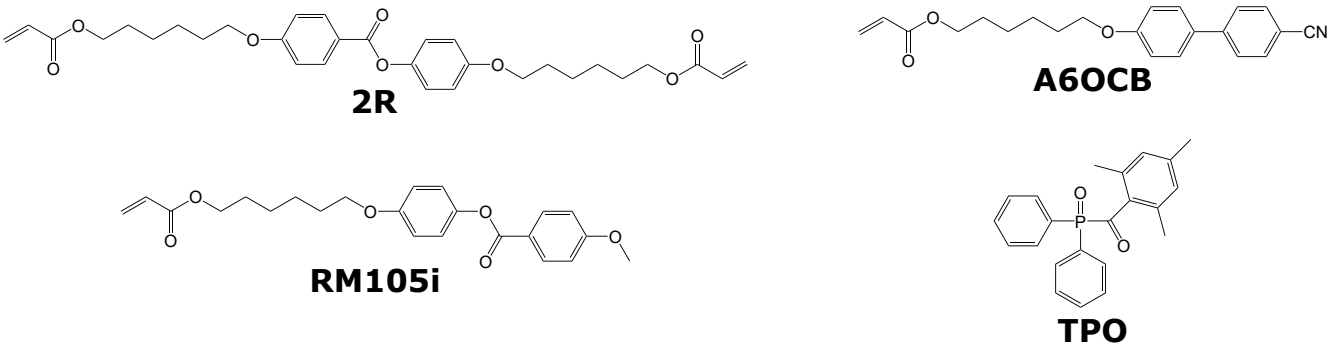

Figure 5.1: Chemical structures of the components used in the LC ink formulation.

of the ink can be obtained after all the DCM gets evaporated followed by slow cooling to room temperature.

LC cell preparation involves cleaning the glass slides sequentially by sonication in water, acetone, and isopropanol for 15-20 mins each. Then the substrates are dried and plasma-cleaned for about 10 minutes. Then, 5 wt% aqueous polyvinyl-alchohol (9000 Mw) is spin-coated at 4000 rpm for 60 seconds followed by heating at 90°C for about 5-10 minutes and slow cooling to room temperature. The prepared slides were then rubbed uniformly using a velvet cloth to achieve in-plane alignment along the rubbing direction. At the end, the LC cell is prepared using 100 μm spacers.

5.6 Comparison of sequential and single-shot printing

One of the limitations of layer-by-layer or voxel-by-voxel printing is that the alignment at the interface is distorted.[44, 57, 58] Here, we compare LC rectangular bars printed using sequential multiple exposures with those printed using a single-shot exposure. Figure 5.2 shows the LC bar printed section by section where each section is polymerized through a single exposure separately. Figure 5.2a-c, shows the light exposures for shots 1-3 to print the corresponding area in LC cell that is exposed to the light in Figure 5.2e-g respectively. One can see that the alignment at the boundary of each section is a bit distorted. To confirm that the sections are properly polymerized, the whole area of three sections is exposed in shot four and one can observe that there is no significant change in the structure, as seen in Figure 5.2h.

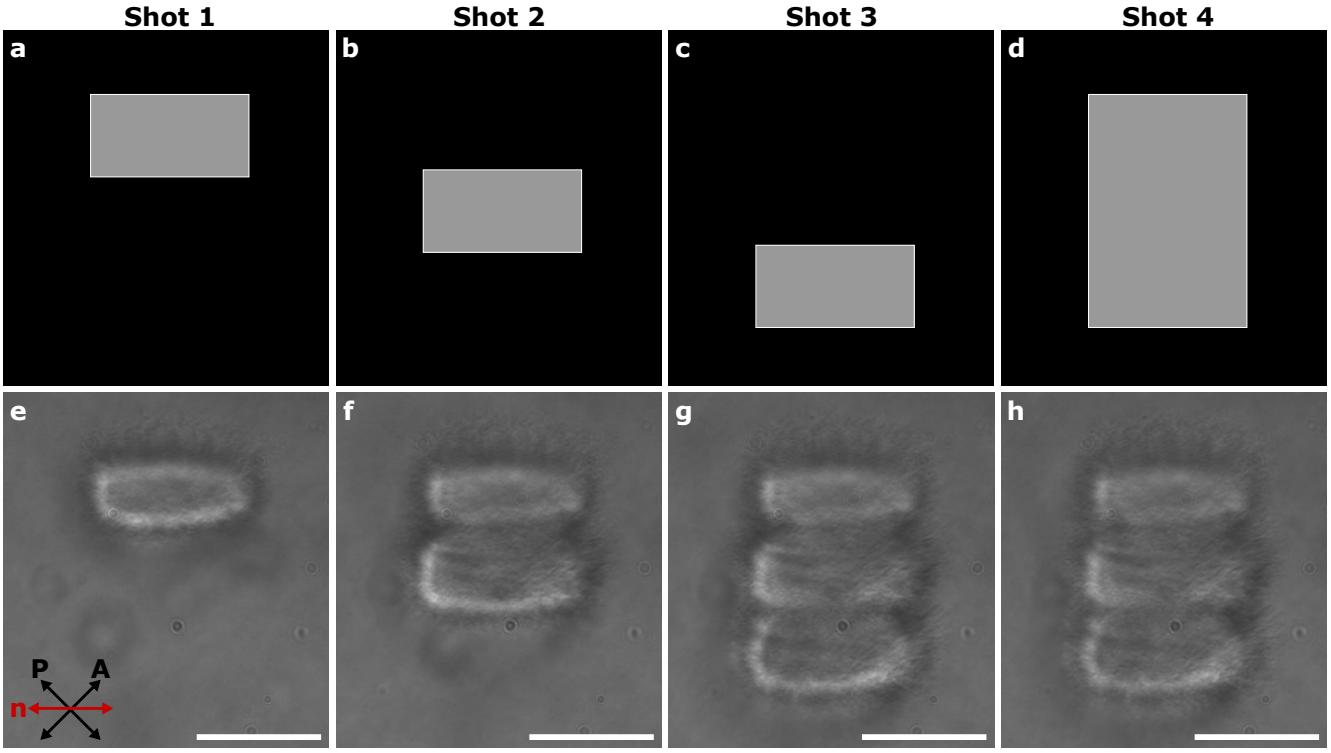

Figure 5.2: **Sequential printing to fabricate larger polymerized structures.** a-d) The target areas/sections for the single-shot light exposures, where grey and black colors indicate areas with light and no light, respectively. e-h) The printed sequence of sections in the polymerized structure in response to the exposed light in a-d. The interfaces between the sections are clearly visible. The final exposure in (d) is used to confirm whether the sections are completely polymerized during exposures in (a-c). The scale bars are 20 μm.

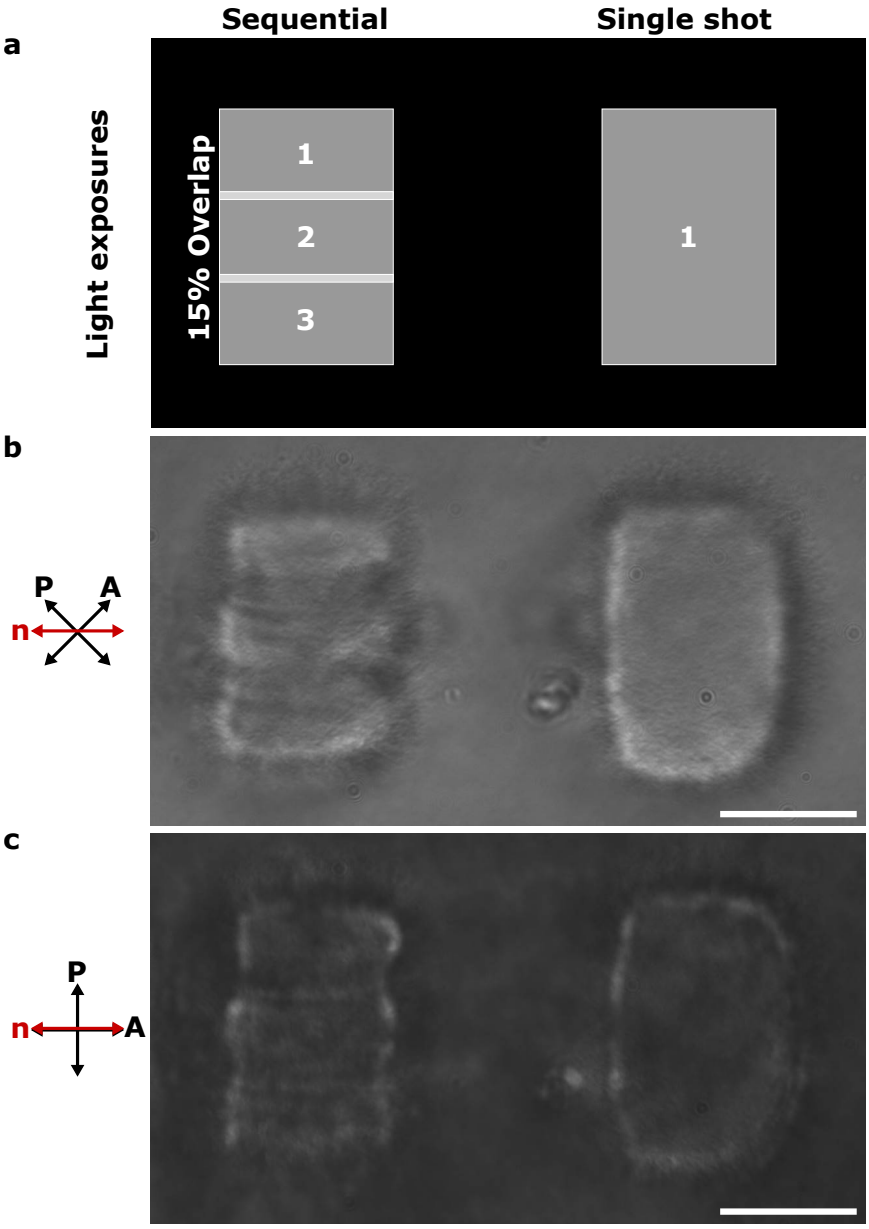

Figure 5.3: **Comparison of sequential vs. single-shot exposure for printing larger structures.** a) The total light exposure used for each section, where the sequential approach polymerizes each section separately, and the single-shot approach uses just one exposure for all the sections collectively. The total exposed area in both cases is the same. However, there is a 15% overlap in the areas exposed in the sequential step so that the interfaces are completely polymerized. b-c) Polarization optical microscopy images of the printed structures. Single-shot exposure polymerizes all the sections uniformly without the formation of any interfaces, in contrast to the sequential approach where interfaces and director distortion at the interfaces can be easily observed. The scale bars are 20 μm.

This sequential printing can be compared with the single shot parallel printing of the whole bar where the entire structure is exposed simultaneously at once. Figure 5.4 summarizes the visual observation of the print quality. The total exposed areas of the two cases are equal. The exposured areas in the sequential printing overlap by 15% so that the interfaces are completely polymerized. In Figure 5.4b-c, one can see that parallel single shot printing keeps the alignment uniform without the formation of interfaces that cause director distortion in case of sequential printing.

It can be concluded that the parallel printing can be effective in fabricating complex structures specifically for 4D LC robotic structures.

5.7 Optical holographic lithography

In 2D, the exposed area can be easily controlled by designing the appropriate masks. However, controlling the exposed volume elements in 3D space is more challenging and requires the spatial 3D modulation of the light.

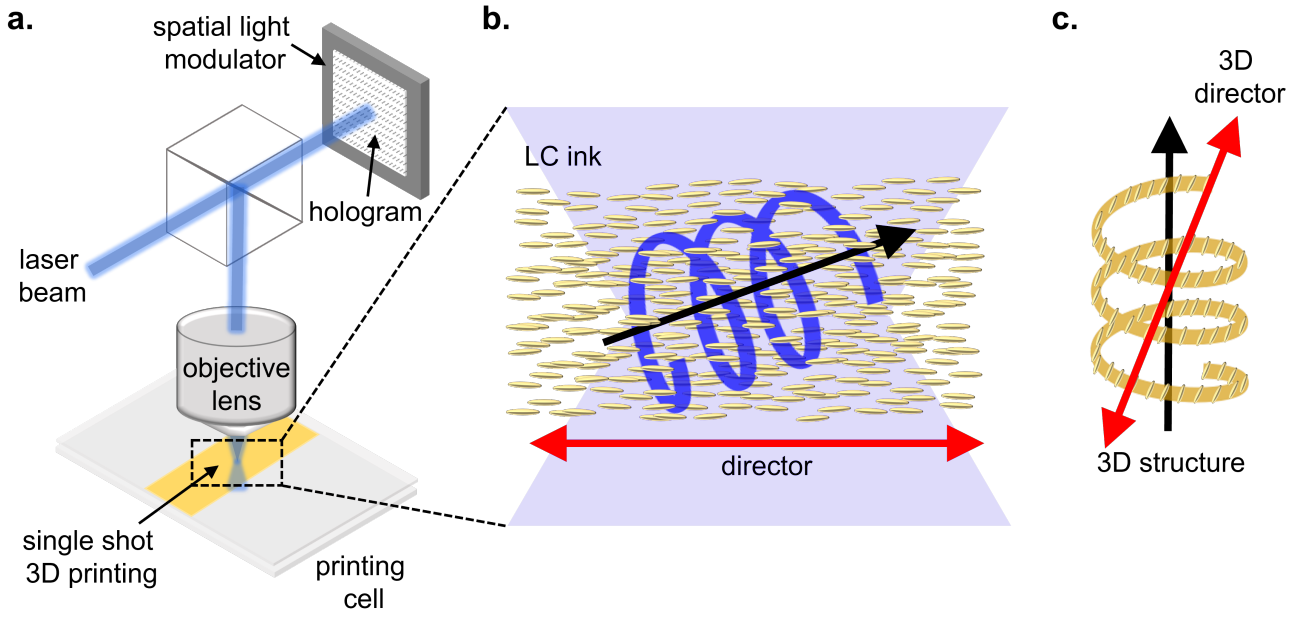

Figure 5.4: **Optical holographic lithography.** Schematics (not to scale) illustrating the single-shot parallel printing. a) The light is phase-modulated using a spatial light modulator (SLM) depending on the digitally calculated hologram, and the generated 3D intensity pattern is focused inside the printing cell using an objective lens. b) Single-shot exposure of the generated light intensity pattern of a 3D spring. The uniformly aligned LC ink is polymerized only in the regions of high intensity. The orientation of the structure is independent of the director alignment. c) The printed 3D LC Spring with a fixed 3D global director alignment.

Here, we use optical holographic lithography to shape the light in the desired 3D patterns

and expose the bulk LC ink in a single exposure to parallel print the whole 3D LC structure directly in the printing cell. The setup involves a spatial light modulator (SLM) that modulates the light according to the digitally calculated hologram. This hologram is calculated by using a 3D Computer-Generated Holography (CGH) algorithm with non-convex optimization as discussed in the literature.[102]

Please note that this OHL setup was built in our lab by my colleagues Junhee Lee, Dr. Alexander Song and Dr. Kai Melde and I, the author of this thesis, have used the setup to fabricate 4D LC structures of this study.

5.8 Printing 2D structure

The following demonstrates that OHL method can be used to print 2D structures and the director can be oriented in any arbitrary orientation within the polymerized material. To show this capability, we prepared uniformly inplane rubbed LC cells and projected light patterns in the shape of letters A, B, C and D using the SLM that formed the corresponding holograms. These light patterns were exposed to the bulk LC ink to print structures. Figure 5.5 shows that the director alignment can be controlled in any desired orientation within the printed letters independent of the structure geometry. The contrast changes can be observed in the polarization optical microscopy images where each row of the Figure 5.5 corresponds to the director alignment at angles 0°, 15°, 30° and 45° respectively. The red and black arrows indicate the director and optical axes of the polarizers for each case.

These 2.5D structures were anchored on the substrate with bottom flat surface and hence prevented from drifting out of the field of view during imaging in the microscope. To confirm whether the director is fixed inside the bulk polymerized LC, the cell was heated to 80°C causing the nematic to isotropic transition of the unpolymerized ink. This enables us to observe the director alignment within the polymerized structures as only polymerized structures remained visible under POM. The contrast of the letters depends on the molecular alignment as desired before the printing which confirms that the director orientation can be fixed inside the printed structures.

As seen in the Figure 5.5a, the structures appear dark confirming the director alignment along the polarizers. The contrast increases as the director is oriented at angles 15°, 30° and 45° as seen in Figure 5.5 respectively. There are slight misalignments and shape differences that could result from imperfections in the rubbing alignment and deformations due to heating. Even though, the edges are not sharp and the polymerization seems to extend beyond the desired areas, the shapes

remain recognizable with their POM contrast, which depends on the director orientation. This demonstrates that the proposed method allows the printing of 2D LC structures with independent and defined molecular orientation with respect to the structure's geometry.

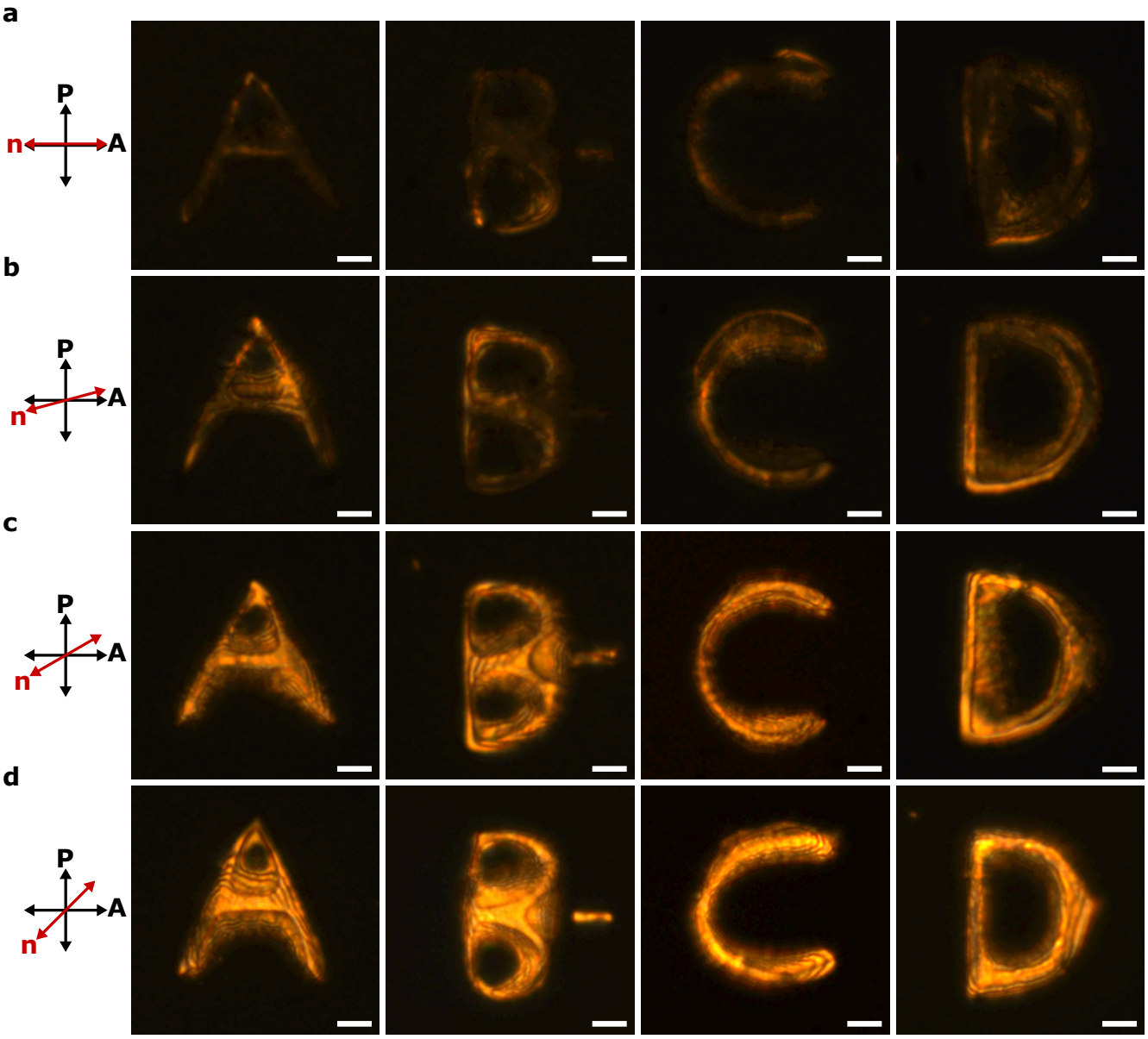

Figure 5.5: **Printing letters A-D with different global director alignments.** a) Chemicals used to prepare the LC ink formulation for printing structures. b-e) LC structures in the shapes of letters A and B printed with different in-plane director alignments. The rows display structures with alignment directions along $\varphi = 0^o$, 15^o, 30^o and 45^o respectively. The polarizer and analyzer optic axes are shown in black, while the director alignment is indicated by the red arrow. The scale bars are 20μm.

5.9 Printing 3D structure with independent 3D director

The OHL fabrication method can also be used to print complex 3D LC structures that cannot be realized using traditional techniques. Since the method allows the 3D shape of the polymerized ink to be defined solely by the 3D light intensity patterns, the director alignment is not coupled with the axis of the geometry. This capacity unlocks all three degrees of freedom in both structural design and director control. Similar to different geometries, each orientation of the same geometry also requires a different 3D light intensity pattern, and hence, different hologram calculations. Therefore, there is no need to modify the setup; we can print different structures with different orientations by using the corresponding hologram on the SLM.

The following structures were printed to demonstrate the capability of the method:

5.10 3D spring-shaped LC structures

3D LC Springs with 3 orthogonal director alignments were fabricated as shown in Figure 5.6. The LC Spring-X has its director alignment along the x-axis, which is the long axis of the spring. LC Spring-Y has its director along the y-axis, corresponding to the short axis of the spring. Both were printed in a homogeneously aligned LC cell. LC Spring-Z is printed in a homeotropic cell, such that the director is aligned along the z-axis, which is seen as the out-of-plane short axis.

The structures are printed and designed in a way that allows them to anchor on the substrate, making it easy to compare their actuation mechanisms, which depend on the director orientation within the body of the spring. Since the helical shape has a cylindrical bottom, the anchoring does not completely hinder the actuation, and the structures can still exhibit significant deformation.

The actuation simulations were predicted by our collaborator, Reza Norouzikudiani from SSCA, Italy, within the STORM-BOTS network.

Figure 5.6 illustrates the simulation predictions and the experimental observations of the actuating 3D LC Springs. The displacement field shown in the simulation is calculated for each structural element. The anchoring area was also taken into account, which was identified as the part of the structure that was fixed and, therefore, could not actuate in the observations. The colored scale bar for the displacement field is kept the same for all three cases, with blue indicating small displacements and red corresponding to large displacements. Both 3D visualizations and their 2D in-plane projections are shown in the first and second columns of Figure 5.6, respectively. During actuation, the structures contract along the axis of the director alignment and expand perpendicular to it, as expected. Since these three springs have different 3D director alignments with

respect to their body axis, the observed mechanical response is director-dependent and therefore varies for each case. Their responses are visually compared with each other as indicated by the blue and red bounding boxes for T = 80°C and 180°C, respectively.

Considering the LC material to be incompressible with uniform deformation due to a decrease in the order parameter, the observed contraction should be approximately the square of the observed expansion, as every 3D structure can be considered a cut-out part from a 3D cubical volume that uniformly contracts and expands along different axes depending on the director alignment. However, one can observe that the contraction is smaller than the in-plane expansion in the perpendicular direction. This could be due to the anchoring of the structures or possibly different expansions in the two orthogonal directions. Furthermore, there is a slight difference in the shapes of all the spring cases at $T = 80°C$, as there is some structural deformation between room temperature and $T = 80°C$, which was not recorded in our observation cycles. Nevertheless, the measurements show that the springs do exhibit mechanical deformation depending on the 3D director alignment, verifying the successful demonstration of the method to print the same 3D LC actuators with independent 3D director alignment, hence exhibiting different 3D stimuli responses.

5.10.1 Reversible and repeatable actuation

The mechanical deformations of the structures were recorded in response to the changes in temperature between $T = 80°C$ and $T = 180°C$. During the temperature cycle, the structures relaxed back to their original shape upon cooling, as seen in Figure 5.7a-c. The repetition of 3 cycles was observed to verify the reversibility and repeatability, and the average response follows the predictions by the simulation, as shown in Figure 5.7d-f. For example, in the case of LC Spring-X, the contraction along the x-axis and in-plane expansion along the y-axis in response to the temperature changes is measured in Figure 5.7d. The mean value and the standard deviation are also calculated to show its repeatability. The cooling cycle also shows similar values. There is a slight variation in the deformation measurement between heating and cooling cycles for the same temperature values, which could be due to the different temperatures of the LC cell and the indicated measurements by the heating chambers. Overall, the nature of the deformation matches well with the simulations, as indicated in Figure 5.7d. Similarly, this is also true for the cases of LC Spring-Y and LC Spring-Z, as shown in Figure 5.7e and f, respectively. All these results verify that this method has great potential for printing complex 3D LC actuators with arbitrary 3D global director profiles, capable of undergoing reversible and repeatable mechanical actuation.

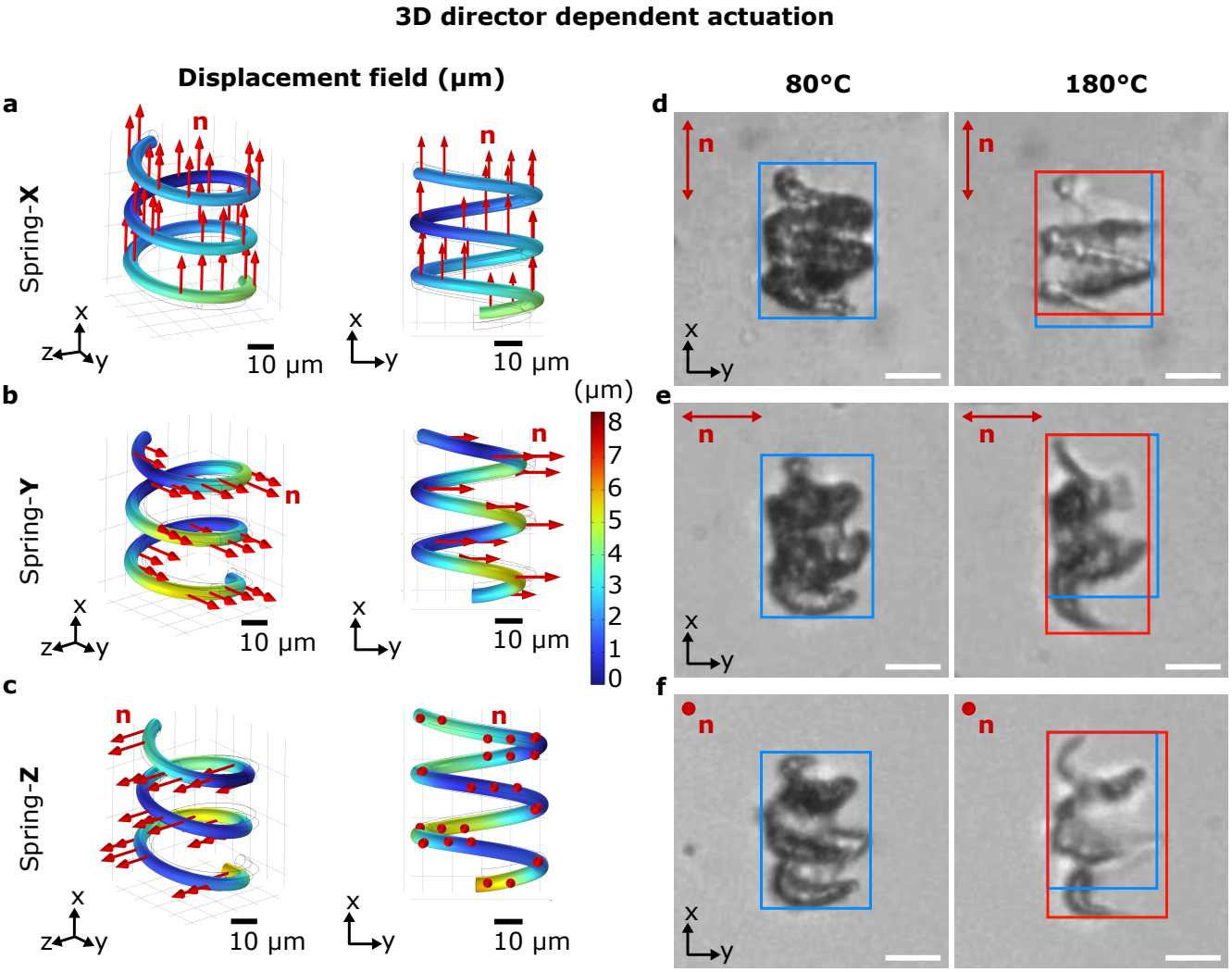

Figure 5.6: **3D spring-shaped LC structures with different orthogonal 3D director alignments and their thermal actuation behavior**. a)-c) Simulation visualizations of the displacement field (in μm) in 3D space and their 2D projection in the x-y plane. The director orientation along the x, y, and z axes is indicated by the red arrows for a) LC Spring-X, b) LC Spring-Y, and c) LC Spring-Z, respectively. Multiple arrows pointing in the same orientation in the structure indicate the global director alignment in the entire 3D geometry. Upon actuation, all the structures exhibit director-dependent mechanical deformation, where the color scale bar shows the displacement fields for all the elements of the printed geometry upon actuation to high temperatures. a) LC Spring-X: With the director along the spring's long axis, it contracts along its body axis and expands perpendicular to it. b) LC Spring-Y: The director is aligned along the y-axis, the same as the spring's in-plane short axis. It contracts along its short in-plane axis and expands orthogonally to it. c) LC Spring-Z: The director is aligned homeotropically along the z-direction, and therefore, the structure expands in both the x- and y-axes. d)-f) Observed thermal actuation of the LC Spring-X, LC Spring-Y, and LC Spring-Z, respectively. The bounding blue and red boxes show the outer in-plane dimensions of the structures at T = 80°C and 180°C, respectively, to compare their mechanical deformation for each case of the springs. The scale bars for the simulations in a)-c) are 10μm, and for experimental observations in d)-f), they are 20μm.

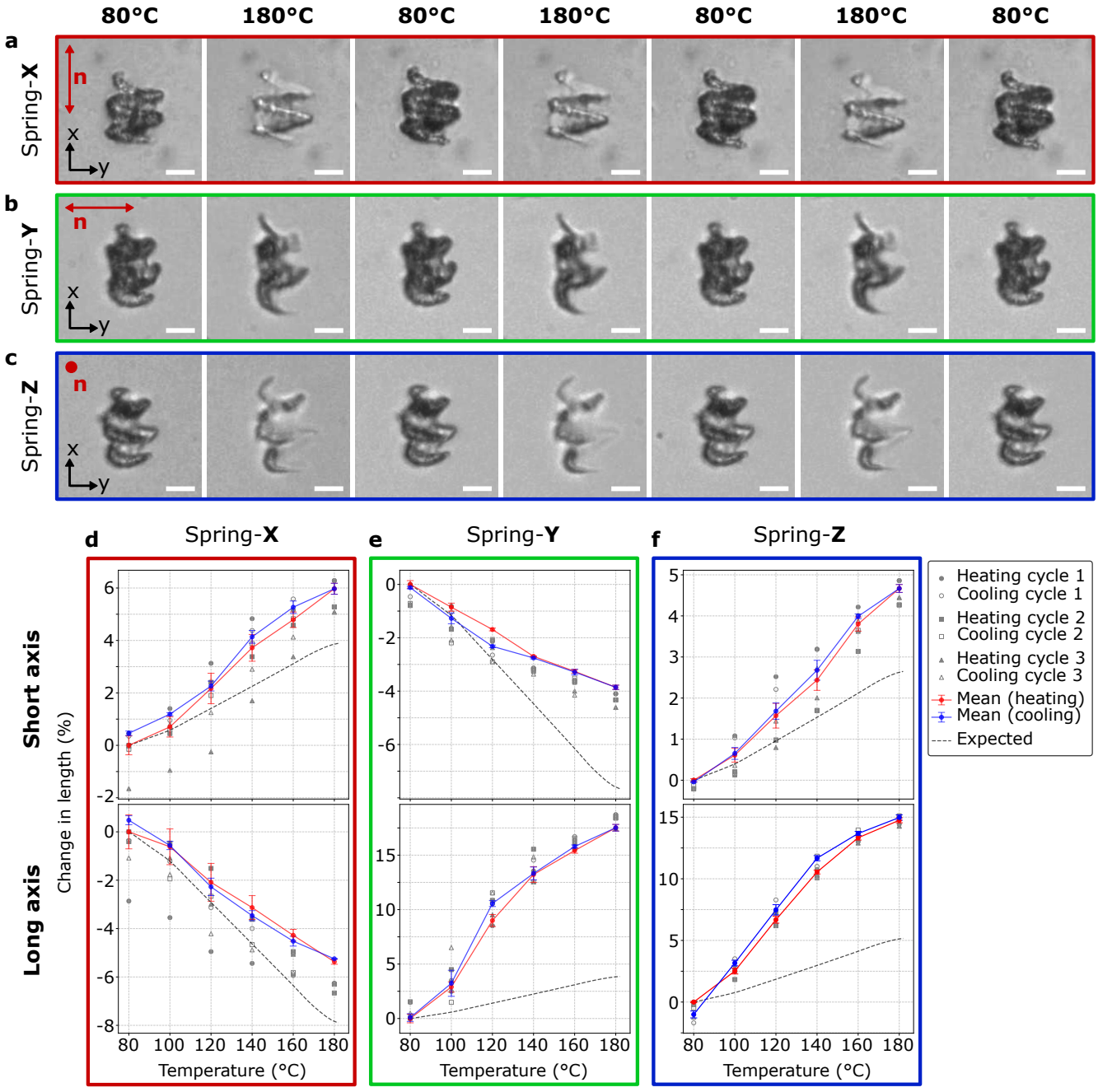

Figure 5.7: **Reversible and repeatable actuation cycles of printed LC Springs.** a)-c) Observed actuation during three heating and cooling cycles for LC Spring-X, LC Spring-Y, and LC Spring-Z, respectively, between $T = 80°C$ and $T = 180°C$. The director alignments are indicated with red markers. d)-f) Plots for the expected and observed actuation behaviors for LC Spring-X, LC Spring-Y, and LC Spring-Z, respectively, along their short and long axes. The percentage change in the lengths for each heating and cooling actuation cycle is indicated with grey markers, and their mean values are plotted along with their standard deviations as error bars. The expected response is plotted by a dotted black line. The consistent data points for each cycle indicate that the actuation response is reversible, and the structures return to their initial states after cooling. Scale bars are 20 μm.

5.11 3D infinity LC Loops

The 3D infinity loop is considered an interesting shape because of its geometry and closed form, and hence, it is not easy to fabricate with other traditional techniques. Here, we demonstrate that the OHL method can be used to fabricate 3D infinity LC Loops, as shown in Figure 5.8a. The circular loop is printed very well as desired, and the uniform planar director alignment is also maintained after polymerization, as verified by the POM images in Figure 5.8b-c.

For actuation, the loop is designed such that it has two open ends, which can act as a reference to observe the mechanical response. For this study, the director is fixed along the x-axis, and we fabricated LC Loop-X and LC Loop-Y with perpendicular orientations to each other. This shows that the structure orientation can be directly controlled by different intensity patterns generated by different holograms. As shown in Figure 5.9, the open LC Loops are observed to have a non-uniform mechanical response, as also visually simulated. This complex behavior is due to the anchoring constraints that influence the free deformations. Although this mechanical actuation is reversible as well as repeatable, as shown in Figure 5.9.

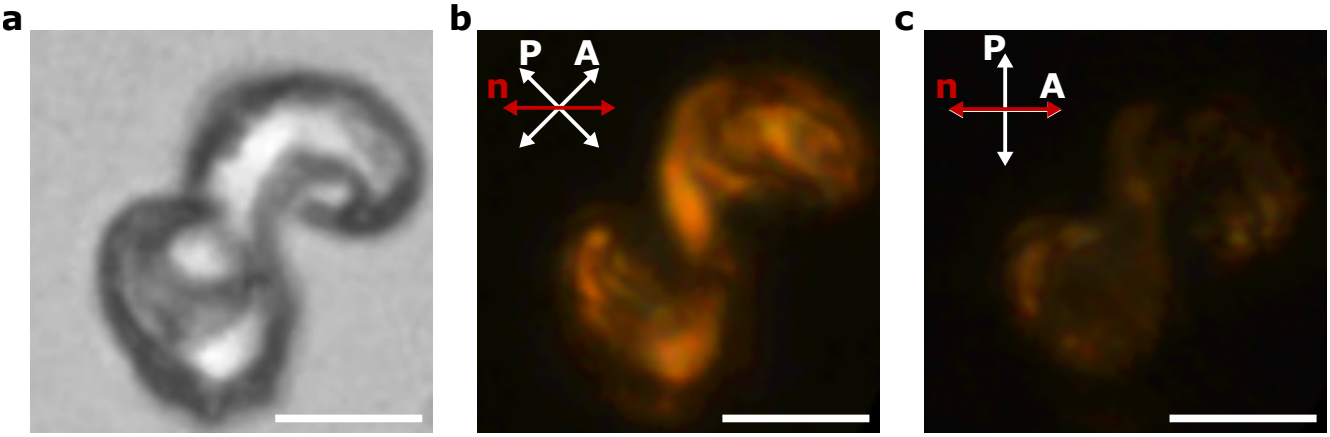

Figure 5.8: **3D infinity loop structure.** a) Printed 3D infinity loop using LC ink. c)-d) Polarized optical microscopy (POM) images of the LC Loop to verify the director alignment, which can be observed as dark and bright regions under crossed polarizers. The scale bars are 20 μm.

5.12 3D LC Flower

Another interesting complex 4D structure is the LC Flower, which is anchored at its base, with its petals remaining free to deform in 3D. In this study, the actuation of the flowers is compared depending on their in-plane orientation relative to the molecular orientation, as seen in Figure 5.10. Two flowers are printed next to each other, with one rotated in-plane by 45° compared to the other, and the director is in the x-direction in both cases. In LC Flower-1, the director

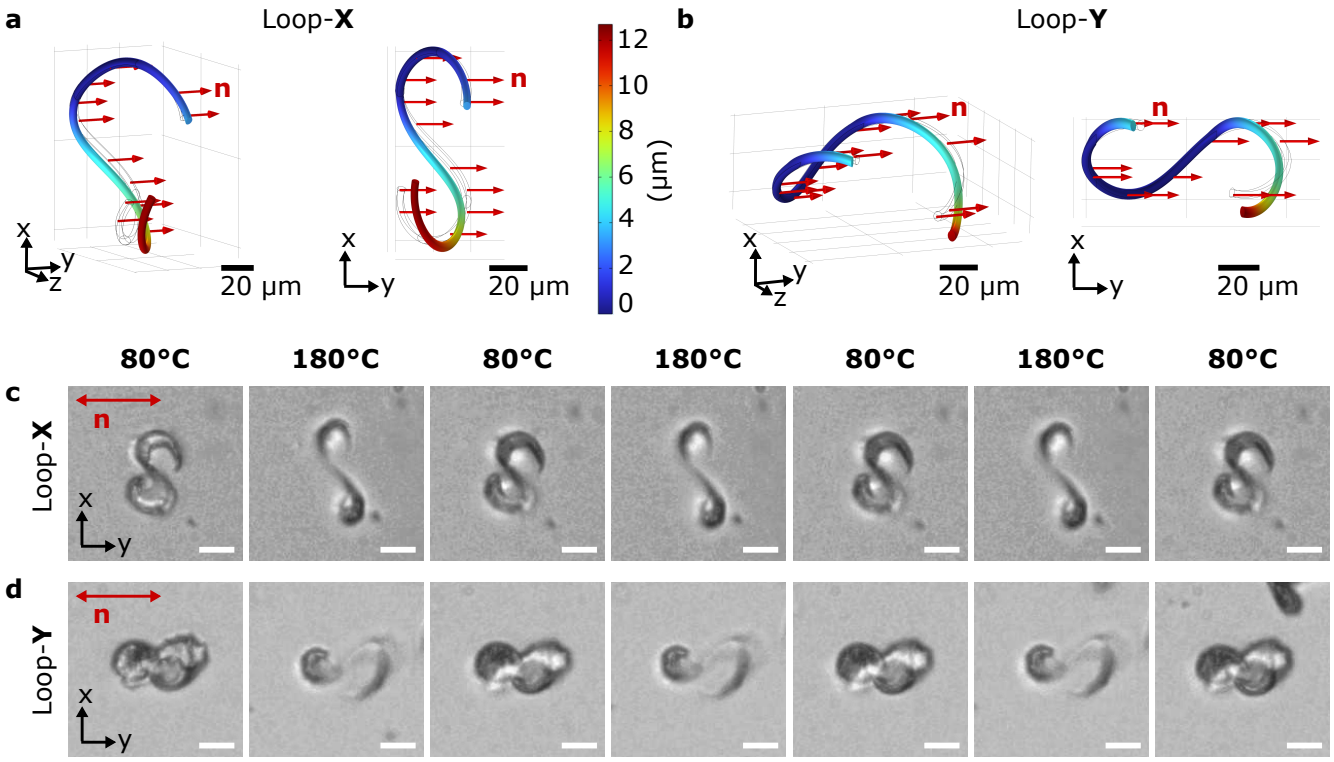

Figure 5.9: **Complex 4D LC Loops.** a-b) Simulation visualizations of the complex 4D LC Loops, shown in 3D and as 2D projections in the x-y plane. The orange-colored regions shown in the simulations correspond to areas anchored to the substrate in the printed structures. The director n is aligned in the x-direction in both cases, and the shape orientation of the printed structure is directly controlled by the phase-modulated light. These simulation results are provided by Reza Norouzikudiani (SSSA, Pisa) and are used in this thesis to compare with the experimental observations c-d) Observed thermal actuation during the 2nd, 3rd, and 4th heating-cooling cycles between $T = 80°C$ and 180°C for LC Loop-Y and LC Loop-X, respectively. The actuation behavior depends on the director orientation relative to the body axis. The scale bars for both simulations and experimental data are 20μm.

is aligned along one of the U-shaped components. As predicted in the actuation simulations in Figure 5.10a-b, this U-shaped component contracts with the decrease in its opening angle. On the other hand, the perpendicular U-shaped component showed a slight increase in the opening angle. The displacement between the tips of the U-shaped components is measured as the deformation parameter, as seen in Figure 5.10c. LC Flower-2 is printed with a 45° in-plane rotation compared to the director alignment. Here, the director can be considered to point along the face diagonal of the imaginary LC cuboid. The simulations in Figure 5.10a-b predict that the angle ϕ between the two U-shaped components increases. This response indicates a change in the angle between the face diagonals of the 3D cuboid that undergoes contraction and expansion parallel and perpendicular to the director. The observations and their plots can be seen in Figure 5.10c-f. Furthermore, this printed flower can also be viewed from the side in the x-z plane, with the director along the y-axis, and the change in angle θ is observed as depicted in Figure 5.10g. The response is also predicted in the simulation, where the base is considered anchored. In the experiments, the outer dimensions

are shown by the bounding boxes in red and blue. In LC Flower-1, the observed contraction aligns well with the simulation's expectations. However, the observed perpendicular expansion is very small. On the other hand, LC Flower-2 deformed significantly in both orthogonal contraction and expansion. Therefore, the weak expansion observed in the case of LC Flower-1 may be because the flower tips are not clearly visible in their 2D projection.

The 3D image of the LC Flower can be observed in the scanning electron microscope (SEM) as shown in Figure 5.11a. Before imaging, the structures were washed in isopropanol at 60° for about 10 minutes. Furthermore, both the 3D profile and the director alignment can be visualized in the freely floating LC Flower-2, as shown in Figure 5.11b, with their X and Y faces showing bright and dark contrasts, respectively. This verifies the director alignment along the y-axis.

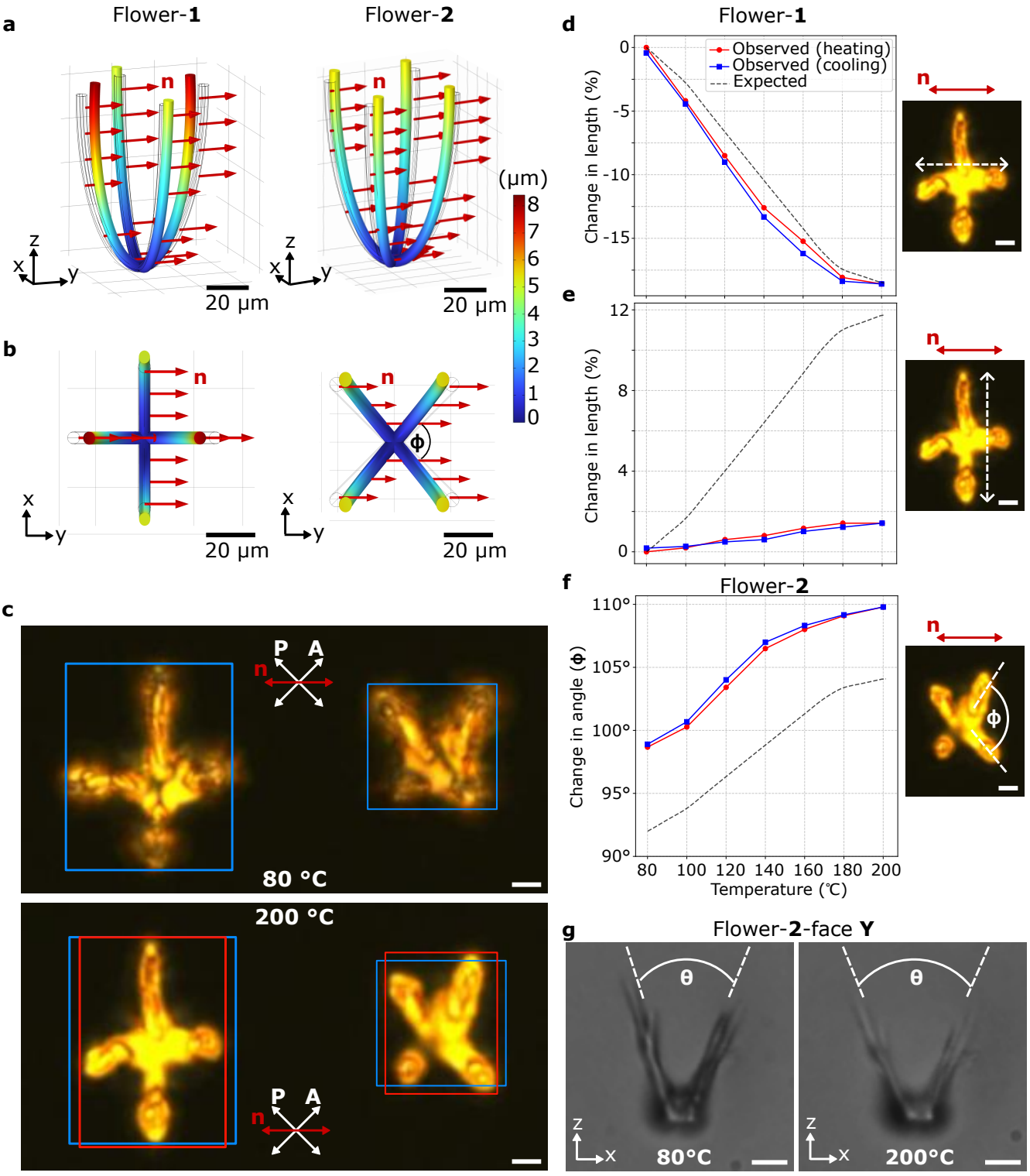
a
Flower-1
Flower-2
n
z
x
y
20 μm
(μm)
8
7
6
5
4
3
2
1
0
b
n
ϕ
x
y
20 μm
c
P
A
n
80 °C
200 °C
d
Flower-1
Observed (heating)
Observed (cooling)
Expected
Change in length (%)
0
-5
-10
-15
e
12
8
4
0
f
Flower-2
Change in angle (ϕ)
110°
105°
100°
95°
90°
80
100
120
140
160
180
200
Temperature (℃)
g
Flower-2-face Y
θ
80°C
200°C

Figure 5.10: **3D LC Flower with 4 petals** a-b) Simulation visualizations of the actuating LC Flower structures in 3D and their 2D projection in the x-y plane. LC Flower-1 and LC Flower-2 are printed with an in-plane rotation of 45°, with the director 'n' aligned along the common y-axis. The displacement field values are represented using a color scale bar, where red indicates large displacements of approximately 8μm, and blue represents minimal displacements. c) Both flowers are printed side by side, and their thermal actuation is observed under a polarized optical microscope at T = 80°C and 200°C. a-c) LC Flower-1: The director is aligned within the plane of one of the U-shaped components. Upon actuation, this alignment causes one U-shaped component to contract, reducing its opening angle, while the perpendicular U-shaped component expands slightly, increasing its opening angle by a few degrees. d-e) Simulated plots and measured changes in the displacements of the tips of the two individual U-shaped components are shown, as indicated in the insets. a-c) LC Flower-2: The director is aligned at 45° relative to the plane of the U-shaped components. Thermal actuation results in a change in the angle φ between the planes of the U-shaped components. f) Expected simulation plots and measurements (as indicated in the inset) illustrate the decrease in φ upon heating. g) Side view in the x-z plane, where the opening angle θ is seen to change upon actuation, as expected in the simulations. The scale bars are 20 μm.

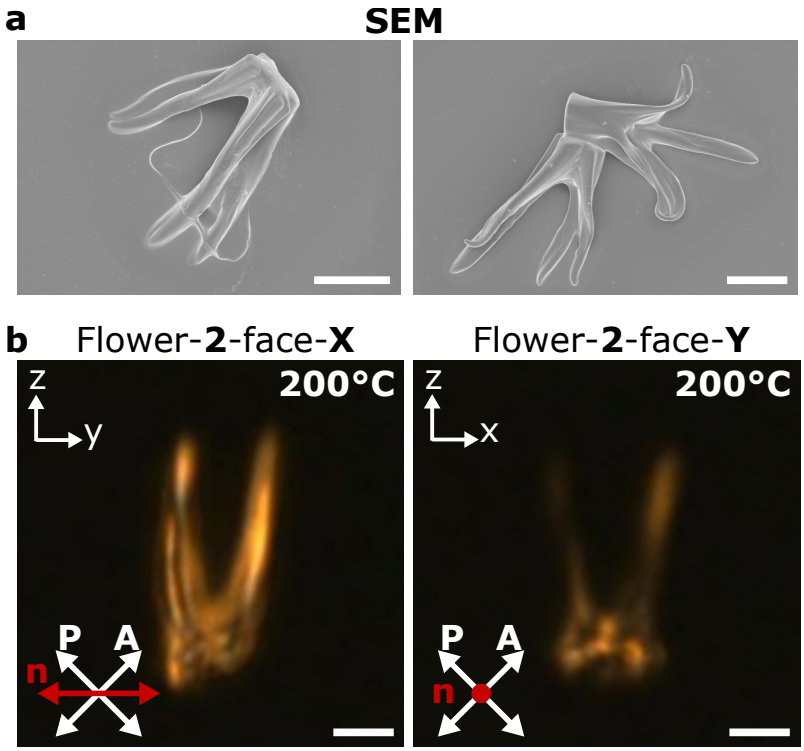

Figure 5.11: **3D Imaging of LC Flower** a) Scanning electron microscopy images of the 3D LC Flower microstructure. b) POM of freely floating LC Flower-2 to observe its director alignment and 3D shape from different angles. Since LC Flower-2 is printed with its alignment at 45° to the plane of both U-shaped orthogonal components, face-X is observed to have in-plane alignment, while face-Y appears to have homeotropic alignment. The scale bars are 20 μm.

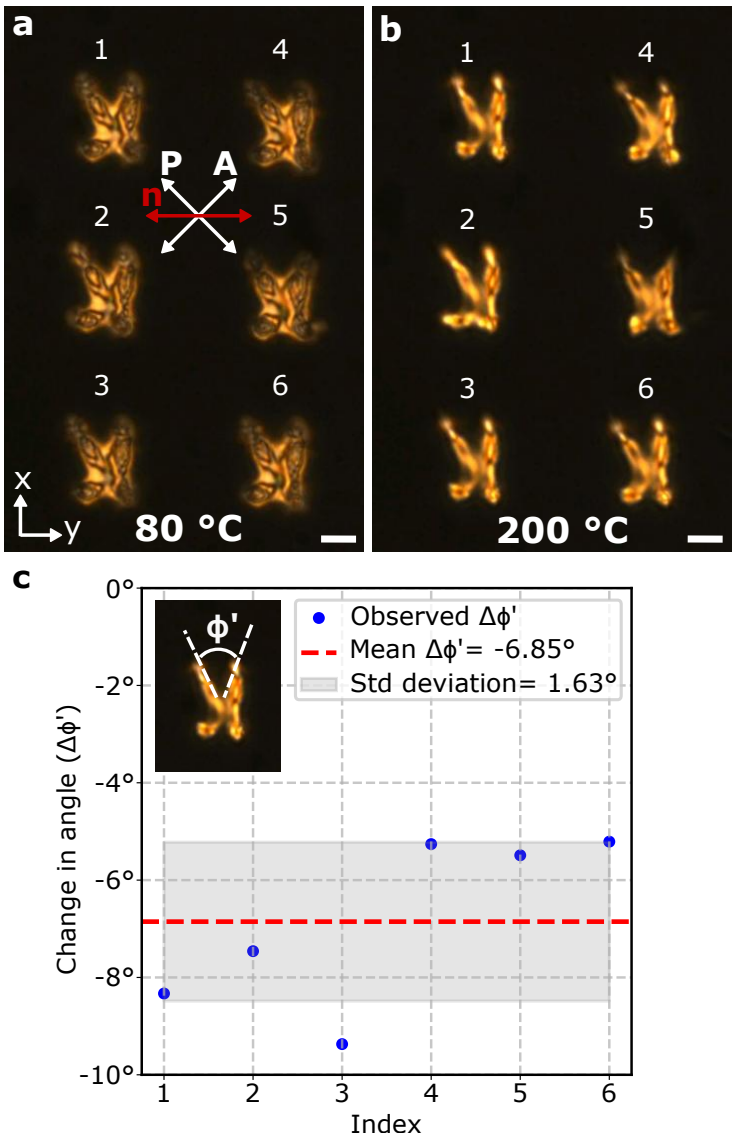

Figure 5.12: **Reproducibility of the printed technique.** A 2x3 array of the LC Flower-2 microstructures was printed, and their thermal actuation was compared. a)-b) POM images of the structures at 80°C and 200°C are shown, respectively. c) The angle $\phi' = 90 - \phi$ is measured for all the flowers individually and plotted with its mean and standard deviation (std) values. The similar response of all the structures confirms the reproducibility of printing 3D structures with fixed and desired 3D alignment. The scale bars are 20 μm.

5.12.1 Discussion

It has been shown that holographic microlithography can be used to fabricate entire 3D complex microstructures in a single short exposure. This parallel printing technique fixes the global director alignment in the structure. The 3D director alignment can be independently controlled relative to the object's axis by choosing the orientation of the printed structure. Another important aspect is that the parallel printing also avoids the formation of interfaces and director distortions.

The OHL technique enables faster printing of large objects compared to voxel-by-voxel or layer-by-layer techniques. The printing speed for each structure varied from 0.05 to 0.1 seconds,

depending on the structure design, thickness, and size. Furthermore, the print resolution, as seen in the experimental images, is around 5 μm.

The ability to control the 3D director in any arbitrary orientation, irrespective of the object geometry and orientation, is very exciting, as it opens up the capability to realize complex 3D shapes and their responsiveness to stimuli.

Another major advantage of this method is that it allows printing of complex shapes at room temperature without the need to heat the ink to high temperatures for printing and alignment, in contrast to traditional DIW and DLP methods.[37–41, 52, 53, 57]

The fabricated structures show reversible and repeatable actuation depending on the 3D director alignment. Hence, we believe that this OHL technique is a reliable method for studying the complex mechanical responses of 4D LC microactuators.

We also checked the reproducibility of the printing method, where the same LC Flower-2 structures were printed in a 2x3 array. Figure 5.12 shows that the prints not only look very similar, but their mechanical actuation is also fairly consistent. The plot summarizes the change in the angle ϕ' for all structures, a mean value of -6.85° and a standard deviation of 1.63°. This gives 23.7% ratio of standard deviation and mean value, which is quite significant. This signifies that the printing or alignment process can be improved as well. Imperfection in the alignment and shape of the printed object both can affect the actuation. Overall, this verifies the reproducibility of the fabrication by the OHL method, and hence, it can potentially be used for mass fabrication of complex 4D structures after some improvement either in the ink composition or alignment process or the exposure optimization.

Although this study only utilized uniform global alignment to demonstrate the capability of the printing method, future directions could involve using spatially patterned substrates to realize 3D complex LC microstructures with 3D arbitrary spatially varying director profiles.

5.13 Conclusions

This study demonstrates that single-shot optical holographic lithography can be used to parallel print the entire 3D microstructure in a single short exposure time, with 3D global director alignment independently controlled relative to the object. The parallel printing not only avoids the formation of interfaces or any distortions in the director, but is also capable of potentially printing at faster speeds compared to other traditional techniques. Another advantage is that it enables printing to be done at room temperature, without the need to heat the ink for alignment and printing steps. Complex 4D actuators such as LC Springs, LC Loops, and LC Flowers were

fabricated in a single short exposure, with 3D global director alignment independently controlled, irrespective of the structure's orientation. Experiments showed that the fabricated microstructures exhibit reversible and repeatable mechanical actuation as a factor of the LC director alignment, and their deformations agree well with the simulation predictions. This technique also supports reproducible fabrication, which is required for mass production. OHL therefore enables parallel printing in a single exposure with a higher degree of 3D control over both the structure's geometry geometry while allowing for independent global director alignment, paving the way to develop complex LC robotic functions, potentially for industrial-scale fabrication of 4D actuators.

6 Conclusions

In this thesis, the challenges related to the 3D aspects of the spatial control of the LC director alignment are addressed, including characterization, and visualization, as well as single exposure holographic parallel printing. The focus is to independently unlock all three degrees of freedom, both in the director and in the structural shape, to precisely align, characterize, and fabricate complex 4D LC actuators at room temperature for advanced robotic functions.

In the first work, an LC gel ink is prepared that can be aligned at room temperature using low magnetic field strengths. The LCG ink-1 formulation, containing non-reactive mesogens (E7), shows a nematic phase at room temperature. LCG ink-2, prepared by adding 5CB to LCG ink-1, lowers the threshold for magnetic field alignment to 0.13 T, which is significantly lower than reported values in the literature. It is concluded that 5CB facilitates magnetic field alignment, and in response to the external field, uniformly present 5CB in the bulk LCG ink-2 guides other molecules to reorient along the same direction. In the experiments, thicker cells with a gap of 250 μm are used to minimize the effects of surface anchoring, resulting in an efficient alignment response. The actuation of the 2D film with uniformly aligned directors is observed to verify the director programming. In the fabrication setup, the applied magnetic field (and hence the director) can be easily oriented in any arbitrary 3D direction. This enables the fabrication of an LC ribbon with spatially patterned in-plane alternate director orientation angles. The POM images confirm the desired director pattern. The work is advanced to fabricate complex 3D optical elements with a spatially varying 3D director profile. An example of an LC Wollaston prism is demonstrated, which has two sections (optic axes) whose directors are orthogonal to each other. This prism causes the light to split into two orthogonal y- and z-polarized beams, as both components experience different refractive index changes while refracting from one section to the other. The method advances the capability to fabricate custom and complex 3D optical elements and LC actuators that cannot easily be realized with other traditional techniques.

In the second part, an optical measurement technique is demonstrated to characterize 3D director alignment. In contrast to other microscopic techniques, where only 2D projections are

observed that indirectly determine the 3D orientation angles, the proposed method can visualize the 3D director in real time. This method is based on a wedge cell technique, where one can observe the splitting of the light beam into two orthogonal E-ray and O-ray components based on the 3D director alignment and hence the effective refractive index. The E-ray component has an electric field in the plane of the director and propagation direction, while the O-ray has an electric field vector perpendicular to it. The in-plane and out-of-plane angles are determined using polarization optics and the angular splitting of the beam. The relation between angular splitting and effective refractive index is derived and plotted as a function of incidence angles and in-plane and out-of-plane director orientation angles. The observed splitting agrees well with the predictions that the angular splitting depends only on the out-of-plane angle, irrespective of the in-plane angle. The splitting increases with a decrease in the out-of-plane angle. Although the characterization process involves many parameters, the work provides a protocol for the fabrication of the wedge cell, choosing incident angles, and measuring the beam separation to easily determine in-plane and out-of-plane angles. The proposed method successfully provides a way to visualize the 3D director orientation, which can be very helpful in optimizing other alignment techniques, chemical ink formulations, temperature dependence, surface anchoring effects by polymer coatings, and diagnosing the quality of the achieved 3D alignment in the wedge cell. After successful determination and optimization, one can easily use the same parameters to fabricate nematic LC structures in parallel plate cells or other cell geometries.

In the third part, optical holographic lithography is demonstrated that allows the parallel-printing of complex 3D structures in a single short exposure, with the capability to fix the director in any orientations within the object, irrespective of the structure's orientation. This technique is utilized without requiring elevated temperatures. We show that the method is advantageous in avoiding the formation of any interfaces or distortions in the director, which are often seen in sequential printing. Interestingly, it is shown that phase-modulated light can generate 3D light intensity patterns, which can be exposed on the aligned LC ink to polymerize only the regions where the light intensity is high. This results in the polymerization of 3D structures after a single exposure with various director orientations. POM images verify that the director is fixed in place as desired. Complex 3D LC actuators are printed in the shapes of a 3D spring, 3D infinity loop, and 3D flower, each in different orientations. Each structure and its particular orientation require a different light intensity pattern, and thus different phase-modulated light. These 4D LC actuators undergo reversible, repeatable thermal actuation, depending on their 3D shape as well as their 3D global director alignment. All measurements are also compared with simulations, and the results match well with the predictions. The method is reproducible, thus

showing potential for mass fabrication of complex 3D LC actuators. Some improvement in the alignment or ink composition may help to achieve better reproducibility. OHL not only establishes parallel printing in a single short exposure but also unlocks the 3D capability for both complex structural shapes and independent global director profiles. In summary, it provides a way for the fast fabrication of complex 4D LC robotic structures, with potential for large scale production.

6.1 Outlook

This thesis has provided a solution to program complex 3D spatially varying directors using low fields. The work can be extended to explore LC inks without incorporating non-reactive mesogens to achieve complete crosslinking and high integrity. Furthermore, one could also incorporate magnetic inclusions that respond to lower fields and guide the reorientation of mesogens through local interactions to achieve global director alignment. In this case, the problem of aggregation of magnetic particles should be solved, as their presence in the LCs can act as defects. To achieve control over the local interactions with mesogens, specific surface treatments would be required to induce the magnetic alignment response.

In the case of the demonstrated alignment, the director can be visually characterized in real time. However, the resolution of the splitting should be improved for inks with lower refractive indices and for the case of small divergence angles. Here, a weak value amplification scheme could be helpful when the alignment response is weak and the divergence of the beam is not significant.[99] This method is capable of amplifying the splitting between orthogonal components by carefully choosing a post-selection for the final polarization state of light, and permits the detection of nanoradian divergence angles.[99] This would help to enhance the sensitivity of the wedge cell technique to optimize and diagnose sample films with lower birefringence than 5CB.

Although a homogeneously aligned cell is used in this thesis for OHL printing of 3D complex shapes with independent 3D director alignment, one can also use a spatially patterned cell to achieve a spatially varying 3D director. Furthermore, by combining OHL with magnetic field alignment, one could print sequentially connected structures in 3D, where each section can have a different 3D shape and independent 3D director alignment. These steps will enhance the complexity and enable the printing of any 4D LC actuator that one can imagine. More work is required to improve the anchoring of the structures to the substrate or to collect them carefully after washing. It would be interesting to understand the effect of interfaces for spatially varying 3D directors. One possibility is to compare structures having a smoothly varying 3D director without any interfaces with structures having an abruptly varying 3D director with interfaces between different

sections. This will help in understanding the effects of body constraints and boundary conditions of the adjacent sections. Another possible direction would be to use 3D holographic microscopy to precisely observe the 3D deformations.

In conclusion, soft LC actuators show great potential for applications as they can be micro-fabricated and exhibit large deformations. These smart systems can open up new possibilities in sensing, micro-robotics, optical devices, and are the future key materials for science, technology, and society. Crucial is the director alignment for these applications and this thesis has developed new alignment and characterization techniques.

Acknowledgements

It is important to mention that this thesis not only concludes my doctoral research but also reflects the contributions and support of numerous individuals. I would like to express my gratitude to all of them here.

First and foremost, I would like to express my deepest gratitude to Prof. Dr. Peer Fischer, my supervisor. I am extremely thankful for providing me the opportunity to contribute to science and be a member of his phenomenal research group. I truly appreciate his immense support and guidance in exploring the world of liquid crystals. I also want to thank Peer for his personal guidance in showing me how to approach scientific problems effectively and for being a role model in managing difficult situations in both science and personal life with professionalism. During the last four years, Peer's door was always open whenever I needed his help. Thank you for believing in me.

I would also like to thank Prof. Dr. Frank Gießelmann for being my second supervisor, for guiding me throughout the project, and for providing the opportunity to learn about liquid crystals in your labs at the University of Stuttgart. Thank you for your valuable suggestions and support.

I would also like to express my sincere gratitude to Dr. Kai Melde and Dr. Alexander Song for their collaboration and guidance throughout the project, for teaching me valuable analytical skills, and for the exciting microscopy-related experiments and insightful discussions. Thank you for your continued support.

I would like to thank our collaborator and STORM-BOTS coordinator, Dr. Carlos Sánchez-Somolinos, for your support and for giving me the opportunity to be part of the STORM-BOTS community and to carry out a secondment in your labs at CSIC. I will remember our insightful discussions during the secondment, as well as at the STORM-BOTS conferences and boot camps.

Importantly, I would like to thank the thesis committee members Prof. Dr. Christine Selhuber-Unkel, Prof. Dr. Eva Blasco, and Dr. Kai Melde for evaluating this thesis work and for their helpful discussions.

I want to thank the entire MNMS group (2021–2025). My work would not have been so

enjoyable without all of you. I would like to thank, in no particular order: Dr. Mariana Alarcon Correa, Dr. Athanasios Athanassiadis, and Dr. Nicolas Moreno Gomez for the training and all the lab-related help that kept me active in research; Dr. Dimitris Missirlis, Dr. Oscar Demeulenaere, and Dr. Jianfeng Li for the scientific discussions in the lab and during short breaks, which made my time at work truly enjoyable; Sai Nikhilesh Murty Kottapalli for technical skills, for all the office and life discussions that kept me focused and motivated; Junhee Lee for ongoing project collaboration and your helpful contribution; Rahul Goyal and Sahar Yosef Meir for all the technical support you provided me; and Lucie Motyckova, Florian Peter, Minghui Shi, Ida Saskia Bochert, and Setthibhak Suthithanakom for all the fun gatherings we had. Thanks.

Importantly, I would like to thank Jutta Heß, Corinna Scalet, and Benjamin Scherke for their help with all the paperwork related to my stay, travels, and lab supply orders. I was able to focus on my research activities because of their constant support.

Thanks to Rajat Kamboj, Dr. Guratinder Kaur, Ankit Mishra, and Gaurav Dave for always being there to boost me up during this journey. Our long chats and discussions on science and entertainment made my time more enjoyable.

Finally, I would like to thank my family for supporting me throughout my life. I would not have achieved this success without their role. I want to thank my grandfather, Sh. Tilak Raj Gulati, and my father, Mr. Davinder Pal, for motivating and guiding me in building my career in science; my grandmother, Smt. Kailash Rani, and my mother, Mrs. Rachna Rani, for always being there for me; and my brother, Anmol Gulati, for all the fun we share in this life. Thank you all for your love and affection.

Bibliography

1. He, Q., Wang, Z., Song, Z. & Cai, S. Bioinspired design of vascular artificial muscle. *Advanced Materials Technologies* **4,** 1800244 (2019).
2. Ware, T. H., McConney, M. E., Wie, J. J., Tondiglia, V. P. & White, T. J. Voxelated liquid crystal elastomers. *Science* **347,** 982–984 (2015).
3. Godman, N. P., Kowalski, B. A., Auguste, A. D., Koerner, H. & White, T. J. Synthesis of elastomeric liquid crystalline polymer networks via chain transfer. *ACS macro letters* **6,** 1290–1295 (2017).
4. Gelebart, A. H. *et al.* Making waves in a photoactive polymer film. *Nature* **546,** 632–636 (2017).
5. Wang, Z., Li, K., He, Q. & Cai, S. A light-powered ultralight tensegrity robot with high deformability and load capacity. *Advanced Materials* **31,** 1806849 (2019).
6. Agrawal, A. *et al.* Stimuli-responsive liquid crystal elastomers for dynamic cell culture. *Journal of Materials Research* **30,** 453–462 (2015).
7. Roach, D. J. *et al.* Long liquid crystal elastomer fibers with large reversible actuation strains for smart textiles and artificial muscles. *ACS applied materials & interfaces* **11,** 19514–19521 (2019).
8. Hajiesmaili, E. & Clarke, D. R. Dielectric elastomer actuators. *Journal of Applied Physics* **129** (2021).
9. Ionov, L. Hydrogel-based actuators: possibilities and limitations. *Materials Today* **17,** 494–503 (2014).
10. Nguyen, P. H. & Zhang, W. Design and computational modeling of fabric soft pneumatic actuators for wearable assistive devices. *Scientific reports* **10,** 9638 (2020).
11. Ghosh, A. & Fischer, P. Controlled propulsion of artificial magnetic nanostructured propellers. *Nano letters* **9,** 2243–2245 (2009).

12. Palagi, S., Singh, D. P. & Fischer, P. Light-controlled micromotors and soft microrobots. *Advanced Optical Materials* **7,** 1900370 (2019).

13. De Gennes, P. The Physics of Liquid Crystals. *Oxford Clarendon Press google schola* **2,** 1625–1627 (1993).

14. Wojtowicz, P. J., Sheng, P. & Priestley, E. *Introduction to liquid crystals* (Springer, 1975).

15. Warner, M. & Terentjev, E. M. *Liquid crystal elastomers* (Oxford university press, 2007).

16. Muševič, I. *Liquid crystal colloids* (Springer, 2017).

17. Blinov, L. M. *Structure and properties of liquid crystals* (Springer Science & Business Media, 2010).

18. Goodby, J. W. 4'-pentyl-4-cyanobiphenyl-5CB. *Liquid Crystals* **51,** 1272–1295 (2024).

19. Brömmel, F., Kramer, D. & Finkelmann, H. Preparation of liquid crystalline elastomers. *Liquid crystal elastomers: Materials and applications,* 1–48 (2012).

20. Lagerwall, J. Liquid crystal elastomer actuators and sensors: Glimpses of the past, the present and perhaps the future. *Programmable Materials* **1,** e9 (2023).

21. Ribas-Massonis, A., Cicujano, M., Duran, J., Besalú, E. & Poater, A. Free-radical photopolymerization for curing products for refinish coatings market. *Polymers* **14,** 2856 (2022).

22. Fouassier, J.-P. & Lalevée, J. *Photoinitiators for polymer synthesis: scope, reactivity, and efficiency* (John Wiley & Sons, 2012).

23. Lang, M., Hirner, S., Wiesbrock, F. & Fuchs, P. A review on modeling cure kinetics and mechanisms of photopolymerization. *Polymers* **14,** 2074 (2022).

24. Ballard, N. & Asua, J. M. Radical polymerization of acrylic monomers: An overview. *Progress in Polymer Science* **79,** 40–60 (2018).

25. Crivello, J. V. & Reichmanis, E. Photopolymer materials and processes for advanced technologies. *Chemistry of Materials* **26,** 533–548 (2014).

26. Ravve, A. & Ravve, A. *Light-associated reactions of synthetic polymers* (Springer, 2006).

27. Bagheri, A. & Jin, J. Photopolymerization in 3D printing. *ACS Applied Polymer Materials* **1,** 593–611 (2019).

28. O'Halloran, S., Pandit, A., Heise, A. & Kellett, A. Two-photon polymerization: fundamentals, materials, and chemical modification strategies. *Advanced Science* **10,** 2204072 (2023).

29. Ligon, S. C., Liska, R., Stampfl, J., Gurr, M. & Mülhaupt, R. Polymers for 3D printing and customized additive manufacturing. *Chemical reviews* **117,** 10212–10290 (2017).

30. Herbert, K. M. *et al.* Synthesis and alignment of liquid crystalline elastomers. *Nature Reviews Materials* **7,** 23–38 (2022).

31. Xia, Y., Cedillo-Servin, G., Kamien, R. D. & Yang, S. Guided Folding of Nematic Liquid Crystal Elastomer Sheets into 3D via Patterned 1D Microchannels. *Advanced Materials (Deerfield Beach, Fla.)* **28,** 9637–9643 (2016).

32. Zeng, H. *et al.* Alignment engineering in liquid crystalline elastomers: Free-form microstructures with multiple functionalities. *Applied Physics Letters* **106** (2015).

33. Ware, T. H., Biggins, J. S., Shick, A. F., Warner, M. & White, T. J. Localized soft elasticity in liquid crystal elastomers. *Nature communications* **7,** 10781 (2016).

34. De Haan, L. T., Sánchez-Somolinos, C., Bastiaansen, C. M., Schenning, A. P. & Broer, D. J. Engineering of complex order and the macroscopic deformation of liquid crystal polymer networks. *Angewandte Chemie International Edition* **51,** 12469–12472 (2012).

35. McConney, M. E. *et al.* Topography from topology: photoinduced surface features generated in liquid crystal polymer networks. *Advanced Materials* **25,** 5880–5885 (2013).

36. De Haan, L. T. *et al.* Accordion-like actuators of multiple 3D patterned liquid crystal polymer films. *Advanced Functional Materials* **24,** 1251–1258 (2014).

37. Ceamanos, L. *et al.* Four-dimensional printed liquid crystalline elastomer actuators with fast photoinduced mechanical response toward light-driven robotic functions. *ACS applied materials & interfaces* **12,** 44195–44204 (2020).

38. Ambulo, C. P. *et al.* Four-dimensional printing of liquid crystal elastomers. *ACS applied materials & interfaces* **9,** 37332–37339 (2017).

39. López-Valdeolivas, M., Liu, D., Broer, D. J. & Sánchez-Somolinos, C. 4D printed actuators with soft-robotic functions. *Macromolecular rapid communications* **39,** 1700710 (2018).

40. Kotikian, A., Truby, R. L., Boley, J. W., White, T. J. & Lewis, J. A. 3D printing of liquid crystal elastomeric actuators with spatially programed nematic order. *Advanced materials* **30,** 1706164 (2018).

41. Tabrizi, M., Ware, T. H. & Shankar, M. R. Voxelated molecular patterning in three-dimensional freeforms. *ACS applied materials & interfaces* **11,** 28236–28245 (2019).

42. Münchinger, A., Hsu, L.-Y., Fürniß, F., Blasco, E. & Wegener, M. 3D optomechanical metamaterials. *Materials Today* **59,** 9–17 (2022).

43. Münchinger, A. *et al.* Multi-photon 4D printing of complex liquid crystalline microstructures by in situ alignment using electric fields. *Advanced Materials Technologies* **7,** 2100944 (2022).

44. Gulati, L., Sánchez-Somolinos, C., Giesselmann, F. & Fischer, P. Aligning and Observing the Liquid Crystal Director in 3D Using Small Magnetic Fields and a Wedge-Cell. *Advanced Functional Materials,* 2413513 (2024).

45. H. G. Hauck, G. H. *Flüssigkristalle. In "Lehrbuch der Experimentalphysik" (ed. Bergmann-Schaefer)* 649–710 (de Gruyter, 2008).

46. White, T. J. & Broer, D. J. Programmable and adaptive mechanics with liquid crystal polymer networks and elastomers. *Nature materials* **14,** 1087–1098 (2015).

47. Broer, D. J. & Mol, G. N. Anisotropic thermal expansion of densely cross-linked oriented polymer networks. *Polymer Engineering & Science* **31,** 625–631 (1991).

48. Kularatne, R. S., Kim, H., Boothby, J. M. & Ware, T. H. Liquid crystal elastomer actuators: Synthesis, alignment, and applications. *Journal of Polymer Science Part B: Polymer Physics* **55,** 395–411 (2017).

49. Kotikian, A. *et al.* Untethered soft robotic matter with passive control of shape morphing and propulsion. *Science robotics* **4,** eaax7044 (2019).

50. Palagi, S. *et al.* Structured light enables biomimetic swimming and versatile locomotion of photoresponsive soft microrobots. *Nature materials* **15,** 647–653 (2016).

51. Espíndola-Pérez, E. R., Campo, J. & Sánchez-Somolinos, C. Multimodal and Multistimuli 4D-Printed Magnetic Composite Liquid Crystal Elastomer Actuators. *ACS Applied Materials & Interfaces* **16,** 2704–2715 (2023).

52. Sartori, P., Yadav, R. S., Del Barrio, J., DeSimone, A. & Sánchez-Somolinos, C. Photochemically Induced Propulsion of a 4D Printed Liquid Crystal Elastomer Biomimetic Swimmer. *Advanced Science,* 2308561 (2024).

53. McDougall, L. *et al.* Free-form liquid crystal elastomers via embedded 4D printing. *ACS Applied Materials & Interfaces* **15,** 58897–58904 (2023).

54. Li, S. *et al.* Digital light processing of liquid crystal elastomers for self-sensing artificial muscles. *Science Advances* **7,** eabg3677 (2021).

55. Mainik, P. *et al.* DLP 4D printing of multi-responsive bilayered structures. *Advanced Materials Technologies* **8,** 2300727 (2023).

56. Concellón, A., Mainik, P., Vazquez-Martel, C., Álvarez-Solana, C. & Blasco, E. 4D Printing of Liquid Crystal Emulsions for Smart Structures with Multiple Functionalities. *Angewandte Chemie,* e202421162 (2024).

57. Herman, J. A. *et al.* Digital Light Process 3D Printing of Magnetically Aligned Liquid Crystalline Elastomer Free–forms. *Advanced Materials,* 2414209 (2024).

58. Wang, Y. *et al.* Printing Mosaics of Magnetically Programmed Liquid Crystal Directors for Reversibly Morphing Soft Matter. *arXiv preprint arXiv:2401.06590* (2024).

59. Hsu, L.-Y. *et al.* Alignment and actuation of liquid crystals via 3D confinement and two-photon laser printing. *Science Advances* **10,** eadq2597 (2024).

60. Hsu, L.-Y. *et al.* A Facile Approach for 4D Microprinting of Multi-Photoresponsive Actuators. *Advanced Materials Technologies* **8,** 2200801 (2023).

61. Zeng, H. *et al.* Light-fueled microscopic walkers. *Advanced Materials (Deerfield Beach, Fla.)* **27,** 3883 (2015).

62. Martella, D., Nocentini, S., Nuzhdin, D., Parmeggiani, C. & Wiersma, D. S. Photonic microhand with autonomous action. *Advanced Materials* **29,** 1704047 (2017).

63. Flatae, A. M. *et al.* Optically controlled elastic microcavities. *Light: Science & Applications* **4,** e282–e282 (2015).

64. Sungur, E. *et al.* Temperature tunable optical gratings in nematic elastomer. *Applied Physics A* **98,** 119–122 (2010).

65. Nocentini, S., Martella, D., Parmeggiani, C., Zanotto, S. & Wiersma, D. S. Structured optical materials controlled by light. *Advanced Optical Materials* **6,** 1800167 (2018).

66. Zanotto, S. *et al.* Multichannel remote polarization control enabled by nanostructured liquid crystalline networks. *Applied Physics Letters* **114** (2019).

67. Loterie, D., Delrot, P. & Moser, C. High-resolution tomographic volumetric additive manufacturing. *Nature communications* **11,** 852 (2020).

68. Kelly, B. E. *et al.* Volumetric additive manufacturing via tomographic reconstruction. *Science* **363,** 1075–1079 (2019).

69. Riffe, M. B. *et al.* Multi-Material Volumetric Additive Manufacturing of Hydrogels using Gelatin as a Sacrificial Network and 3D Suspension Bath. *Advanced Materials,* 2309026 (2024).

70. Sahin, M. A., Werner, H., Udani, S., Di Carlo, D. & Destgeer, G. Flow lithography for structured microparticles: fundamentals, methods and applications. *Lab on a Chip* **22,** 4007–4042 (2022).

71. Shaw, L. A. *et al.* Scanning two-photon continuous flow lithography for synthesis of high-resolution 3D microparticles. *Optics express* **26,** 13543–13548 (2018).

72. Chizari, S. *et al.* Scanning two-photon continuous flow lithography for the fabrication of multi-functional microparticles. *Optics Express* **28,** 40088–40098 (2020).

73. Kiefer, P. *et al.* A multi-photon (7× 7)-focus 3D laser printer based on a 3D-printed diffractive optical element and a 3D-printed multi-lens array. *Light: Advanced Manufacturing* **4,** 28–41 (2024).

74. Shusteff, M. *et al.* One-step volumetric additive manufacturing of complex polymer structures. *Science advances* **3,** eaao5496 (2017).

75. Ouyang, W. *et al.* Ultrafast 3D nanofabrication via digital holography. *Nature Communications* **14,** 1716 (2023).

76. Somers, P. *et al.* The physics of 3D printing with light. *Nature Reviews Physics* **6,** 99–113 (2024).

77. Somers, P., Koch, S., Kiefer, P., Meretska, M. L. & Wegener, M. Holographic multi-photon 3D laser nanoprinting–at the speed of light: opinion. *Optical Materials Express* **14,** 2370–2376 (2024).

78. Rogalski, M. S. & Palmer, S. B. *Advanced university physics* (CRC Press, 2018).

79. Hecht, E. *Optics* (Pearson Education India, 2012).

80. Ghatak, A. *et al. Optics/Ajoy Ghatak.* 2010.

81. Pavlin, J., Vaupotič, N. & Čepič, M. Direction dependence of the extraordinary refraction index in uniaxial nematic liquid crystals. *European journal of physics* **34,** 331 (2013).

82. Liang, Q.-T. Simple ray tracing formulas for uniaxial optical crystals. *Applied optics* **29,** 1008–1010 (1990).

83. Li, S. *et al.* Controlling liquid crystal orientations for programmable anisotropic transformations in cellular microstructures. *Advanced Materials* **33,** 2105024 (2021).

84. Frisken, B., Carolan, J., Palffy-Muhoray, P., Perenboom, J. & Bates, G. SQUID susceptibility measurements on 5CB. *Molecular Crystals and Liquid Crystals Letters* **3,** 57–62 (1986).

85. Diogo, A. & Martins, A. Order parameter and temperature dependence of the hydrodynamic viscosities of nematic liquid crystals. *Journal de Physique* **43,** 779–786 (1982).

86. Kosa, T. & Palffy-Muhoray, P. Magnetic field induced deformations in nematic liquid crystals. *Liquid Crystals Today* **6,** 7–8 (1996).

87. Yao, Y. *et al.* Multiresponsive polymeric microstructures with encoded predetermined and self-regulated deformability. *Proceedings of the National Academy of Sciences* **115,** 12950–12955 (2018).

88. Shin, J. *et al.* Thermally functional liquid crystal networks by magnetic field driven molecular orientation. *ACS Macro Letters* **5,** 955–960 (2016).

89. Buka, A. & De Jeu, W. Diamagnetism and orientational order of nematic liquid crystals. *Journal de Physique* **43,** 361–367 (1982).

90. Shahsavan, H. *et al.* Bioinspired underwater locomotion of light-driven liquid crystal gels. *Proceedings of the National Academy of Sciences* **117,** 5125–5133 (2020).

91. Li, S., Aizenberg, M., Lerch, M. M. & Aizenberg, J. Programming deformations of 3D microstructures: opportunities enabled by magnetic alignment of liquid crystalline elastomers. *Accounts of Materials Research* **4,** 1008–1019 (2023).

92. Ania, F., Flores, A., Kricheldorf, H. & Baltá-Calleja, F. J. Real-time WAXS study of induced orientation in a liquid crystalline polyester under the influence of a magnetic field. *Polymer* **44,** 5909–5913 (2003).

93. Ni, B. *et al.* Customizable sophisticated three-dimensional shape changes of large-size liquid crystal elastomer actuators. *ACS Applied Materials & Interfaces* **13,** 54439–54446 (2021).

94. Oldenbourg, R. A new view on polarization microscopy. *Nature* **381,** 811–812 (1996).

95. Wu, J.-F. & Zhang, Y.-T. The relation between the propagation of extraordinary ray and the optical axis in the uniaxial crystal. *Optik-International Journal for Light and Electron Optics* **124,** 2667–2669 (2013).

96. Avedaño-Alejo, M. Analysis of the refraction of the extraordinary ray in a plane-parallel uniaxial plate with an arbitrary orientation of the optic axis. *Opt. Express* **13,** 2549 (2005).

97. Kędzierski, J. *et al.* Determination of ordinary and extraordinary refractive indices of nematic liquid crystals by using wedge cells. *Opto-Electronics Review* **18,** 214–218 (2010).

98. Kowiorski, K. *et al.* Application of modified interference wedge method in measurements of indices of refraction and birefringence of nematic liquid crystals. *Acta Physica Polonica A* **124,** 946–948 (2013).

99. Pfeifer, M. & Fischer, P. Weak value amplified optical activity measurements. *Optics express* **19,** 16508–16517 (2011).

100. Ghosh, A., Hill, W. & Fischer, P. Observation of the Faraday effect via beam deflection in a longitudinal magnetic field. *Physical Review A—Atomic, Molecular, and Optical Physics* **76,** 055402 (2007).

101. Kawata, S., Sun, H.-B., Tanaka, T. & Takada, K. Finer features for functional microdevices. *Nature* **412,** 697–698 (2001).

102. Zhang, J., Pégard, N., Zhong, J., Adesnik, H. & Waller, L. 3D computer-generated holography by non-convex optimization. *Optica* **4,** 1306–1313 (2017).

103. Maruo, S. & Ikuta, K. Three-dimensional microfabrication by use of single-photon-absorbed polymerization. *Applied Physics Letters* **76,** 2656–2658 (2000).